Probing Cosmology with Strong Lensing: from image processing to cosmological constraints

Tese apresentada
ao
Centro Brasileiro de Pesquisas Físicas
como requisito para
A obtenção do título
de
Doutor em Fisica

Clécio Roque De Bom

Orientador: Prof. Dr. Martín Makler

Rio de Janeiro, Março de 2017

"(...) omnipotens, audacibus adnue cœptis."
"(...) [Deus] onipotente, abençoe nossos audaciosos objetivos."
— Adaptado de Vírgilio em Eneida, livro IX

Dedicado as mulheres da minha vida, Denise Roque De Bom
e Patrícia Apicelo Souza De Bom.

Agradecimentos

"Se tudo aquilo que queres fazer começardes a te perguntar 'Será que quero mesmo faze-lo um número infinito de vezes?' Isso será para ti o centro de gravidade mais sólido. Minha doutrina ensina ' Vive de tal maneira que devas desejar reviver, é o dever (...) mais que saiba bem, aonde vai a sua preferência e que não recue perante nenhum meio' ..."

— Friedrich Nietzsche

Faço neste espaço um agradecimento sincero às inúmeras pessoas que participaram da minha vida e mesmo sem querer contribuiram para este momento. Eu agradeço ao *logos* universal, o sentido último, por vezes misterioso, que convencionamos chamar de Deus. Agradeço ao estímulo dado pelos meus pais, ao pai mais orgulhoso que eu já vi, Clésio De Bom que acompanha este momento. Também agradeço a minha mãe Denise De Bom que esteve sempre ao meu lado neste caminho. Agradeço a minha esposa e companheira de vida Dra. Patrícia Apicelo Souza De Bom sem a qual a vida perderia grande parte do seu brilho. Agradeço ao meu orientador Dr. Martín Makler sem a sua expertise, amizade e compreensão este trabalho jamais se concretizaria.

Agradeço aos meus familiares e companheiros de jornada da vida. Que me deram grande suporte emocional ao longo do tempo. Em especial aos amigos Dr. Marcelo Portes de Albuquerque e Dr. Márcio Portes de Albuquerque, aos amigos de Colégio Pedro II: Bruno, Leonardo, Cardoso, Dr. Rodrigo Couto, Gabriel, Dr. Ricardo Pedroza, Renata, Thiago, Macedo e aos da física Cinthya, Thiago Carneiro, Maíra. Também ao apoio dos meus familiares, meu irmão Leandro, Marcela, Valéria, Rose, minha sogra Eliane, meu orgulhoso sogro Paulo e a memória do meu tio Dr. Odir Clécio Roque.

Agradeço especialmente aos amigos que participaram no desenvolvimento de parte do trabalho acadêmico Dr. Gabriel Caminha e Manuel Valentín. Aos colegas e amigos de departamento Maria Elidaiana, Jaime, Vanessa e Arthur.

Dedico com carinho aos pequenos, que lhes sirva de inspiração ao estudo continuo: Júlia De Bom, minha sobrinha, Leonardo Linhares, meu querido afilhado, Cauã Leonardo De Bom, Yasmin Apicelo, Guilherme Linhares e ao Bento Maia. Que o conhecimento, em todas as suas diversas formas, mas particularmente o científico, possa ser um valor imanente do ser e não apenas uma ferramenta circunscrita ao nosso tempo.

Por fim, agradeço ao CBPF, CEFET-RJ e ao CNPQ que criaram as oportunidades para que eu concluísse esta etapa.

Resumo

Bom, C. R. **Cosmologia com efeito forte de Lentes Gravitacionais: do processamento de imagens aos vínculos cosmológicos**. 2017. Tese (Doutorado), Centro Brasileiro de Pesquisas Físicas, Rio de Janeiro, 2017.

O efeito forte de Lentes Gravitacionais é uma ferramenta de interesse para explorar a distribuição de matéria em galáxias e aglomerados de galáxias, podendo também fornecer informação sobre a geometria do Universo entre outras aplicações. Em particular sistemas de múltiplas fontes em diferentes desvios para o vermelho vem sendo utilizados para determinar razões de distância diâmetro angular e, a partir delas, extrair vínculos cosmológicos.

Nesta tese nós dicutimos diversos aspectos da área de efeito forte de Lentes Gravitationais. Primeiramente nós introduzimos uma nova técnica para extrair atributos de imagens de arcos gravitacionais a qual denominamos: método de filamentação *Mediatrix*. Esta técnica foi construída para analisar formas curvas e alongadas. Analisamos a qualidade de algumas quantidades morfológicas obtidas por essa técnica em arcos tais como raio de curvatura, comprimento e largura.

Na segunda parte da tese, discutimos como encontrar sistemas de lentes gravitacionais. Iniciamos a discussão descrevendo a busca visual em uma levantamento de grande área, o *Dark Energy Survey (DES)*. A seguir, discutimos a construção de métodos automatizados para encontrar arcos. O primeiro deles baseados nos atributos morfológicos obtidos pelo método *Mediatrix* e o uso de uma rede neural de retropropagação (*backpropagation*). Estudamos esse método otimizando seus parâmetros de entrada para obter uma maior completeza e uma menor quantidade de falsos positivos. Construímos, também, um outro método para buscar lentes gravitationais voltado para o regime de lentes na escala de galáxias. Este método foi baseado em um algoritmo de aprendizagem profunda (*deep learning*) denominado rede neural convolucional (*Convolutional Neural Network*; CNN). Nós treinamos e validamos este método em um conjunto de imagens simuladas.

Na última parte desta tese, nós discutimos como a determinação de parâmetros cosmológicos obtidos pela modelagem de lentes gravitacionais se comportam em diferentes condições observacionais, isto é, imagens de menor qualidade tais como levantamentos de grande área. Analisamos imagens com menor profundidade e com maior função de espalhamento de ponto (*Point Spread Function*; PSF). O foco desta análise foi no aglomerado RXC J2248.7−4431, que contêm múltiplas fontes e tem sido analisado utilizando imagens profundas do telescópio

Hubble além de dados de espectroscopia disponíveis.
Palavras-chave: Lentes Gravitacionais, Cosmologia, Processamento de Imagens

Abstract

Bom, C. R. **Probing Cosmology with Strong Lensing: from image processing to cosmological constrains**. 2017. Tese (Doutorado), Centro Brasileiro de Pesquisas Físicas, Rio de Janeiro, 2017.

Strong Lensing is a powerful probe of the matter distribution in galaxies and galaxy clusters and the large-scale geometry of the Universe, among other applications. In particular, systems with sets of multiple images originating from sources at different redshifts have been used to determine cosmological distance ratios, and therefore to constrain cosmological parameters. In this thesis, we address several aspects of the Strong Lensing program. We start by proposing a novel image processing technique to extract features from arc images named Mediatrix Filamentation Method, which is particularly suited to curved and elongated shapes. We study how some morphological parameters of the arcs such as curvature radius, length and width can be recovered. In the second part of this work, we discuss how to find Strong Lensing systems. We start by describing a visual search in the Science Verification area of the Dark Energy Survey. Thereafter, we discuss an automated method to find Gravitational Arcs based on the features derived from the Mediatrix Method and on an Artificial Neural Network (ANN). We study this approach, named ANN Mediatrix Arcfinder (AMA for short), in order to tune its parameters to reach a reliable detection fraction with a low fake positive rate. Then we discuss a second method most suitable to galaxy scale lensing based on Convolutional Neural Networks (CNN). We trained and validated the method on a sample of galaxy-scale lensing simulations. In the last part address the determination of cosmological parameters from Strong Lensing systems and, in particular, on systematic errors arising from the observational conditions, such as the depth and seeing of the images. We focus on Strong Lensing systems with a large number of families of multiple images that have been exhaustively analyzed using deep space-based images (from HST) and massive spectroscopic follow-up.

Keywords: Lensing: Strong, Cosmology, Image Processing

Contents

List of Figures

Chapter 1

Introduction

The Gravitational Lensing effect (e.g., Mollerach & Roulet, 2002; Petters et al, 2012; Schneider et al, 2013) is produced by the deflection of light caused by the matter distribution on its way from the source to the observer. This matter distribution distorts space-time, acting as a lens. The image of distant astronomical objects may be strongly distorted and magnified in the so-called Strong Lensing regime, forming multiple images and gravitational arcs. The first detection of gravitational arcs produced by the lensing of galaxies by galaxy clusters was performed by Lynds & Petrosian (1986) and Soucail et al. (1987). The lensing phenomenon conserves the surface brightness, such that magnified images, i.e., with a larger angular size due to lensing, are also brighter. Therefore, Strong Lensing acts as a *gravitational telescope*, enabling the study of distant galaxies that would not be detected under the same observational conditions (see, for example, Jones et al, 2010; Richard et al, 2011).

Since Strong Lensing is produced by massive matter haloes along the line of sight, it provides useful tools to uncover the mass distribution in galaxies (e.g. Koopmans et al, 2006; Treu & Koopmans, 2002; Treu & Koopmans, 2002) and galaxy clusters (e.g., Abdelsalam et al. , 1998; Carrasco et al, 2010; Coe et al, 2010; Kovner, 1989; Natarajan et al, 2007; Zackrisson & Riehm , 2010), independently of the dynamical state of the systems or the nature of their constituents, presenting a window to study dark matter (see, e.g., Meneghetti et al, 2004).

Besides the mass distribution in the deflector, the Lensing effect also depends on the angular diameter distances between observer, lens and sources. These distances are cosmology dependent. One may use the Strong Lensing effect to constrain those distances and

therefore infer the cosmological parameters. This approach is being used as a complementary cosmological probe (see, e.g., Caminha et al, 2016b; Jullo et al, 2010). In chapter 2 we briefly review some of the key aspects in the Strong Lensing field and discuss how it can be used as a tool for Cosmology.

The many applications of gravitational arcs in astrophysics and cosmology have spurred the search for these objects in both space-based and ground based observations. This includes searches in Hubble Space Telescope (HST) mosaics, such as in the *Hubble Deep Field* (HDF; Hogg et al, 1996), the *HST Medium Deep Survey* (Ratnatunga et al, 1999), the *Great Observatories Origins Deep Survey* (GOODS; Fassnacht et al, 2004), the *Extended Groth Strip* (EGS; Marshall et al, 2009), and the *HST Cosmic Evolution survey* (COSMOS; Faure et al, 2008; Jackson, 2008), as well as in targeted observations of galaxies (Bolton et al, 2006; Brownstein et al, 2012) and clusters (Horesh et al, 2010; Sand et al., 2005; Smith et al, 2005; Xu et al, 2016). Investigations from the ground include follow-ups of clusters (Furlanetto et al, 2013a; Hennawi et al, 2008; Kausch et al, 2010; Luppino et al., 1999; Zaritsky & Gonzalez, 2003) and galaxies (Willis et al, 2006), and searches in wide-field surveys, such as in the *Red-Sequence Cluster Survey* (RCS; Bayliss, 2012; Gladders et al, 2003), the *Sloan Digital Sky Survey* (SDSS; Bayliss, 2012; Belokurov et al, 2009; Estrada et al, 2007; Kubo et al, 2010; Wen et al, 2011), the *Deep Lens Survey* (DLS; Kubo & Dell'Antonio, 2008), *The Canada-France-Hawaii Telescope (CFHT) Legacy Survey* (CFHTLS; Cabanac et al., 2007; Gavazzi et al, 2014; Maturi et al, 2014; More et al, 2012, 2016; Paraficz et al, 2016), the Dark Energy Survey (DES; Nord et al, 2015), the Kilo Degree Survey (KIDS; Petrillo et al., 2017) and the *CFHT Stripe 82 Survey* (CS82; Caminha, More et al., in prep.).

As of now, the largest homogeneous samples of gravitational arcs have on the order of a hundred systems. However, due to the small size the samples of lens systems, several studies are hindered, in particular, those using arc statistics (e.g. Bartelmann et al., 1998; Golse et al, 2002; Meneghetti et al, 2004). These numbers will increase by one order of magnitude with the close completion of the KIDS[1] (KiDS; de Jong et al, 2015) and DES[2] (DES; Dark Energy Survey Collaboration et al, 2016), which will cover, respectively,

[1] http://kids.strw.leidenuniv.nl/
[2] http://www.darkenergysurvey.org

1000 and 5000 square degrees with sub-arcsecond seeing. Comparable numbers are expected from the ongoing Hyper Suprime-Cam[3] (HSC) and the forthcoming Javalambre Physics of the Accelerating Universe Astrophysical Survey (J-PAS; Benitez et al, 2014) projects. These numbers are expected to increase even further in the near future, with the operation of the Large Synoptic Survey Telescope (LSST; LSST Sci. Collaboration et al, 2009) and Euclid[4] (Refregier et al, 2010), which are both expected to detect $\mathcal{O}(10^5)$ systems with arcs (Collett, 2015).

The vast majority of the current samples of arc systems involve a visual search and classification. This is true for the targeted surveys and also for the wide-field imaging surveys, where either the full footprint or cutouts around potential lenses (e.g., luminous red-galaxies, galaxy clusters) are visually inspected. In section 4.1 we discuss the visual inspection approach in which we participated using Dark Energy Survey Science Verification data (Nord et al, 2015), which covered an area of 250-sq-deg.

However, this manual procedure will become prohibitive for the complete DES and KiDS footprints, not to say for LSST and Euclid. Therefore, the development of automated arc finding methods is absolutely needed for the scrutiny of these surveys in the quest for gravitational arcs. In section 4.2 propose a novel arcfinder algorithm based on pattern recognition suitable for cluster scale lensing, while in section 4.5.2 we propose an algorithm based on deep learning methods for galaxy scale lensing.

Regardless of the size of the survey, automated arc detection is essential for an objective and reproducible definition of arc samples, which often includes the determination of arc properties. In chapter 3 we discuss how to obtain arc morphological features with a novel approach to measure curvature (Bom et al., A&A submitted). This is, of course, critical for arc statistics (see, e.g., Meneghetti et al, 2013; Xu et al, 2016) and for any comparison of real and simulated data (e.g., Horesh et al, 2011, 2005) and among different data sets (e.g., Horesh et al, 2010).

During the past decade, the Strong Lensing program has been emerging as a relevant probe to constrain cosmological models, using Strong Lensing data alone or in combina-

[3] http://www.naoj.org/Projects/HSC/surveyplan.html
[4] http://www.euclid-ec.org/

tion with other probes (e.g. Bartelmann et al, 1998; Caminha et al, 2016b; Cao et al, 2015; Cooray, 1999; Golse et al, 2002; Jullo et al, 2010; Magaña et al, 2015; Meneghetti et al, 2004, 2005; Treu & Koopmans, 2002; Yamamoto et al, 2001). High accuracy time-delay distance measurements in multiple image systems are used to measure the expansion rate of the universe using QSOs (Oguri, 2007; Suyu et al, 2010). More recently, using multiple images of a Supernova (Goobar et al, 2016; Kelly et al, 2015). The time time-delays were also exploited in the determination of the dark energy equation of state (Suyu et al, 2013). In the recent years, arcs and Einstein rings, in combination with kinematic information for the lenses, have also been employed for testing modified gravity (e.g. Enander & Mörtsell, 2013; Pizzuti et al, 2016; Schwab et al, 2010).

Among the many Strong Lensing observables being used to constrain Cosmology we focus our attention on Strong Lensing constraints arising from multiple families of multiple images. This involves a detailed modeling of the galaxy cluster mass distribution, whose free parameters are fitted together with the cosmological parameters. This approach has also been explored as a powerful probe of the mass distribution in the inner cluster regions (e.g., Grillo et al, 2015; Halkola et al, 2008). The many applications of inverse modelling have motivated the developments of several algorithms to derive the lens mass distribution either in a parametric way or in *free-form* (e.g., Bradač et al, 2009; Coe et al, 2008; Diego et al., 2005; Jullo et al, 2007; Oguri, 2010). The great number of free parameters and diverse response due different techniques, models or observational conditions led to a concern in the robustness of this type of analysis. Some authors have investigated the systematic errors arising from the models and make comparisons between the lens inversion techniques (e.g. Meneghetti et al, 2016; Priewe et al, 2016). In chapter 5 we address the issue of systematics in the multiple image Strong Lensing constraints, due to observational effects. Our goal is to analyze the response of cosmography to observational conditions, in particular in the conditions of wide-field surveys, where we are more likely to find a large number of systems with several arcs for which deep data from space may not be obtained. In chapter 6 we wrap up our results and mention current and upcoming publications based on them.

Chapter 2

Introduction to Gravitational Lensing

2.1 The deflection of light

The history of the light deflection by massive bodies can by traced back to Newton's book *Optics* in which he speculates that light particles should be affected by gravitational potentials. Although only in the late 17th century *Henry Cavendish* and *John Mitchell* derived the first attempt to calculate the deflection angle based on Newton's Gravity. For a point mass deflector with mass M, this angle $\hat{\alpha}$ is given by:

$$\hat{\alpha} = \frac{2\,G\,M}{c^2\,\xi_0}, \tag{2.1}$$

where G is the gravitational constant, c is the light speed and ξ_0 the impact factor. Since in Newton's Gravity only mass can feel the gravitational pull, Eq. (2.1) relies on the corpuscular theory of light. In 1801 *Von Soldner* obtained $\hat{\alpha} = 0.83''$ for a light particle near the solar disk (Jakı 1978).

In 1915, considering the General Theory of Relativity (hereafter GR), Einstein obtained a corrected deflection angle:

$$\hat{\alpha} = \frac{4\,G\,M}{c^2\,\xi_0}, \tag{2.2}$$

which differs from (2.1) by a factor of two. The light deflection by stars near the Sun was first observed during an eclipse in 1919 by two teams, one at Príncipe island led by Sir Arthur Stanley Eddington and the other at Sobral, Brazil, led by Andrew Claude de la Cherois

Crommelin. The teams obtained 1.61 ± 0.30 (Dyson et al, 1920) in agreement with the GR.

From the confirmation of the light deflection to the current time, the Gravitational Lensing studies and developments gave rise to a wealth of applications in astrophysics and Cosmology as discussed in the previous chapter. In this thesis, we focus in the Strong Lensing of background galaxy by a foreground galaxy or galaxy cluster. In this case, the background source may be multiply imaged, magnified and/or strongly distorted, forming the Gravitational Arcs or Einstein Rings. In the next sections, we discuss some key aspects of Cosmology and in XX we discuss the basic ideas in the Strong Lensing field.

2.2 Homogeneous and isotropic Cosmology

Strong Lensing phenomena involve cosmological distances, which can be used as a probe of Cosmology. In particular, in this work we focus on the angular diameter distances. For an object with size x and angular size $\delta\theta$ the angular diameter distance is given by:

$$D_A = \frac{x}{\delta\theta}. \tag{2.3}$$

The key to assess Cosmology in this context is the connection between distances and cosmological parameters which we discuss in this section.

In GR, the presence of energy distorts the space-time according to the Einstein's Field Equations (hereafter EFE, see, e.g., Schutz, 2009; Weinberg, 1972):

$$G_{\mu\nu} = \frac{8\pi G}{c^4} T_{\mu\nu}, \tag{2.4}$$

where $G_{\mu\nu}$ is the Einstein tensor, related to the geometry of space time, $T_{\mu\nu}$ is the stress-energy tensor, which defines the mass-energy content of space-time. The EFE solutions are metric tensors $g_{\mu\nu}$ which describe the geometry of space-time.

On large scales the Universe is approximately homogeneous and isotropic. This statement is supported by the distribution of galaxies in large scales and the Cosmic Microwave Background (CMB) which is nearly isotropic (see, for instance, Peebles, 1993; Ryden, 2016). In this context, the metric which satisfies these conditions is the so-called Friedmann-Lemâitre-

Robertson-Walker (FLRW):

$$ds^2 = c^2dt^2 - a^2(t)d^2\sigma,, \tag{2.5}$$

where $a(t)$ is the scale factor representing the universe expansion with $a(t_0)$ denoting the scale factor in present time and $d^2\sigma$ is the line element of space with constant curvature,

$$d^2\sigma = \frac{d|\vec{x}|^2}{1-k|\vec{x}|^2} + |\vec{x}|^2(d\theta^2 + \sin^2\theta d\phi^2), \tag{2.6}$$

where $\vec{x}$ are the so-called comoving coordinates and k is the curvature. From the EFE one can derive the Friedmann equations, the first from the 00 component of 2.4:

$$H = \frac{\dot{a}^2}{a^2} = \frac{8\pi G\rho}{3c^2} - \frac{kc^2}{a^2}, \tag{2.7}$$

where H is the expansion rate of the Universe, ρ is the energy density, k is a constant which depends on the curvature. Since the CMB also gives a strong evidence that the Universe is approximately flat, from now on we take $k = 0$ (e.g., Komatsu et al, 2009, 2011; Planck Collaboration et al, 2016). The second Friedmann equation rises from the trace of EFE.

$$\frac{\ddot{a}}{a} = -\frac{4\pi G}{3}\left(\rho + \frac{3p}{c^2}\right). \tag{2.8}$$

The energy density can be written as a sum of several components

$$\rho = \rho_m + \rho_r + \rho_{DE}, \tag{2.9}$$

where ρ_m stands for the energy density of matter, ρ_r is the energy density of radiation and ρ_{DE} is the density of the so-called dark energy, a component which accelerates the Universe expansion rate (Riess et al, 1998). It is worth noticing that, at present, ρ_r is very small and the energy density is essentially dominated by ρ_m and ρ_{DE}. From 2.7 and 2.8 we may derive the energy-momentum conservation:

$$\dot{\rho} = -3\frac{\dot{a}}{a}\left(\rho + \frac{p}{c^2}\right). \tag{2.10}$$

The last equation can be easily solved if one considers that each component conserves the energy independently and if we take the equation of state of the fluid to be $p = w\rho$ with w constant. This leads to

$$\rho \propto a^{-3(1+w)}, \tag{2.11}$$

where $w_m = 0$ for non-relativistic matter, $w_r = 1/3$ for radiation and $w_X = -1$ for dark energy. It is convenient to introduce the critical density, i.e., the energy density in which the Universe is flat:

$$\rho_{crit} = \frac{3H^2}{8\pi G}, \tag{2.12}$$

which can be used to define the density parameters

$$\Omega_i = \frac{\rho_i^0}{\rho_{crit}^0}, \tag{2.13}$$

where i is the energy density component and the upper index 0 denotes the present value. Equation 2.13 can be combined with the first Friedmann equation 2.7:

$$\frac{H^2}{H_0^2} = \Omega_r \left(\frac{a(t_0)}{a}\right)^4 + \Omega_m \left(\frac{a(t_0)}{a}\right)^3 + (1 - \Omega_{tot}), \tag{2.14}$$

where $\Omega_{tot} = \Omega_r + \Omega_m$. In a Universe in expansion is also interesting to consider the relation between scale factor $a(t_e)$ from a time t_e, where a photon was emitted to the scale factor at the present time t_0, $a(t_0)$, which is related to the redshift z due to Universe expansion:

$$\frac{a(t_0)}{a(t_e)} = 1 + z. \tag{2.15}$$

It is convenient choice to take $a(t_0) = 1$ which simplifies 2.15 and 2.14. It is worth noticing that the z is an observable. In the FLRW cosmologies, the distances scales with $1/H_0$ and, as the Friedmann equation describes the Universe expansion it is possible to write the angular diameter distances, defined in 2.3, as a function of the redshifts z_1 and z_2 with $z_2 > z_1$, and in terms of Cosmological parameters:

$$D_a(z_1, z_2) = \frac{c}{H_0(1 + z_2)} \int_{z_1}^{z_2} \frac{1}{\sqrt{\Omega_r(1+z)^4 + \Omega_m(1+z)^3 + \Omega_\Lambda}} dz. \tag{2.16}$$

In the Strong Lensing case, one may assess only the ratio between Cosmological Distances. Since this observable is degenerated to the Lensing mass, we may need other constraints to probe Cosmology with Strong Lensing. In cluster scales, this can be resolved using multiple images from several sources. This approach is discussed in chapter 5.

2.3 Gravitational Lensing and General Relativity

For light traveling though cosmological distances in a Universe that is homogeneous and isotropic on large scales, passing near some potential Φ (generated by a galaxy or cluster acting as a lens), one may obtain the solution of light propagation from the geodesics of the perturbed Friedmann-Lemâitre-Robertson-Walker (FLRW) metric:

$$ds^2 = \left(1 + \frac{2\Phi}{c^2}\right) c^2 dt^2 - a^2(t) \left(1 - \frac{2\Phi}{c^2}\right) d^2\sigma, \tag{2.17}$$

where $a(t)$ is the scale factor that describes the universe expansion and $d^2\sigma$ is given by (2.6). The potential is assumed to be weak in the sense that $\Phi \ll c^2$, which is an excellent approximation for galaxy and cluster scales. In this case, Φ obeys a Poisson equation:

$$\nabla_x^2 \Phi = 4\pi G a^2 (\rho - \bar{\rho}),$$

where $\bar{\rho}$ is the mean density of mass-energy in the Universe and ρ is the density at a position $\vec{x}$ and time t. Since the $\rho \gg \bar{\rho}$ for galaxies and clusters, the $\bar{\rho}$ is usually ignored. Considering this approximation, in proper coordinates $d\vec{r} = a d\vec{x}$ the Poisson equation can be written as:

$$\nabla_r^2 \Phi = 4\pi G \rho, \tag{2.18}$$

i.e., the Newtonian result.

2.4 The Lens Equation

To derive the Lens equation we consider a scheme presented in Fig. 2.1 in which a mass distribution M, which acts as a lens, is located between the observer and a source

of light. The lens is close to the line of sight between observer and source. The angle $\vec{\theta}$ is the observed position, $\vec{\beta}$ is the "real" source position, i.e., what one would observe without the light deflection and $\vec{\hat{\alpha}}$ is the deflection angle. These quantities are related by the Lens equation

$$\vec{\theta} D_{OS} = \vec{\beta} D_{OS} + \vec{\hat{\alpha}} D_{LS}, \tag{2.19}$$

where $\vec{\xi_0}$ is the impact parameter, D_{OL}, D_{LS} e D_{OS} are angular diameter distances between observer and lens, lens and source, and observer and source, respectively. As the distances are cosmological it is worth recalling that $D_{LS} \neq D_{OS} - D_{OL}$.

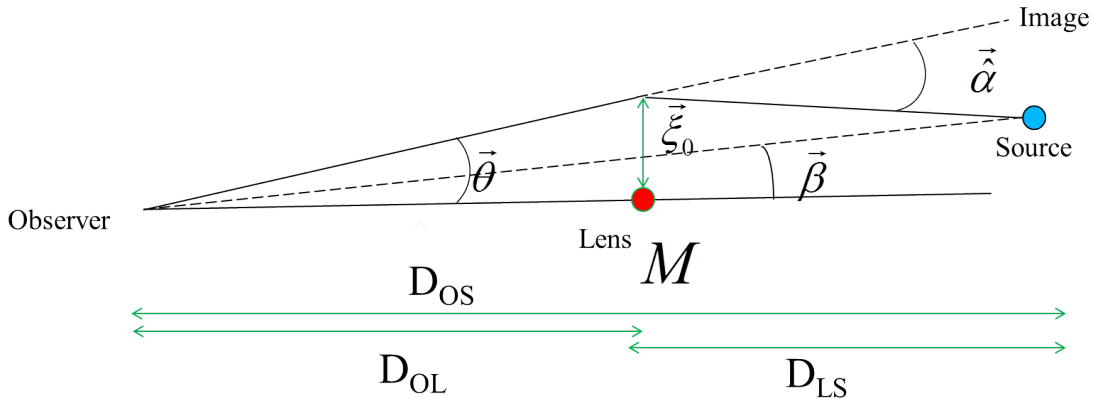

Figure 2.1: *Schematic figure of the lens equation.*

We may define the reduced deflection angle

$$\vec{\alpha} = \left(\frac{D_{LS}}{D_{OS}}\right) \vec{\hat{\alpha}}(\vec{\xi_0}), \tag{2.20}$$

such that the lens equation can be written as

$$\vec{\beta} = \vec{\theta} - \vec{\alpha}. \tag{2.21}$$

For the case of point mass lens, the deflection angle $\vec{\hat{\alpha}}$ is given by (2.2). For a perfect alignment between the lens, source and observer, in which $\vec{\beta} = 0$, due to the symmetry of the problem the image is a ring known as Einstein Ring. The position θ_E, the Einstein Radius, is given by:

$$\theta_E = \sqrt{\frac{4\,G\,M D_{LS}}{c^2 D_{OS} D_{OL}}}. \tag{2.22}$$

This quantity also defines a typical scale for the Strong Lensing regime, as the typical angular separation of the images is $\sim 2\theta_E$.

2.5 Extended Lenses

As the distances between the source, the lens, and the observer are much larger than the size of the lens one may consider only the limit of a "thin lens", we may consider that the deflection occurs in a single plane. In this approximation, we define the projected mass density

$$\Sigma(\vec{\xi}) = \int_{-\infty}^{\infty} \rho(\vec{\xi}, z) dz, \tag{2.23}$$

where we decompose $\vec{r} = \vec{\xi} + z\hat{z}$, with z is the axis defined by the observer and the lens. In the weak field regime (linear gravity) the deflection is linearly dependent with the mass. Thus we may construct a general solution for $\vec{\hat{\alpha}}$ as a sum of infinitesimal point mass lenses where each mass element contributes with a deflection angle given by 2.2:

$$\vec{\hat{\alpha}}(\vec{\xi}) = \frac{4G}{c^2} \int \Sigma(\vec{\xi'}) \frac{\vec{\xi} - \vec{\xi'}}{|\vec{\xi} - \vec{\xi'}|^2} d^2\vec{\xi'}, \tag{2.24}$$

where $\vec{\xi'}$ is the distance of $dM = \Sigma(\vec{\xi'})\, d^2\vec{\xi'}$ to the origin. We may also define the projected potential:

$$\psi(\vec{\xi}) = \int_0^{\infty} \Phi(\vec{\xi}, z) dz. \tag{2.25}$$

Considering that $\nabla^2 = \nabla^2_{\vec{\xi}} + \partial^2/\partial z^2$ and (2.18) combined with (2.23) we may write:

$$\nabla^2_{\vec{\xi}} \psi(\vec{\xi}) = 4\pi G \Sigma(\vec{\xi}). \tag{2.26}$$

The Green function for (2.26), which satisfies $\nabla^2_{\vec{\xi}} \mathcal{G}(\vec{\xi}, \vec{\xi'}) = 2\pi\delta^2(\vec{\xi} - \vec{\xi'})$ is

$$\mathcal{G}(\vec{\xi}, \vec{\xi'}) = \ln |\vec{\xi} - \vec{\xi'}|. \tag{2.27}$$

Thus the projected potential is given by:

$$\psi(\vec{\xi}) = 2G \int \Sigma(\vec{\xi}') \ln |\vec{\xi} - \vec{\xi}'| d^2\, \xi', \tag{2.28}$$

using the identity $\nabla_x \ln |\vec{x} - \vec{x}'| = \frac{\vec{x}-\vec{x}'}{|\vec{x}-\vec{x}'|^2}$ we may write the deflection angle $\vec{\hat{\alpha}}$ as:

$$\vec{\hat{\alpha}}(\vec{\xi}) = \frac{2}{c^2} \nabla_\xi \psi(\vec{\xi}). \tag{2.29}$$

This last equation indicates that the projected potential can be used to obtain the deflection angle, or, if the surface mass distribution is known, we may use it to determine the potential and thus $\vec{\hat{\alpha}}$. From (2.29) we may rewrite the lens equation as

$$\vec{\beta} = \vec{\theta} - \nabla_\theta \Psi(\vec{\theta}), \tag{2.30}$$

where we defined $\Psi = \frac{2}{c^2} \frac{D_{LS}}{D_{OS} D_{OL}} \psi$ and we changed the variable $\vec{\xi}$ to $\vec{\theta}$ by using $\vec{\xi} = \vec{\theta} D_{OL}$. From (2.30) we may notice that for each image θ there is a single source at $\vec{\beta}$. However, as (2.30) is nonlinear in θ, there may be several images for a single source located at $\vec{\beta}$.

2.6 Lensing Models

In this section we briefly review three lensing models of interest. The Singular Isothermal Sphere (SIS), which is a simple model for galaxy lensing, and other two models which are used in our Cluster Lensing Cosmology modelling, the Pseudo Isothermal Elliptical Mass Distribution (PIEMD) and its variation, the Dual Pseudo Isothermal Elliptical Mass Distribution (dPIE).

2.6.1 Singular Isothermal Sphere - SIS

Perhaps the simplest lens model besides the point source is given by the Singular Isothermal model whose mass distribution is given by

$$\rho(R) = \frac{\sigma_v^2}{2\pi G R^2}, \tag{2.31}$$

where σ_v is a parameter given by the unidimensional velocity dispersion of particles in an isothermal self-gravitating gas in equilibrium.

Despite this simple form and the divergence at the center. This model has been widely used for lenses on the galaxy scale. Indeed, it has been shown that this density profile is an excellent approximation to the mass distribution in early type galaxies from a vast and diverse set of observations as well from simulations (see, e.g., van de Ven et al, 2009). By integrating (2.31) one can obtain the surface density

$$\Sigma(\theta) = \frac{\sigma_v^2}{2GD_{OL}\theta}. \tag{2.32}$$

In this case, the deflection angle is given by

$$\hat{\alpha}(\theta) = \frac{4\pi\sigma_v^2}{c^2}, \tag{2.33}$$

which is independent of θ. Then, we may write the lens equation as

$$\vec{\beta} = \vec{\theta}\left(1 - \frac{\theta_E}{\theta}\right), \tag{2.34}$$

where the Einstein Radius θ_E is given by:

$$\theta_E = \frac{4\pi\sigma_v^2 D_{LS}}{c^2 D_{OS}}. \tag{2.35}$$

2.6.2 The Pseudo and Dual Pseudo Isothermal Elliptical Mass Distribution - PIEMD and dPIE

The Pseudo Isothermal Elliptical Mass Distribution (PIEMD, Kassiola & Kovner, 1993) is a simple isothermal-like aspheric model. The PIEMD main feature is that its potential, as well as its first and second partial derivatives, can be obtained analytically, which enables to derive deflection angles, distortions and time delays for any ellipticity. This advantage makes it very suitable to parametric approaches in Strong Lensing modeling. This model has been reported as a robust approach to describe Strong Lensing in clusters, sometimes with a

better fit than canonical Navarro-Frenk-White (hereafter NFW, Navarro et al, 1996, 1997) mass distribution. For instance, Grillo et al. (2015) found that the dark matter components of the Hubble Frontiers Field (HFF) galaxy cluster MACS J0416.1−2403 is better fitted by PIEMD models. For such model the projected mass density distribution is

$$\Sigma(R) = \frac{\sigma_v^2}{2G}\left(\frac{1}{\sqrt{R^2(\varepsilon) + r_{core}^2}}\right), \tag{2.36}$$

where $R(x, y, \varepsilon)$ is an elliptical coordinate on the lens plane, σ_v is the velocity dispersion, r_core is the core radius and ε is the ellipticity. Some variants of PIEMD have frequently been used in lensing analysis (see e.g., Caminha et al, 2016a; Grillo et al, 2015; Keeton & Kochanek, 1998; Kneib et al, 1996; Smith et al, 2005). One of the most common variants is the two component PIEMD with both a core radius, r_c and a scale radius, r_s known as dual Pseudo Isothermal Elliptical mass distribution (dPIE, Elíasdóttir et al, 2007). In the case of $r_c < r < r_s$, the 3-D profile $\rho(r)$ behaves as $\rho \sim r^{-2}$, though in the outer regions it falls like r^{-4}. The surface density which defines this model is given by

$$\Sigma(R) = \Sigma_0 \frac{r_c r_s}{r_s - r_c}\left(\frac{1}{\sqrt{r_c^2 + R^2}} - \frac{1}{\sqrt{r_s^2 + R^2}}\right). \tag{2.37}$$

Chapter 3

Morphological Analysis and Image Processing for Gravitational Arcs

Shape analysis and detection are fundamental issues in image processing field. The measurement of basic morphological quantities, such as the length and width of an object, is useful in many applications and may have multiple definitions.

In the case of Strong Lensing phenomena, another quantity that should be relevant to characterize the Gravitational arcs is the presence of a curvature center and determination of the curvature radius. This quantity is not directly provided by standard morphological estimators, such as those obtained from second moments of the light distribution (e.g., Bertin & Arnouts, 1996) or by fitting the object surface brightness with elliptical isophotes (Peng et al, 2010). Providing appropriate characterization tools for the objects detected in the image, such as those derived from the method presented here, is a major step in developing arcfinders (Bom et al, 2015, 2017) and for gravitational arc statistics (Meneghetti et al. , 2013). We have developed a novel technique to decompose shapes (images of objects) into a set of filaments on their intensity ridgeline, which allows one to define a length along the ridgeline and to determine a curvature center. Though applicable to many shapes, the technique is particularly appropriate for long and curved objects.

In the following, we describe the method to decompose elongated objects into a set of line segments. For concreteness, we will consider the object to be composed of a set of pixels with given intensity, as in a standard digital image. However, in principle, the method can

be applied to any intensity distribution, even if not pixelated. The only requirement is that the object should have a clearly defined boundary, in other words, the intensity must be zero outside the object.

3.1 Mediatrix Method

The Mediatrix method was originally designed to characterize and search for curved objects. It was inspired on a basic geometrical property of the perpendicular bisector of pairs of points on a circle, namely that these lines, for any set of pairs of points, intersect at the circle center. Therefore if an elongated object can be decomposed into a set of points along its longer direction, and if this object has a shape close to an arc segment, the perpendicular bisectors of pairs of these points will intersect in nearby points (i.e., close to the center of curvature). It turns out, however, that this method can be used to assign segments along the longer direction of elongated objects, i.e., to "filament" the object, or to determine its "spine", regardless of the presence of curvature. The key procedure to segment the object is to recursively obtain the perpendicular bisector of pairs of points on the object's image.

Given the points $P_1 = (x_1, y_1)$ and $P_2 = (x_2, y_2)$, the perpendicular bisector is a straight line $y = mx + b$ perpendicular to $\overline{P_1P_2}$ that intersects the segment at its middle point and whose coefficients are given by:

$$m = -\frac{x_2 - x_1}{y_2 - y_1}, \tag{3.1}$$

$$b = \frac{(y_1 + y_2) - m(x_1 + x_2)}{2}. \tag{3.2}$$

The Mediatrix method is a recursive method that operates in several iteration steps. Each step is a new Mediatrix level and, in principle, the method can be iterated up to an arbitrary level n. In the following, we describe the first few levels as an example (see Fig. 3.1).

In the first step, we determine the extreme points, E_1 and E_2 of the object (i.e., the two points most distant from each other). Several methods have been considered to determine

the extreme points of an object (see, e.g., Brandt et al., in prep.). Here we use the "farthest-of-farthest" method, by which E_1 is defined as the most distant point from a reference point on the object (e.g., the brightest pixel on the image or its geometrical center), whereas E_2 is defined as the pixel on the object farthest from E_1. Next, the perpendicular bisector of these two points is calculated. The first *Mediatrix point* M^1 is defined as the brightest pixel of the object along the perpendicular bisector. In practice, we take the brightest pixel located at a distance $d \leq \alpha \Delta p$ from the perpendicular bisector, where Δp is the pixel size and α is chosen as $\alpha = \sqrt{2}/2$. The first Mediatrix Point M^1 is shown in Fig. 3.1(A) for an arc-shaped object (more specifically, an ArcEllipse, Furlanetto et al, 2013b).

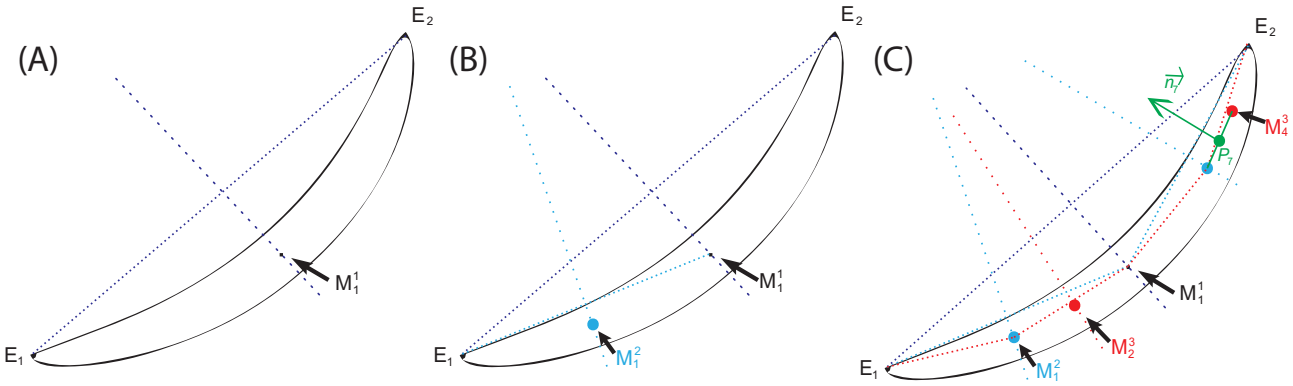

Figure 3.1: *Steps of the Mediatrix Filamentation method. After n iterations, the method determines a set of 2^n points defined by the maximum of intensity along the 2^n perpendicular bisectors and 2^n vectors perpendicular to neighbouring points with the magnitude given by the distance between these points. For clarity, only some points are shown on the figure, which illustrates the steps for $n = 3$.*

In the second step the perpendicular bisectors are now calculated with respect to (E_1, M^1) and (M^1, E_2). These two perpendicular bisectors define two other Mediatrix Points: M_1^2 and M_2^2 using the same criteria we used to define M^1 (Fig 1B). The upper index refers to the iteration level and the lower index is a label to identify the points. Proceeding to the third step, presented in Fig 1(C), we start from the previous set of Mediatrix Points M^1, M_1^2, M_2^2 and the two extremes E_1 and E_2. Those points are used to define new Mediatrix Points M_i^3 obtained, again, by picking the highest intensity pixel near the perpendicular bisector between two neighboring points. The algorithm may continue defining new Mediatrix Points M_i^j, corresponding to the i-est point in the j-est iteration level, in higher iteration levels until reaching a specified final step n. In Fig 1(C), we present the last step for $n = 3$ (as

in the previous panels some points were omitted not to crowd the figure). The collection of Mediatrix Points together with the two extreme points are then named *keydots*. From the keydots, the object is decomposed in $N = 2^n$ segments or filaments. Each segment connects a keydot to its neighbors. The algorithm outputs a set of vectors $\vec{n}_j$, where j varies from 1 to N. Those vectors are perpendicular to the segment that connects a keydot to its neighbor with origin in the midpoint of its segment and norm equal to the length of this segment. This is shown in Fig. 1(C) for $\vec{n}_7$, where $|\vec{n}_7|=|\overline{M_4^3 M_2^2}|$.

3.2 Features derived from the Mediatrix Method

Using the outputs of the Mediatrix filamentation method, for an iteration level k, the object length is defined as:

$$L_k = \sum_{j=1}^{N} |\vec{n}_j| = \sum_{j=1}^{N} l_i. \tag{3.3}$$

One may define an arc width W_k (in the k^{th} level) by the following expression

$$W_k = \frac{4A}{\pi L_k}, \tag{3.4}$$

where A is the object area in pixels derived from the object segmentation, i.e., the number of pixels labeled as part of an object by a segmentation and labeling algorithm. This expression is taken from the ellipse-area relation but is still exact for other shapes, such as an ellipse whose main axis is distorted into an arc segment (precisely the shape used to illustrate Fig. 3.1, see Furlanetto et al, 2013b).[1] and is an excellent approximation for a specific solution for gravitational arcs (Pacheco et al. in preparation).

For arcs constructed from circle segments, as in the case of the object of Fig. (3.1), all perpendicular bisectors intercept at the center of curvature. In a more general case, we may define the center of curvature as the point closest to all perpendicular bisectors. We thus define the "*M-statistic*" function $M(\vec{r})$ as the mean of the distances from $\vec{r}$ to the perpendicular bisectors of all Mediatrix segments (i.e., the average distance to the lines

[1]Some authors use the relation $W = A/L$, which is more suited to a boxy, i.e., closer to rectangular, shape (see, e.g. Meneghetti et al, 2013, for discussions). Throughout this contribution, we will use definition (3.4) and will not address which of the two gives a better representation of the width of real objects.

spanned by the vectors $\vec{n}_i$). Then we have

$$M(\vec{r}) := \frac{1}{N}\sum_{i=1}^{N} |\vec{d}_i(\vec{r}, \vec{n}_i)|^2, \tag{3.5}$$

where $|\vec{d}|$ is the distance of point $\vec{r}$ to the lines defined by $\vec{n}_i$. Therefore the center of curvature is defined as the point $\vec{r_0}$ in the plane that minimizes the function $M(\vec{r})$. In the case of a circle arc, the procedure above yields the circle center. However, this method is also well suited for more generic shapes.

If the object has a well-defined curvature center, not only the function $M(\vec{r})$ will have a clear global minimum, but also small deviations from r_0 lead to a substantial increase in $M(\vec{r})$. We treat $M(\vec{r})$ analogously to a "chi-square function" and define a Confidence Region (CR) such that

$$M(\vec{r}) - M_0 \leq \sigma_m, \tag{3.6}$$

where σ_m is an arbitrary parameter. After some visual assessment, for the images used in this thesis we found a reasonable value of $\sigma_m = 1$.

3.3 Tests in a controlled sample

To test the method, and in particular its ability to recover the parameters of arc-like objects, we ran it on a controlled sample, for which these parameters are known. To that end we use the PaintArcs method (Furlanetto et al, 2013b), which produces a surface brightness distribution mimicking arcs from an analytical prescription. The isophotes are given by ArcEllipses, which are ellipses whose main axis is curved into an arc segment. In polar coordinates centered on the center of curvature, the ArcEllipse is defined by

$$\left(\frac{r_c\,(\theta - \theta_0)}{a}\right)^2 + \left(\frac{r_c - r}{b}\right)^2 = 1, \tag{3.7}$$

where r_c is the ArcEllipse curvature radius of curvature (i.e., the radius of the circle on which the ellipse is distorted), θ_0 is the position angle of the center of the ArcEllipse, b is

the its half-width (computed at the center) and a is its half-length. The resulting shape is as illustrated in Fig. 3.1. The area of this figure is simply given by πab, exactly as for an ellipse (Furlanetto et al, 2013b).

Now we can take any profile, such as a Gaussian, for example, and make the argument of this function constant over ArcEllipses, i.e. we construct a surface brightness distribution with the chosen radial profile and ArcEllipses isophotes. The resulting image looks like a gravitational arc, and this prescription (ArcEllipse+radial profile) has been used to fit arcs in simulations and on real data (Furlanetto et al, 2013b). We are thus able to produce arcs controlling all their parameters, such as curvature radius R, length $2a$ and width $2b$ and position, providing a perfect sample for testing the Mediatrix method. As the arcs can be added, i.e., "painted" on background images for a number of application, this prescription was dubbed PaintArcs (Furlanetto et al, 2013b). PaintArcs has been used to add simulated arc images on the so-called Data Challenges of the Dark Energy Survey. It is interesting to note that while the ArcEllipse is a pure geometrical construction with no connection to the physics of gravitational lensing, it does provide an excellent approximation for images of circular sources lensed by a Singular Isothermal Sphere (Pacheco et al., in preparation).

To carry out our tests we use a sample of arcs produced by PaintArcs which are pixelated and have their counts scaled to reproduce a given magnitude. The sample has ~ 600 images with magnitudes[2] of 22, 22.5, 23.0 and 23.5. The arcs curvature radius, r_c are given by $5.0''$, $10.0''$ and $15.0''$ while their L/W are 2.0,4.0, 7.0 and 10.0. We work in two samples with different observational conditions. The first is the pure arcs (hereafter PA), i.e. with no observational effect applied. The second sample have background noise addition (hereafter BN), we assume a background comparable to Smith et al. (2005), and since we are mimicking the sample to be a space based like we did not include the PSF in this application example.

To add a constant background we selected an visually empty area in Smith et al. (2005) image and calculated its mean. We use this value to add a constant background. Then we assign a Poisson noise by sampling each pixel value from a Poisson distribution with mean given by the pixel value.

To make the object segmentation we adopted a simple algorithm: for PA sample we pick

[2]This range roughly corresponds to the arcs studied in the survey Smith et al. (2005).

all pixels brighter than 1/10 the maximum pixel value and defined it as a single object. For BN sample, which included a constant background and noise addition, we selected all pixels above the mean $+1\sigma$ values of the image histogram. We did not make any fine tuning in the detection parameters.

In the next subsections, we apply the Mediatrix method for both sample of arcs (PaintArcs with and without the addition of background and noise). We assess its ability ti recover arc parameters, in particular curvature radius and the lenght-to-width ratio L/W. The curvature radius R is defined as the distance from the center of curvature $\vec{r_0}$ from the minimization of $M(\vec{r})$ to the arc center given by the first Mediatrix point M_1^1, whereas L/W is determined from the definitions of L and W in Eqs. (3.3) and (3.4). In the PaintArcs simulated images, these quantities correspond exactly to r_c and a/b. Therefore, we have a truth table for comparing the values from Mediatrix to the input values used to simulate the arcs. Notice that we compare L/W and not L and W individually. These quantities are strongly dependent on the object boundary, i. e., on the chosen segmentation. If we decided to cut the object for pixel threshold values different from a tenth of the peak values (in the PA case) or other multiples of σ (in the BN) case, the values of L and W would change significantly. However, due to the self-similarity of the PaintArcs isophotes the ratio L/W should be robust (and equal to a/b). We apply the Mediatrix filamentation method and generate the outputs for each iteration level up to $n = 5$, including the keydots and normal vectors $\vec{n_i}$, the length L_n and width W_n, the curvature center r_0 and the confidence regions. Some examples are given in Fig. 3.2. We may notice in the bottom panels of the Fig. 3.2 that some objects are poorly detected in BN sample which compromises the curvature center determination

From our first curvature analyses and after visually inspecting the results we noticed that the vectors in the image borders, i.e. the vectors defined by one of the extrema, degrade the determination of r_0. This is not an unexpected result, since the extrema are very sensitive to the segmentation, unlike the others Mediatrix points. If the arcs edges are not sharp (i.e., for fat arcs) or for objects that span large angles ($L/R > \pi$), E_1 and E_2 will not correspond to arc extremities. Therefore, we choose to eliminate these 2 points from the analysis of the center of curvature and curvature radius, as illustrated in 3.2. Of course this can only be done for the Mediatrix level $n > 1$.

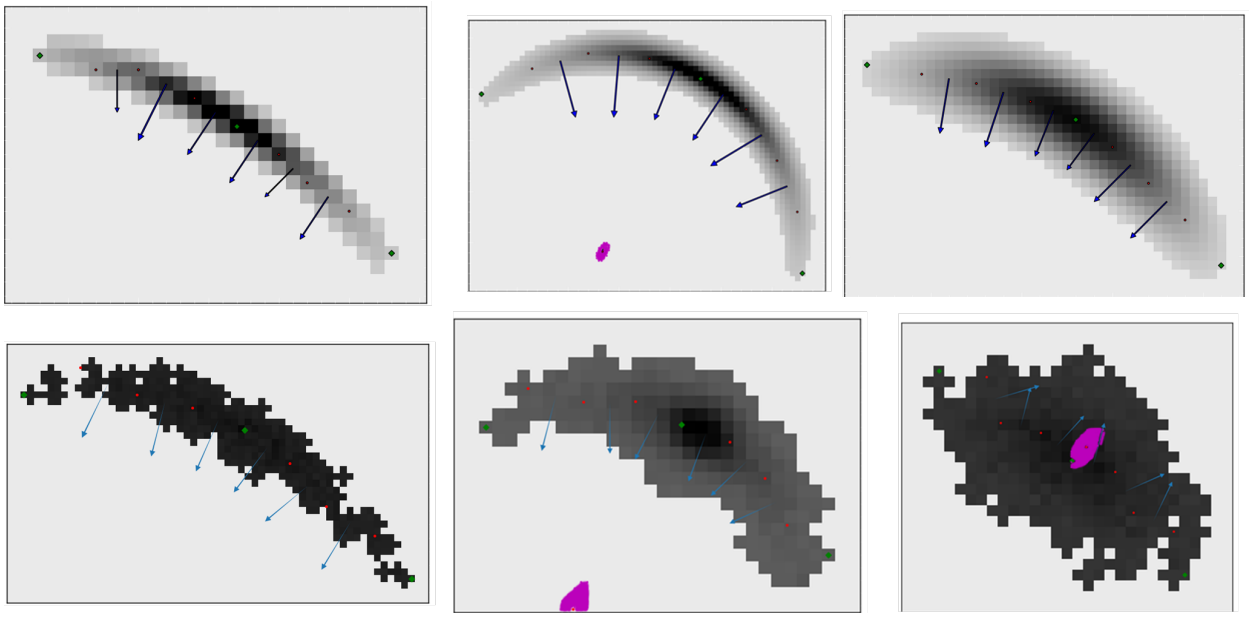

Figure 3.2: *Examples of PaintArcs images after Mediatrix Analyses for $n = 3$. Top: Pure Arc Sample (PA). Bottom: Background and Noise (BN). The keydots, except the extrema and the center (M_1^1), are shown as [red] circles, the arrows are the $\vec{n}_i$ normal vectors. In some cases, the curvature center $\vec{r_0}$ [red losangle] and confidence regions (CR) are shown. (bottom left).*

3.3.1 Results for the Pure Arcs Sample

In Fig. 3.3 we present the results for the determination of the curvature radius R Mediatrix as a function of the input curvature radius r_c for the PA sample along with its fractional deviation with respect to the PaintArcs inputs. As we have 3 values of r_c in our sample, we show the results for all arcs for the three corresponding values of R and all values of the other parameters. The error bars are the standard deviations. We see that R is a decreasing function of the iteration level n. The results for $n = 1$, which represent a standard method used in the literature are all biased high. The level $n = 2$ already shows interesting results, but the optimal value in this sample is $n = 3$ with smaller error bars. For $n = 4$ and especially $n = 5$ the values are biased low and the error bars increase probably due to the excess of divisions such that the directions are affected by the pixel scale. The $n = 3$ case shows less than 10% deviation for all values of the curvature. For instance, the error bar for the lowest curvature $R = 5''$ is $0.3''$, which is roughly the pixel size.

We have also split the sample into two size groups: low-L (hereafter LL) containing objects from 10 pixels to 50 pixels in length (or $\sim 3''$ to $\sim 14''$) and high-L (hereafter HL), containing objects from 100 to 150 pixels (or $27''$ to $\sim 40''$). We present the results

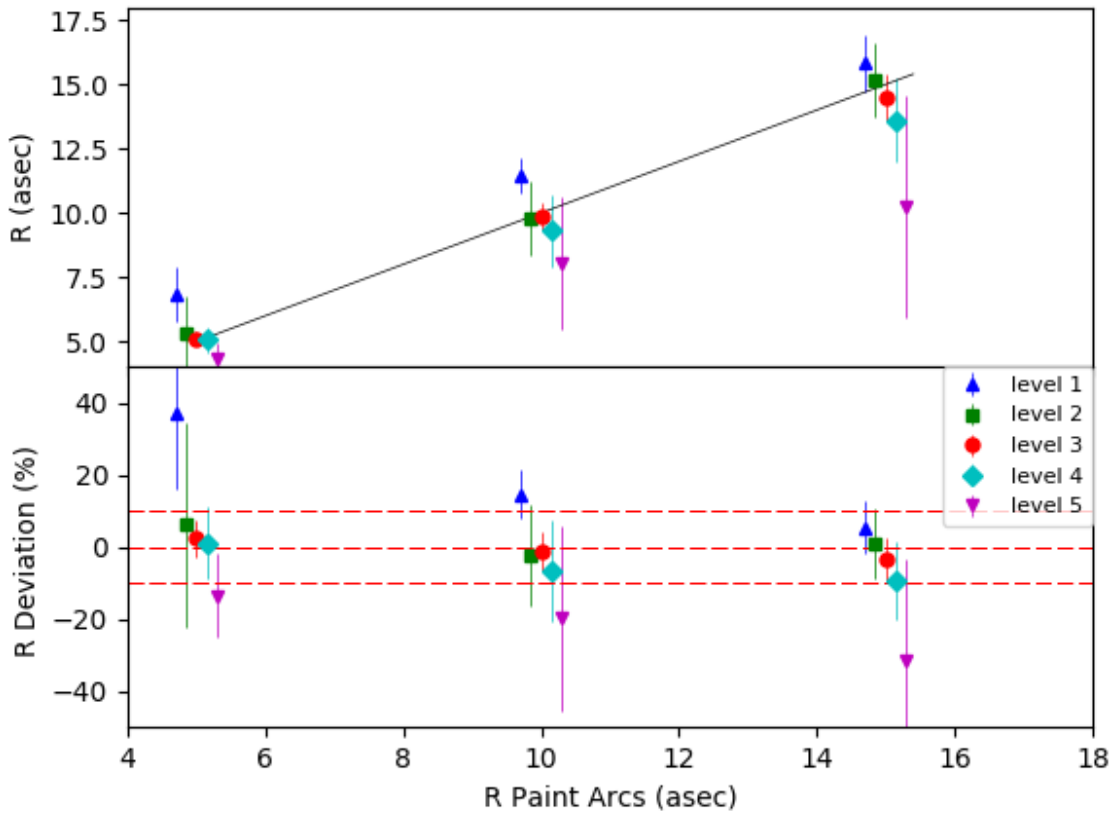

Figure 3.3: *Curvature radius R obtained from Mediatrix (up) and fractional deviation from the input PaintArcs values (bottom) in PA sample for different levels of Mediatrix iterations. The red dashed lines indicate the ±10% deviations. The points were shifted horizontally for clarity.*

for curvature in both groups in Fig. (3.4), as expected the Mediatrix loses its precision for small objects. The constraints in level 2 are more accurate than level 3 for curvature radius $R = 10''$ or $R = 15''$ showing that it does not help to further decompose small objects due to the pixel size. From the figures 3.4a and 3.4a is clear that by using the extrema (level 1) ones always bias the results for both the HL and LL to higher values of R. Also as expected. The method is more precise for large objects as they have a better resolution and stand more divisions. Nevertheless, $n = 5$ still gives results that are biased low.

In Fig. 3.5 we show L/W. As expected, L/W is an increasing function of the iteration level. Indeed, by construction, L can only increase with i, while W is given by Eq. (3.4), whose the area of the object is fixed. In any case, the dependence with i is much weaker than in the case of curvature radius. We see from the bottom pannel of 3.4 that all results are compatible with the PaintArcs input within their standard deviations (except for the

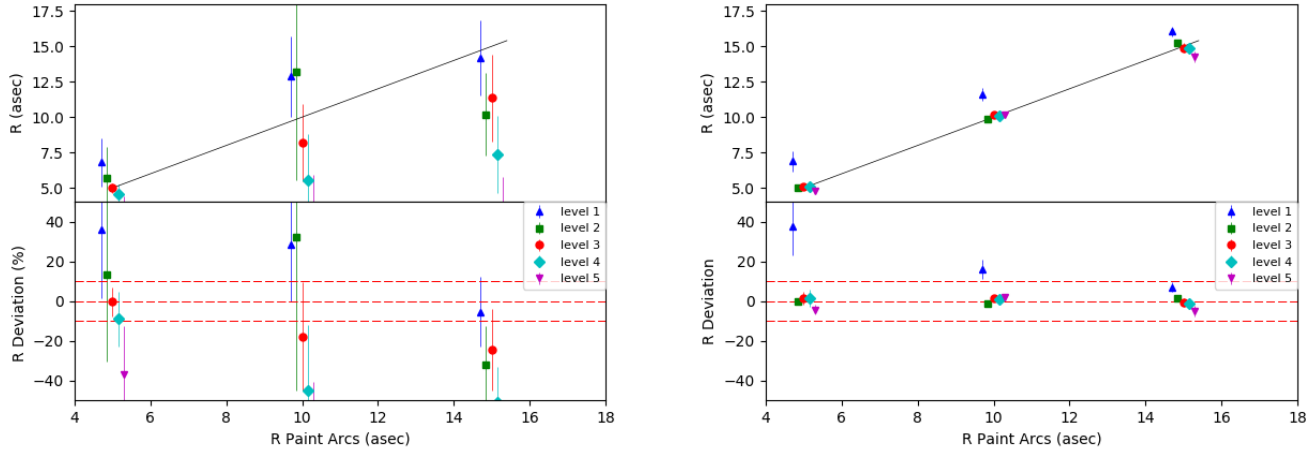

(a) *Low-L subgroup* **(b)** *High-L subgroup*

Figure 3.4: *Curvature radius R and deviations from the input PaintArcs values in the PA sample for different levels of Mediatrix iterations in two subset of arcs, the low L and high L. The red dashed lines indicate the* 0 *and* ±10% *deviations.The points were shifted horizontally for clarity.*

smaller L/W and $i = 1$). Here, again, $i = 2$ or 3 seem to yield the best performance. Also, as before $i = 5$ gives an exceedingly high variance.

3.3.2 Results on the Arc sample with added Background and Noise

We present the results of the determination of curvature radius for this sample in Fig. 3.6. We see that the Noise and Background addition have a substantial impact on the R determination. In this case, both the scatter is tremendously increased, and the means have a larger deviation from the true value. Contrarily to the PA case, for which R was both accurately and precisely recovered for $i = 3$. There is no iteration level that provides reliable results. Nevertheless, $i = 2$ and $i = 3$ produce the best results with a mean bias of $\sim 20\%$.

If one considers the HL and LL subsamples, as shown in Fig. 3.7, we conclude that the method fails to define a reliable curvature center in LL sample. On the other hand, R is correctly recovered for $i = 3$ in this case with a small mean deviation. For the highest curvature, which corresponds to largest errors we obtained, for level 3, $R = 13.4 \pm 2.0$ while for $R = 5.0$ we get 5.0 ± 0.6, i.e. with errors bars $\sim 10\%$.

Due to the presence of noise and background, it makes sense to look at the results as a function of the signal-to-noise of the object or, alternatively, as a function of their magnitude.

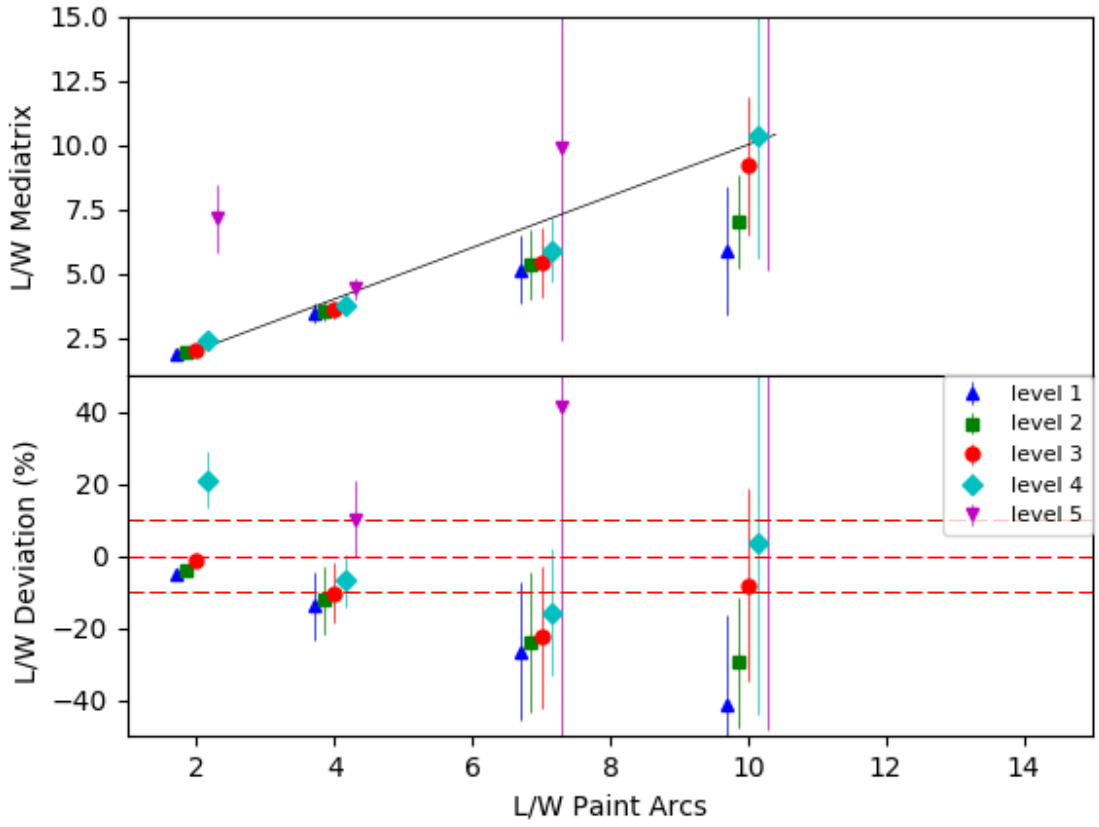

Figure 3.5: *Length to width ratio, L/W and fractional deviations from the PaintArcs input values (a/b) in the PA sample for different levels of the Mediatrix Iterations. The red dashed lines indicate the* 0 *and* $\pm 10\%$ *deviations. The points were shifted horizontally for clarity.*

The results for the brightest arcs, with magnitude 22 are shown in Fig. 3.8. In this case, the results are highly improved when compared to Fig. 3.6 and are similar to the ones in HL, which may indicate that the main issue in the determination of R is a reliable segmentation even if we already eliminate the extreme points. We made the same test for magnitude 23, but we obtained results similar to the ones in Fig. 3.6.

In Fig. 3.9 we present the results for L/W in the BN sample. Comparing to Fig. 3.5 the results are surprisingly similar, or even better than in the PA case. By construction, L/W is a growing function of i, and, as expected, the scatter is larger for L/W than in the PA case. However, the mean is even closer to the PaintArcs input than for the PA (in all cases, except the smaller L/W). Here $i = 2$ provides the best results, $i = 3$ and $i = 1$ are still acceptable, 4 is consistently worse, and $i = 5$ should not be used at all.

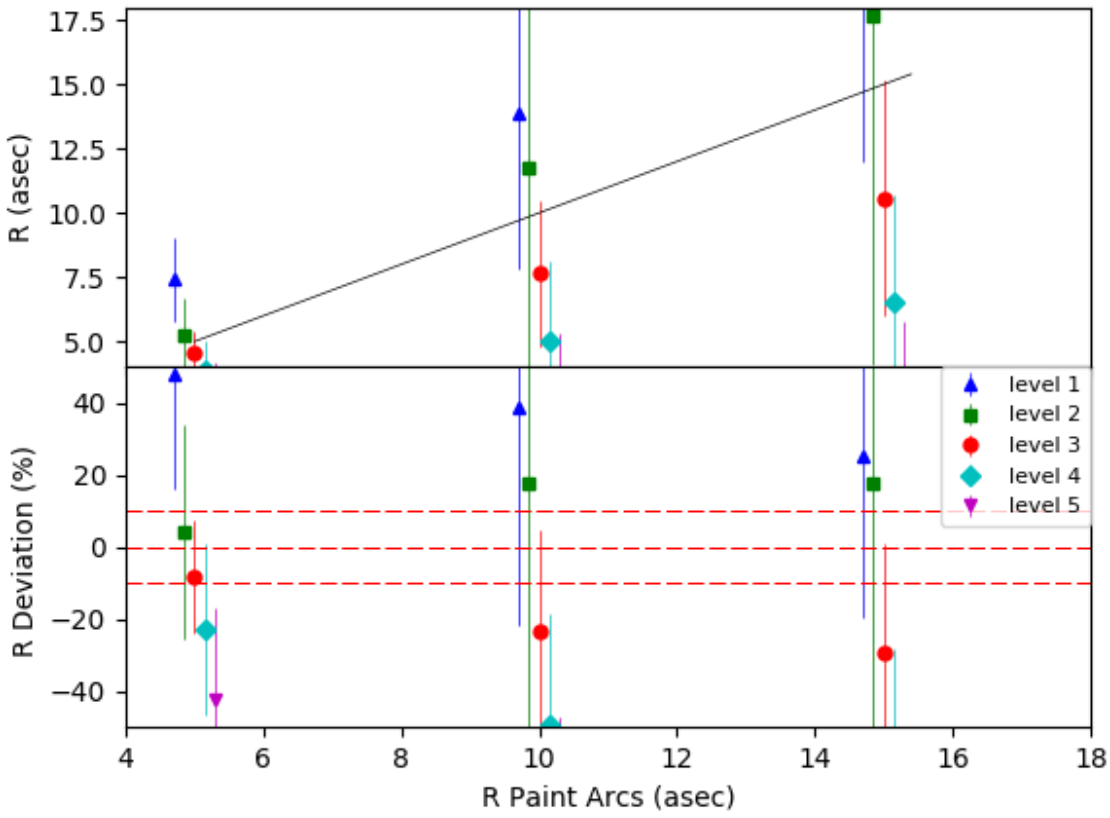

Figure 3.6: *Curvature radius R and deviations from the input paint arcs values in BN sample for different levels of Mediatrix Methods. The red dashed lines indicate the ±10% deviations. The points were shifted horizontally for clarity.*

3.4 Concluding Remarks on morphology and arc features

The Mediatrix filamentation method is a technique to decompose elongated shapes into filaments, which enables one to define a number of morphological parameters, including the length and curvature center. In particular, it provides means to estimate the confidence of the curvature center.

In this chapter we apply the Mediatrix method to a sample of simulated arcs shapes using the PaintArcs method, providing a diverse set of images with different length-to-width ratios, curvature radius, and magnitudes, providing a controlled sample to test the method. Firstly we report that the use of extreme points leads to a strong bias in the curvature radius constrains.

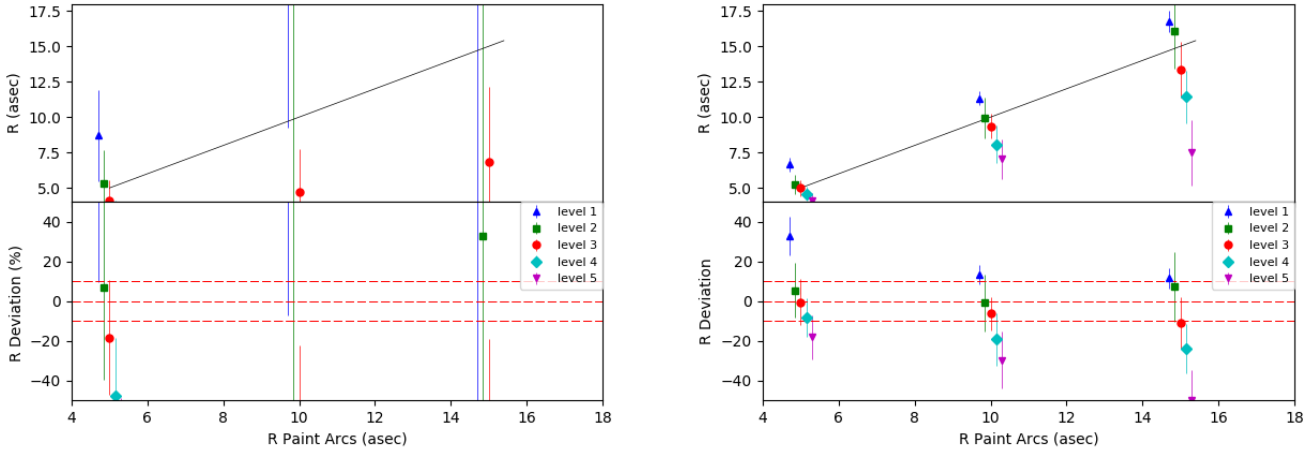

(a) *Low-L subgroup* **(b)** *High-L subgroup*

Figure 3.7: *Curvature radius R and deviations from the PaintArcs input values in the BN sample for different levels of the Mediatrix iterations in two subsets of arcs, the low-L (left) and high-L (right). The red dashed lines indicate the* 0 *and* $\pm 10\%$ *deviations. The points were shifted horizontally for clarity.*

We firstly worked on the pure arc, PA, images (i.e. with no background and noise) segmented using all pixels brighter than a tenth of the brightest one. We found that the recovered curvature radius as a strong variation with the iteration level n. In particular, $n = 3$ provides excellent results with less than 10% scatter, which is less than the pixel scale for $R < 10''$ and a mean precision with virtually no bias.

Regarding the length-to-width ratio, L/W the dependence with n is smaller. The scatter increases with L/W ranging from $\sim 5\%$ to $\sim 40\%$ (except for $n = 5$). Overall, the best results are obtained with $n = 2, 3, 4$, with mean deviations $\lesssim 10\%$ (for $L/W = 2, 4$).

Then we studied R and L/W in the sample with noise and background added. The segmentation is, of course, more subtle in this case. We considered all pixels with values 1σ above the background as part of the object.

The results for R are strongly degraded concerning the PA case. Both the scatter is significantly larger, and the mean values have a stronger deviation with respect to the input values. The best results are obtained for $n = 2, 3$ but the mean values deviates $\sim 20\%$ in those cases. The situation is much improved for both larger arcs (HL sample) or the brightest ones ($mag = 22.0$) for which the mean values of R are $\lesssim 10\%$.

On the other hand, the results for L/W are much less sensitive to the presence of noise and

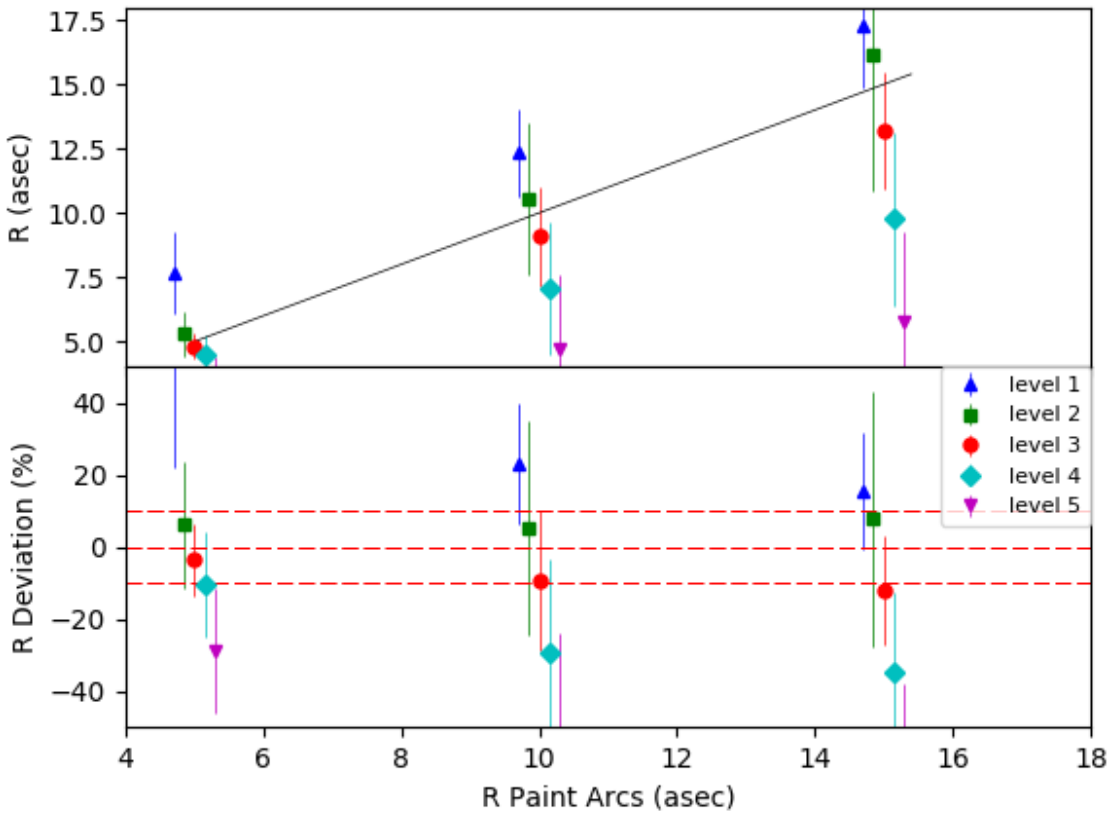

Figure 3.8: *Curvature radius R and deviations from the PaintArcs input values in a sample containing sources with mag* ≤ 22.0 *for different levels of the Mediatrix iterations. The points were shifted horizontally for clarity.*

background. The scatter are much less susceptible to the presence of noise and background. As expected the scatter is larger, but the mean values of L/W are even closer to the input ones than for the PA case. We will carry out a few tests aiming to improve the results of the BN case. As we saw that the brighter and larger objects yield better results, this hints to selecting higher Signal-to-Noise regions. To minimize the effect of noise, we will convolve the images with a small kernel to make them smoother.

We have not used the confidence region (CR) in our statistical evaluations. However, we stress that visually, the CR has a very distinct behavior for straight or curved objects. For arcs with a clear curvature, the CR has a small area and small ellipticity, showing that the $M(\vec{r})$ function has a well defined minimum. For more straight objects, $M(\vec{r})$ still has a minimum (as there is a dispersion on the $\vec{n_i}$ directions), but the CR is much larger and very elongated in the direction perpendicular to the arc. In this case $\vec{r_0}$ gets closer to the

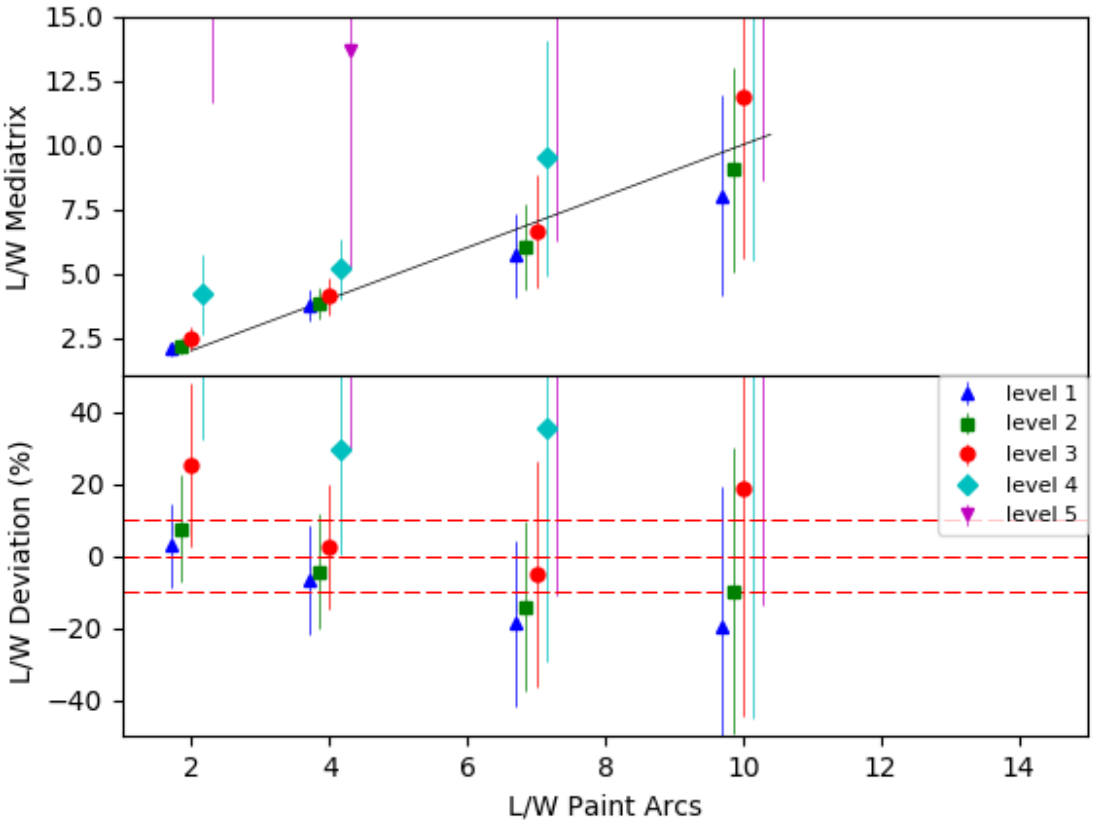

Figure 3.9: *Length to width ratio, L/W and fractional deviations from the PaintArc input values in BN sample for different levels of Mediatrix iterations. The red dashed lines indicate the* 0 *and* $\pm 10\%$ *deviations. The points were shifted horizontally for clarity.*

object center as k increases and the CR starts intersecting the object. This effect is more pronounced in the images with noise and background since the presence of minima is a consequence of the fluctuations.

Therefore, the "M-statistic" $M(\vec{r})$ is a good indicator for the presence of curvature. On one hand it takes into account the details of the object shape (as opposed to just using the object extremities and brightest pixel, for example), through the many vectors $\vec{n_i}$ of the Mediatrix decomposition, and, on the other hand, it has a very distinct behavior for curved objects. This function not only provides an estimate for the center of curvature location, but also, and more importantly, gives a measure of the significance of the presence of such center. A more systematic and quantitative study is still needed to determine the optimal values of σ_m in Eq. 3.6 and the threshold on the CR parameters to define the significance of the curvature. This may depend on several factors, including the image properties, and is

left for subsequent work.

The Mediatrix method may provide interesting discriminators for gravitational arcs, especially by combining its outputs. This motivated the development of a gravitational arc finder based on this approach, which is discussed in the next chapter (see also Bom et al. , 2015, 2017).

Two important quantities to characterize gravitational arcs are their length L and width W (and the derived ratio L/W). One standard definition of L is the sum of the distances from the brightest arc pixel to the two arc extreme points, E_1 and E_2 (e.g., Luppino et al, 1999), while W is often defined from the area of the arc, as discussed in Section 3.2. In most cases, this definition of L is very close to L_1, the length after the first Mediatrix iteration. In principle, the Mediatrix fillamentation allows for a more accurate determination of the length along the arc. However, it is easy to see that significant differences are not expected for objects with simple morphology. In fact, for objects whose intensity ridgeline has the shape of an arc of a circle, we expect the difference between Mediatrix iterations to be the largest when the angle spanned by the arc with respect to the curvature center is π.

It must also be said that the filamentation method is rapid, such that applying the Mediatrix decomposition to a large set of objects in astrophysical images has a low computational cost. The method is well suited for gravitational arcs but could be useful in many other astronomical applications, such as for interacting galaxies, planetary nebulae, etc. In the examples of this work, the objects show a well-defined "main direction" having a surface brightness distribution with a clear "spine". However, the method can be trivially extended to more general situations. For example, instead of using the object extrema as the first Mediatrix step, other definitions for the first step can be used for objects without a clear single preferred direction, such as objects with several tips. In this case, each pair of tips will define a different set of Mediatrix filaments and the final filamentation can be constructed as the combination of them. For binary images, where the pixels have all the same value, the midpoint of the pixels along the perpendicular bisector can be chosen as Mediatrix points, instead of the brightest pixel along this line.

From gravitational lensing theory, it is known that the curvature center of the arcs and the center of mass of the lens *do not* need to coincide (indeed, there are straight arcs, etc).

Lensing systems may have lots of matter clumps, for instance, the curvature center may be affected by a perturber galaxy and not point to the center of cluster halo in which the galaxy is embedded. However, we expect that the mean curvature center will be close to the lens center. Thus the Mediatrix curvature radius might be used as an estimator for Einstein Radius and therefore to the mass inside the Einstein Radius. This remains to be tested using arcs from lensing simulations and real data, when multiple images are available to carry out lens inversion. This is currently being implemented and under investigation in the SOAR GRavitional Arc Survey arc sample (Makler et al. in prep.).

Chapter 4

Gravitational Lens Detection

4.1 Visual Inspection

Several algorithms have been proposed for the automated detection of Strong Lenses. However, as discussed in Chapter 1, none of them emerged as a definitive method for lens finding, and a further visual inspection on the candidates is still needed. In this section, we discuss the visual inspection performed on the Dark Energy Survey Science Verification (hereafter SV) data (Nord et al, 2015). Since the SV area is a considerably small, a visual assessment could be done in a reasonable amount of time by a small team of inspectors, including the author. Also, visual inspection is likely to recover high-ranking candidates that would be found in different automated methods without the bias due to premises in the arcfinding algorithms. For instance, Horesh et al. (2005) search for thin and elongated objects only, while Bom et al. (2017) search for curved objects not necessarily with high elongation. Nevertheless, there is a bias towards larger Einstein radii, which are easier to identify through visual inspection.

The criteria to define a lens candidate was based on the morphology and color of the objects. Our team searched for objects with clear curvature, ring-like features and multiply imaged sources. As galaxies in higher redshifts are bluer due to high star formation and Luminous Red Galaxies (LRGs) are among the most massive, we search in particular for blue sources associated with red galaxies. Though red sources have also been identified.

Two types of visual scan were performed: a non-targeted search in the SV area ($\sim$ 250 sq.

deg.) and a targeted search around previously identified galaxy clusters. The non-targeted search was done by roughly 20 inspectors who looked at PNG images. Each image combines the *g, r, i* filters to produce a false-color image. Two targeted searches were performed. The first one in 67 clusters identified in the SPT SZ survey (Bleem et al, 2015) and the second one on 374 galaxy clusters with richness > 50. Those clusters were detected using the red-sequence Matched-Filter Probabilistic Percolation cluster-finder algorithm (redMaPPer; Rykoff et al, 2014). The searches were combined, and the candidates were ranked from 1 to 3, with 1 denoting least likely to be a lens system, and 3 the most likely. The search results yielded 53 high-quality candidates, i.e. rank 3, of which 24 were considered appropriate for spectroscopic follow-up and had never been identified as lensing systems before.

The spectroscopy was acquired by the Gemini Multi-Object Spectrograph (GMOS; Hook et al. , 2004) and by the IMACS multi-object spectrograph (Dressler et al, 2011) on the Magellan/Baade Telescope. From the 24 candidates, 21 have been observed within the allocated time and six were confirmed as lensing systems. The confirmed candidates are shown in Fig. 4.1. We present the main lensing features in table 4.1. From the observed sample, in 9 of them, it was not possible to define a continuum emission, 4 have no discernible features and 2 were confirmed as not lenses.

It is worth noticing that two of the systems have galaxies that are notably interesting. DES J0221-0646 and DES J0446-5126 have source galaxies at redshifts $z = 2.7251$ and $z = 3.22086$, respectively. Due to the magnification effect provided by lensing, these galaxies are among the brightest observed galaxies (in their apparent magnitude, due to the lensing) in their redshift ranges and may provide relevant information into the star formation history and galaxy formation at these cosmic epochs.

4.2 The Mediatrix arcfinder algorithm

Due to the many applications of Strong Lensing and the large amount of available data, several automated methods to find Strong Lensing/arcs have been proposed in recent years. Most focused on “pattern recognition”, i.e., on identifying shapes that look-like gravitation lensing, in particular arcs, thin and elongated structures (e.g., Alard, 2006; Horesh et al, 2005;

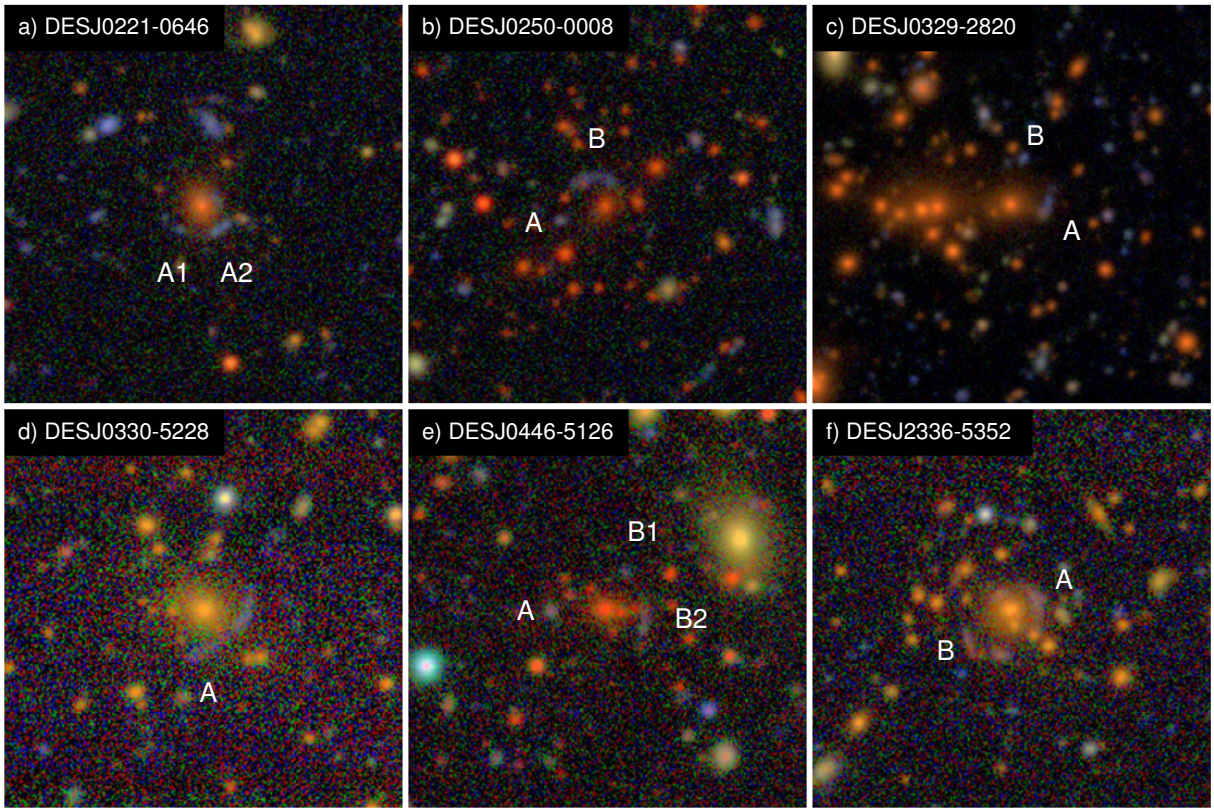

Figure 4.1: *Color co-added DES images of the six systems confirmed in the SV visual inspection a) DES J0221-0646, b) DES J0250-0008, c) DES J0329-2820, d) DES J0330-5228, e) DES J0446-5126, f) DES J2336-5352. The lensing features are labeled by the letters. Figure reproduced from (Nord et al, 2015).*

Lenzen et al, 2004; More et al, 2012; Seidel & Bartelmann, 2007), sometimes requiring also a degree of curvature (e.g., Estrada et al, 2007; Kubo & Dell'Antonio, 2008). Maturi et al. (2014) combine this approach with a multi-colour selection of the sources. Marshall et al. (2009) use lens inverse modelling to find strong lenses, i.e., assume that a given object in an image is a consequence of lensing and determine whether the lensing solution is favoured by the data. More recently, new arc finders have been proposed that subtract the lens candidate (usually Early-type galaxies) light distribution, either using two bands, as in Gavazzi et al. (2014), or by modelling the lens in a single band, as in Joseph et al. (2014) and Brault & Gavazzi (2015). The residuals are then investigated, using either their shapes (Joseph et al, 2014; Paraficz et al, 2016), by color selection (Gavazzi et al, 2014), or with inverse modeling (Brault & Gavazzi, 2015).

Due to blending issues, the lens subtraction approach is very frequent for galaxy-scale lenses, especially when observed from the ground, as the arcs can be embedded in the galaxy's

Table 4.1: *Lensing Features*

System ID Source Image ID	Spectral Features	Redshift	Einstein Radius $\theta_{\rm E}$ ($''$)	Enclosed Mass $M_{\rm enc}$ ($\rm M_\odot$)
DES J0221-0646		0.672 ± 0.042		
A1	Lyα	2.7251 ± 0.0008	5.0 ± 1.4	$7.5 \pm 4.7 \times 10^{12}$
A2	Lyα	2.7241 ± 0.0008		
DES J0250-0008		0.841 ± 0.042		
A	[OII]3727	1.2081 ± 0.0004	6.6 ± 1.1	$3.7 \pm 3.0 \times 10^{13}$
DES J0329-2820		0.655 ± 0.033		
A	[OII]3727	0.7963 ± 0.0001	7.2 ± 1.4	$1.6 \pm 0.9 \times 10^{13}$
B	[OII]3727	1.2976 ± 0.0003		
DES J0330-5228		0.463 ± 0.046		
A	[OII]3727	1.4541 ± 0.0004	6.1 ± 1.5	$9.0 \pm 3.7 \times 10^{12}$
DES J0446-5126		0.746 ± 0.047		
B1	Lyα	3.2068 ± 0.0010	7.0 ± 1.5	$1.6 \pm 0.9 \times 10^{13}$
B2	Lyα	3.2086 ± 0.0011		
DES J2336-5352		0.530 ± 0.075		
A	[OII]3727	1.1528 ± 0.0006	5.0 ± 1.5	$8.6 \pm 7.7 \times 10^{12}$
B	[OII]3727	0.8972 ± 0.0004	8.6 ± 1.9	$3.5 \pm 3f3 \times 10^{13}$

Notes. Lensing features of confirmed systems. We show the DESDM object ID's for lenses, the source image IDs, names of spectral features, photometric redshifts of lenses $z_{\rm l}$, spectroscopic redshifts of sources $z_{\rm s}$, an Einstein radius for each source image $\theta_{\rm E}$, and the resulting enclosed masses $M_{\rm enc}$. The main spectral features are all emission lines. Table reproduced from (Nord et al, 2015).

light. On the other hand, it is less critical for arcs on cluster scales, which span larger angular sizes than the galaxies and the PSF.

Most lens finders in the "pattern recognition" category use sets of measurements on the objects (such as ellipticity, length, L, width W, etc.) to determine whether they are lens candidates or not. They usually employ hard (i.e. fixed and mutually independent) cuts, whose values may be arbitrarily assigned or tuned using data or simulations. However, given the diversity of lensed sources properties (shapes, sizes, S/N ratios, etc.) and their physical origin, different cuts could perform better in various regions of the multi-dimensional space of lensed source parameters. For example, on cluster scales lensed sources may be very elongated, with several arcs but not necessarily with a clear curvature, while on galaxy scales lensed sources are not as drastically elongated but exhibit a clear curvature. Therefore, a flexible criterium based on a combination of parameters may be more efficient than applying hard cuts. This is a typical situation where machine learning methods can be extremely helpful. A suitably trained algorithm can then classify the objects into lenses or not, given a set of input images or values for the object features. Such training can be carried out either

on real data (on objects previously known to be arcs) or using simulations, by feeding the algorithm with a large set of lensing and non-lensing samples. This process is characteristic of supervised learning methods, the most well-known of which being the Back Propagation Artificial Neural Network (ANN; Rumelhart et al, 1988; Williams & Hinton, 1986).

As important as the choice of the classification method and its configurations is the selection of the set of input parameters. In this work, we concentrate the AMA algorithm to find for arc features. Thus we adopt measurements derived from the Mediatrix Filamentation Method presented in chapter 3 (Bom et al, 2016a,b), a novel iterative technique well suited to find arc-like shapes such as the ones from strong lensing.

Therefore, the purpose of this section is to construct an ANN gravitational arc finder based on the Mediatrix Filamentation Method, or *ANN Mediatrix Arcfinder* (AMA) for short to detect a sample of strong lensing candidates. We use a sample of simulated gravitational arcs and a sample of non arcs from HST images to train and validate the ANN. This sample is used to pin down a few configurations among the many possible choices involved in the ANN detection process: the types of images used for the training, the selection of inputs given to the ANN, the number of neurons, and the final threshold for classification. As an illustration of the application of the method to real data, we consider four galaxy cluster images from HST and run the AMA on them, comparing the results with the training and validation.

The Mediatrix Arcfinder can be divided into four steps: object segmentation, preselection, measurement, and final classification. In the segmentation phase, sets of pixels above the background are grouped into objects (as discussed in Sec. 4.2.1). In the preselection phase, we define a sample of objects to be analyzed, performing cuts to eliminate those that can be readily discarded as not being arcs (Sec. 4.2.2). The measurements are carried out through the Mediatrix filamentation method introduced in section 3 (see Sec. 4.2.3). For the final classification, we use an ANN trained to identify arc candidates (see Sec. 4.2.4).

4.2.1 Object segmentation

The first step is to identify the objects in the image, separating them from the background and defining which set of pixels belong to a given object. To this end, we use

the SExtractor (Bertin & Arnouts, 1996) software, which has several parameters controlling the object identification, deblending, and measurement process, including the minimum signal-to-noise ratio for a given pixel to be considered, a minimum number of pixels, and deblending thresholds. Tuning these parameters is a critical step in arc identification, especially as arcs are low surface brightness objects, are often close to brighter sources, and can thus be easily missed and/or blended with other sources. However, in this contribution, we do not perform a systematic optimization of these parameters. We rather use a set of manually tuned values that provided good results on a visual inspection, as our primary focus is in the measurement and final classification phases. Horesh et al. (2005), Estrada et al. (2007), and Kubo & Dell'Antonio (2008) also use SExtractor in the object segmentation phase of their arc finding methods.

SExtractor provides an output catalog containing measurements on the objects identified and several image outputs. Here we use two such output images, namely OBJECTS, containing the pixel values of all objects identified, and SEGMENTATION, in which all pixels belonging to the same object have the same value (corresponding to the object ID in the catalog). From these two images, we produce a single array per object, which contains only the pixels belonging to that object and the respective pixel value. These arrays are called *postage stamps* and are kept in the memory for the next steps. From this point on the AMA algorithm will work separately on each object.

4.2.2 Preselection

Among the measurements provided by SExtractor are the object semimajor axis A and semiminor axis B derived from the weighted central second moments of the pixels (Bertin & Arnouts, 1996). From them we define the ellipticity e as

$$e = 1 - \frac{B}{A}, \tag{4.1}$$

which is used to eliminate from the sample objects with ellipticities below some threshold $e_{\rm th}$. For the images used in this chapter, we set $e_{\rm th} = 0.4$. We also add a cut on the maximum number of pixels to exclude objects that are too large and are definitely nonarcs. To avoid

spurious detections we remove objects that are close to the image borders. We do not make cuts in the object signal-to-noise ratio or magnitude, as this could remove some of the faint arcs. We do not apply any star-galaxy separation either, as the cut on e already removes the stars.

4.2.3 Measurements with the Mediatrix filamentation method

In chapter 3 we presented and discussed the Mediatrix Method basics applied essentially to arcs shapes, for the AMA algorithm we apply the method to all (preselected) objects in an image for the sake of classification as arc candidates. For an iteration level k the object length L_k and width W_k are given by Eq. (3.3) and (3.4) respectively. We use an adaptive method to decide when to stop the mediatrix iteration. When the distance between two neighboring segments l_i (see 3.3) is too small, there is no point in continuing the Mediatrix iteration. On the contrary, the decomposition starts to be dominated by noise (or by the finite pixel size). We expect that when $l_i \lesssim W_k$ the directional information is lost and no further division is useful. Therefore we impose the following condition as a criterium to stop the iteration:

$$l_i \leq \alpha W_k, \tag{4.2}$$

where α is a parameter that is set to $\alpha = 1$ in this work. The decision to continue with the Mediatrix filamentation is taken independently for each segment following Eq. (4.2). The iteration generally stops for regular objects at the same level for all segments, such that the total number of segments (and oriented vectors) is $N = 2^n$, where n is the last iteration level. However, if the shape is irregular, the iteration can be carried out to different levels for different regions of the object. Also, if the object is composed of noncontiguous sets of pixels, the code may not find any pixel along the perpendicular bisector of two given Mediatrix points. In this case, the iteration is stopped so that no further division happens between those two points. After the last iteration, the sum in Eq. (3.3) is carried out for all segments defining the final length L. The final width W is defined using Eq. (3.4).

As discussed in the previous chapter we may define a center of curvature by determining the circle that passes through the points E_1, M_1^1, and E_2. We denote the center of this circle

by $\vec{r}_c$ and its radius by R_c. Using these points, we may also define a length as the circle arc length, L_c, between the two extreme points, E_1 and E_2. Another possibility is to define a curvature center based on all points from the Mediatrix filamentation using Eq. (3.5) and (3.6) to derive the curvature center $\vec{r}_0$ and the confidence region respectively. We expect that curved arcs have a small CR as compared to the arc size. We noticed by visual inspection of the CR and the objects, that for arcs the CR is usually elongated along the radial direction and does not, in general, intersect the arc.

We provide, as inputs to the ANN, combinations of the parameters described above derived from the Mediatrix filamentation. These combinations are defined so as to be scale invariant, such that they depend mostly on the object shape and are weakly sensitive to the pixel scale. In some cases, we normalize the output by the appropriate power of L to produce the scale invariant quantities. In particular, we tested the ANN with the following set of parameters:

i) The length-to-width ratio L/W.

ii) The mean of the scalar products of each unitary vector $\vec{n}_i/|\vec{n}_i|$ with its neighbor, $\vec{n}_{i+1}/|\vec{n_{i+1}}|$, i.e.,

$$s := \frac{1}{N}\sum_{i=1}^{N-1} \frac{\vec{n}_i}{|\vec{n}_i|} \cdot \frac{\vec{n}_{i+1}}{|\vec{n}_{i+1}|}. \tag{4.3}$$

This quantity provides a measurement of the coherence of the shape. For very irregular objects, its value is low, while for long and smooth objects (curved or not), its value should be close to 1.

iii) The minimum value of the function $M(\vec{r})$ divided by the arc length squared (for dimensional reasons), M_0/L^2.

iv) The arc aperture $\Delta\theta := L/R$, where the radius R is the distance from $\vec{r}_0$ to M_1^1.

v) The ratio between the arc aperture defined above and the one constructed from the circle that contains points E_1, M_1^1, and E_2, $\Delta\theta/\Delta\theta_c := (L/R)\,/\,(L_c/R_c)$.

vi) The distance between the center of the circle $\vec{r}_c$ and the minimum of $M(\vec{r})$ normalized by the arc length, $\delta r := |\vec{r}_0 - \vec{r}_c|/L$.

vii) The ratio between the major axis of the CR, L_{CR}, and the arc length: L_{CR}/L.

viii) The eccentricity of the CR, $e_{\rm CR}$.

ix) The ratio between the number of pixels from the arc enclosed by the CR, A_{CR}, and total number of pixels in the object, A, i.e., A_{CR}/A.

The choice of parameters above is somewhat arbitrary, but is inspired by the visual assessment of these quantities on samples of arcs and objects that are clearly nonarcs. An important component of this chapter is to obtain a set that is at the same time good for discriminating arcs from nonarcs and is less time- consuming.

4.2.4 Arc identification with an artificial neural network

The arc identification process through the ANN can be subdivided into two parts: the training process and the actual classification. In the current implementation, we use a standard back-propagation and fully connected ANN (Rumelhart et al, 1988; Williams & Hinton, 1986). The ANN has the following structure: *a)* an input layer with i neurons, where i is the number of inputs used in the specific ANN configuration, which in this case is a subset of the parameters described in section 4.2.3; *b)* a second layer with j hidden neurons; and *c)* the output layer with one neuron. The ANN activation function is linear and the output is a floating point number R in the range -1 to 1. The AMA code was developed using the python binding for the Fast Artificial Neural Network (FANN) library[1].

In order to recognize the arc shape using this type of ANN, it is necessary to train this neural network on a group of objects, which were previously classified as arcs and nonarcs. A successful training process is determinant to reach acceptable results in any back-propagation ANN code. The training requires presenting to the ANN two groups: the arcs group (AG), with desired output $+1$ and the nonarc group (NAG), with desired output -1. The two groups also need to have the same order of number of objects. Otherwise, the ANN may just output as the result a number that represents the larger group. The AG and NAG are split into a training group and a validation group. In this work, we used 80% from all objects chosen randomly from the sample of AG and NAG for training and 20% for validation.

After the training, the ANN is applied to the validation group, yielding an output value R for each object. We have thus to set a threshold t on this output such that the code finally classifies each object (i.e., each set of input measurements on the object) as an arc or not.

[1]For further information see `http://leenissen.dk/fann/wp/`

After running in the validation group the code computes the completeness, c, defined as the fraction of arcs recovered (i.e., *the ratio of the number of detected arcs and the total number of arcs* in the validation group) and the fraction of false positives, f, defined as the fraction of nonarcs that are classified as arcs (i.e., the ratio of the number of nonarcs detected as arcs and the total number of nonarcs in the validation group).

After the validation test, the training and validation groups are redefined randomly and the whole process is repeated m times. In this work we retrained the ANN for a single set of input parameters 40 times. The validation code outputs the mean completeness $\bar{c}$, mean false positive fraction $\bar{f}$, and their standard deviation for the $m = 40$ validation groups.

4.3 Training and validation of the ANN

In this work, we use the training and validation steps to characterize the behavior of the AMA with respect to all aspects of the ANN identification process mentioned in Sec. 4.2.4 above, including the types of images used in the training, sets of inputs, number of hidden neurons, and threshold for classification. The goal is to define a good set of configurations for practical applications of the AMA. In particular, we seek to have a high completeness c at the same time limiting the fraction of false positives f. This search for the best parameters for the ANN detection is described in Sec. 4.3.3

The arcfinder method was trained using a sample of 175 simulated arcs (AG) described in Sec. 4.3.2 and 437 nonarcs (NAG) taken from HST images, as described in Sec. 4.4. These numbers are the result of steps 1 (object identification) and 2 (preselection), and thus all objects from the two samples already pass the preselection criteria described in Sec. 4.2.1. Notably, all have ellipticities above $e_{\rm th} = 0.4$. Therefore, in all comparisons and tests described in this chapter, we are really testing the measurements + ANN steps of the whole arc finding process, which is the aim of this contribution.

4.3.1 ANN inputs from the Mediatrix filamentation

We performed the training with ten different subsets of the parameters i to ix described in Sec. 4.2.3 to determine the best combination of Mediatrix parameters to be used as input

for the ANN. Each subset is labeled with a letter from A to J. The input configurations are presented in Table 4.2. We divided the input parameter sets into two groups depending on whether the CR evaluation is necessary or not for a given configuration. Group 1 includes only measurements derived directly from the Mediatrix filamentation process (*i* and *ii*) and from the minimization of $M(\vec{r})$ (*iii* to *vi*), while group 2 contains measurements that depend on the CR (parameters *vii* to *ix*). The total time to run the AMA varies only slightly within each group, but changes considerably between the two groups, as the process to obtain the CR is currently the most time consuming step of the AMA.

From sets A to J, the number of inputs (i.e., the number of parameters in the input vectors) is systematically decreased (except for I and J, which have only one input each). The three sets of configurations in Group 2 (A, B, C) include the determination of the CR and are thus those that take more computational time. From configuration D downward the time drops substantially. In all cases but one (J), we keep the parameter (*i*), i.e., L/W, which is historically the primer arc indicator. In section. 4.3.3 we test the AMA for each set and compare the results for c and f to define the best set for practical applications, both in terms of maximizing completeness and minimizing contamination, also accounting for the computational time.

Table 4.2: *Combinations of inputs used for the neural network training (A to J).*

	Group 2			Group 1					
	L_{CR}/L	$e_{\rm CR}$	A_{CR}/A	L/W	s	M_0/L^2	$\Delta\theta$	$\Delta\theta/\Delta\theta_c$	δr
A	X	X	X	X	X	X	X	X	X
B		X	X	X	X	X	X	X	X
C			X	X	X	X	X	X	X
D				X	X	X	X	X	X
E				X		X	X	X	X
F				X			X	X	X
G				X				X	X
H				X					X
I				X					
J									X

4.3.2 The training set sample: simulations with AddArcs

Given the intrinsic variation in gravitational arc shapes it is important to have a large enough training sample so as to encompass some of their diversity and, at the same time,

have sufficient statistics to train the ANN. However, the current samples of arcs taken under uniform observing conditions are still substantially small. Also, we need a truth table of arcs in the AG and not all known arcs have spectroscopic confirmation. Moreover, we want to be able to control some observational and instrumental parameters, such as the background and noise, point spread function, and pixel size so as to test the arc finder under different conditions. For this sake, we use simulated gravitational arcs for the training and validation phases.

The simulated sample was created using the `AddArcs` pipeline (Brandt et al., in preparation), which uses two input catalogs: one with the properties of the lenses (such as mass, ellipticity, and redshift) and one with the properties of the sources (such as magnitude, size, ellipticity, and redshift), plus a number of configurations that can be set, such as observational and instrumental parameters. The code distributes the sources in random positions for each lens in the catalog, following the specified surface number density, and then it randomly chooses the source parameters from the source catalog. Given the input models for the source and the lens, from their respective catalogs, the pipeline uses the `gravlens` code (Keeton, 2001) recursively to perform the projection of the sources onto the image plane. It then identifies which images correspond to arcs and generates postage stamps from them, providing as one of its outputs a pixelized surface brightness distribution of these objects, i.e., a simulated image of a gravitational arc.

For our simulated arc sample the input catalog contains galaxy cluster scale halos from N-body simulations[2] and we assume a Navarro–Frenk–White density profile (NFW; Navarro et al. , 1996, 1997), with elliptical surface mass density (see, e.g., Caminha et al, 2013), a given mass–concentration parameter relation (Gao et al, 2008; Neto et al, 2007), and fixed ellipticity. The sources are given by a Sérsic surface brightness distribution (Sersic, 1968) with parameters derived from the Hubble Ultra Deep Field Survey (UDF; Beckwith et al, 2006; Coe et al, 2006).

To define a even purer sample of arcs objects we make a visual inspection in the Strong Lensing simulations by `AddArcs` and removed objects that even with high L/W do not

[2]We use a catalog from the *Las Damas/Carmen* N-body simulation, `http://lss.phy.vanderbilt.edu/lasdamas/`.

have a definite curvature or were too small and pixelated to present a reliable arc shape.

In Sec. 4.4 we apply the trained AMA to real images of systems containing arcs taken with the WFPC2 instrument on HST (Smith et al, 2005). As in our training the AG is given by the simulated arc sample, we set the observational conditions in the simulations to mimic these HST images. In particular, we use the same pixel scale as WFPC2 and convert the counts in each pixel on the simulated images to data numbers using the properties of these HST images (for details, see Appendix A of Bom et al, 2016b). At this point the simulated arcs are smooth, i.e., the pixels have no fluctuations from noise and the simulated images have no background. We refer to this calibrated set of arcs as pure arcs.

However, real astronomical images have noise (including Poisson noise from the counts in pixels) and background. Even though it is common to work on background-subtracted images, of course the background noise remains. Therefore, for a proper test of the arc finding process we need to include at least these two effects on the simulated images, as they are of fundamental importance for object detection and measurement[3]. The (constant) background is added to all pixels as measured from the HST images. Then each pixel is assigned a new value sampled from a Poisson distribution with the mean given by that pixel value in count units (including object plus background). Finally, the new image with background and noise is converted again to the data units.

Both samples of simulated arcs go through the object identification and preselection phases, as described in section 4.2.1. In particular, `SExtractor` is run on each simulated image containing one arc and a postage stamp is created for that object. The Mediatrix method is then applied and the derived parameters are input to the ANN.

The validation of the trained ANN is performed using the background and noise sample as it is the more realistic sample. Nevertheless, it is interesting to test the results of the training carried out using each type of image as entries. These tests are discussed in the next section.

[3]The PSF convolution is not important for this example application in HST images and is not included in this work.

4.3.3 The training and validation results: Determining reasonable ANN configurations

In this section, we present the training and validation results and use them to select an optimal set of configurations for the ANN arc finding process. We start by looking at the dependence of f and c as a function of the number of hidden neurons (N_h). We considered all configurations from A to J described in Table 4.2 and varied the number of neurons from 2 to 15 fixing the threshold for the ANN output to $t = 0$ (i.e., objects with the ANN response function $R > 0$ are defined as arcs). First, we considered the training carried out on the pure arcs set and then in the background and noise images as the AG (the NAG is the same in both cases). In the first case, we do not notice any significant variation of the completeness and false positives with N_h for any input configuration. On the other hand, when the training is performed using the images with background and noise, we do see a dependence on the hidden neurons for some of the configurations. This is shown in Fig. 4.2 for only three configurations: A (representative of group 2), D (representative of group 1 with several inputs), and J (with one input). We see that the dependence of the completeness on N_h is only significant for the A configuration, for which we can observe a significant increase in c up to $N_h \sim 6$. In all configurations that we have investigated, there is no gain in increasing N_h above this value. Thus, only for the configuration with the highest number of inputs and using the training set with more variation among the systems (due to the noise in the AG) does the ANN require more complexity than two hidden neurons. On the other hand, the false positive fraction does increase with N_h in most cases. This is less visible in configuration A because of the large variance and could be due to overtraining, when the number of neurons is large.

As we see below, we end up choosing the pure arcs as a training sample and therefore we could be tempted to choose a very small number for N_h, as this also significantly decreases the computational time. On the other hand, to be on the safe side for real-world applications, we still want to have a larger number of neurons for dealing with the diversity of real arcs. Therefore, we set our final number of hidden neurons to $N_h = 4$ in all tests to reach a balance between computational time, false positives, and completeness.

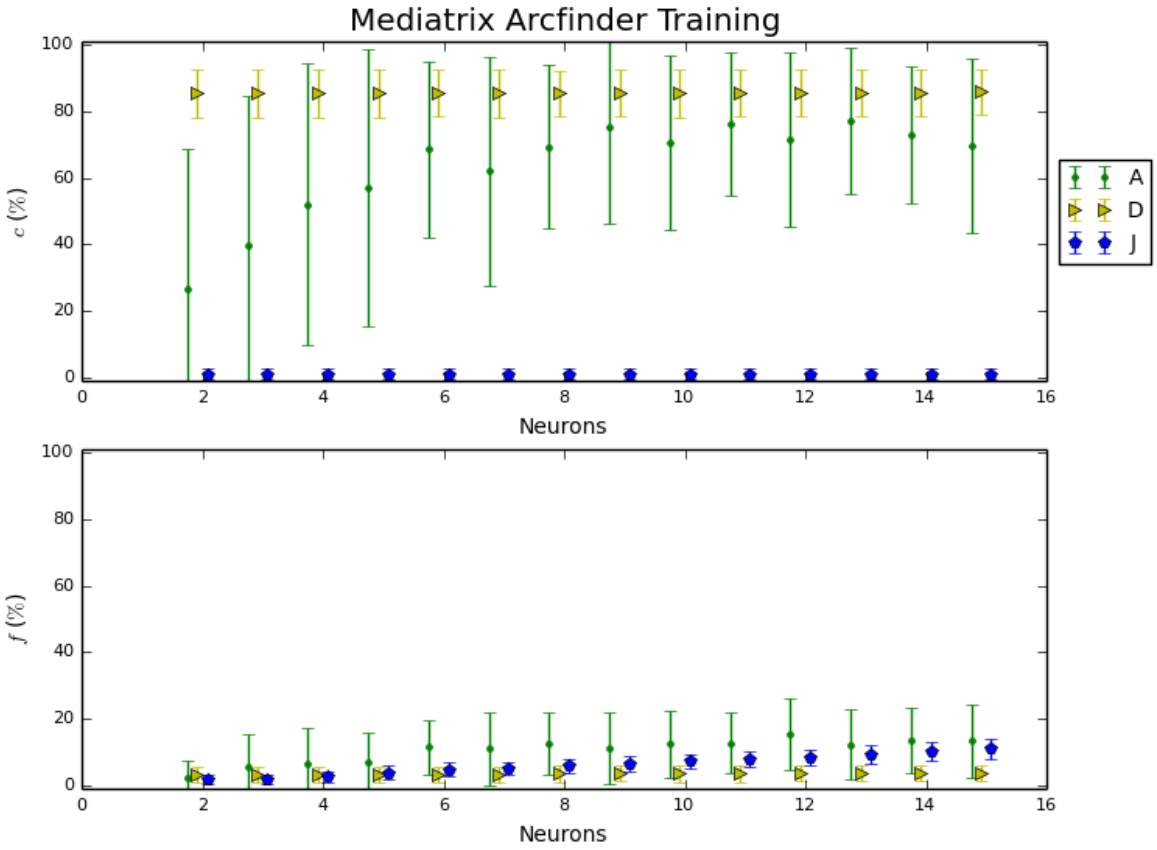

Figure 4.2: *Mean completeness $\bar{c}$ and fraction of false positives $\bar{f}$ as a function of hidden neurons, using background and noise arcs in the AG for training and a threshold $t = 0$. The error bars are the standard deviation from the 40 training plus validation subsamples. We shifted the symbols horizontally for clarity.*

Now we turn to the choice of the final set of configurations and the types of images for the training. In Fig. 4.3 we show the results for c and f for the ten configurations in Table 4.2 using pure arcs (in large blue circles) and those with background and noise (in small green dots) for the training. Clearly, configurations A to D have the best performance, both for completeness and for false detections. The results from training on pure arcs in general have a smaller variance than using background and noise, in particular for configurations A and B. Besides, for lower thresholds, A and B have much more contamination when trained on arcs with background and noise than with pure arcs.

At first sight, it could seem surprising that training with the more realistic set of arcs in general gives worse results. For the ANN, it is better to learn with a more consistent and well-defined set of parameters from the arcs, than having a larger variation on these

parameters owing to noise, even if the validation is carried out on the images that do have noise and background. It is important to mention that the noise is added only once to the arc sample, i.e., the variance among the 40 subsamples is not due to different realizations of the noise, but rather to the spread in the parameters caused by the noise in each subsample of arcs. From now on, we choose to carry out the training process using only the pure arc sample.

As for the inputs, we see from Fig. 4.3 that the combination that gives the highest mean completeness, and a low fraction of false detections is configuration A, from group 2. However, D also gives a good performance (as good as the other configurations in group 2) but is in group 1, i.e., is computationally faster, as it does not require the computation of the CR. Therefore, we keep these two sets of inputs, A (the best) and D (almost as good as A, for both c and f, but faster), for the next test and for applications to real data.

Finally, we look at the dependence of c and f on the threshold t for these two selected configurations. We vary t in steps of 0.25. The cases $t = -1$ and $t = +1$ are trivial as all objects are classified as arcs and nonarcs, respectively. In Fig. 4.4 we show the results for t in the range $[-0.75, 0.75]$. As expected, both the completeness and the false detections decrease as t is increased. However, c has a softer dependence with t than f. Two possible choices for t are in order. If we want to have a higher completeness, even at the expense of a higher percentage of false detections, then $t = -0.75$ is a good choice. This threshold would be preferred, for example, in targeted surveys, where a visual inspection to discard false positives is feasible even if the false detections outnumber the real arcs. In this case, we obtain $c \sim 95\%$ and 90% and $f \sim 10\%$ and 25% for configurations A and D, respectively. On the other hand, if we seek a purer sample of arcs, a good choice is $t = +0.25$. After this value c drops considerably, while f does not vary much. This choice could typically be adopted for a wide-field survey, where we need to minimize the fraction of the objects to be inspected for a final selection. In this case, c decreases a bit to $\sim 90\%$ and 80%, but f drops substantially to $\sim 3\%$ and 2%, respectively, for A and D.

We recall that f is defined as the fraction of false positives concerning the total number of nonarcs, i.e., it is essentially the number of false detections over the total number of objects that pass the preselection cuts. In the training and validation process the numbers of arcs

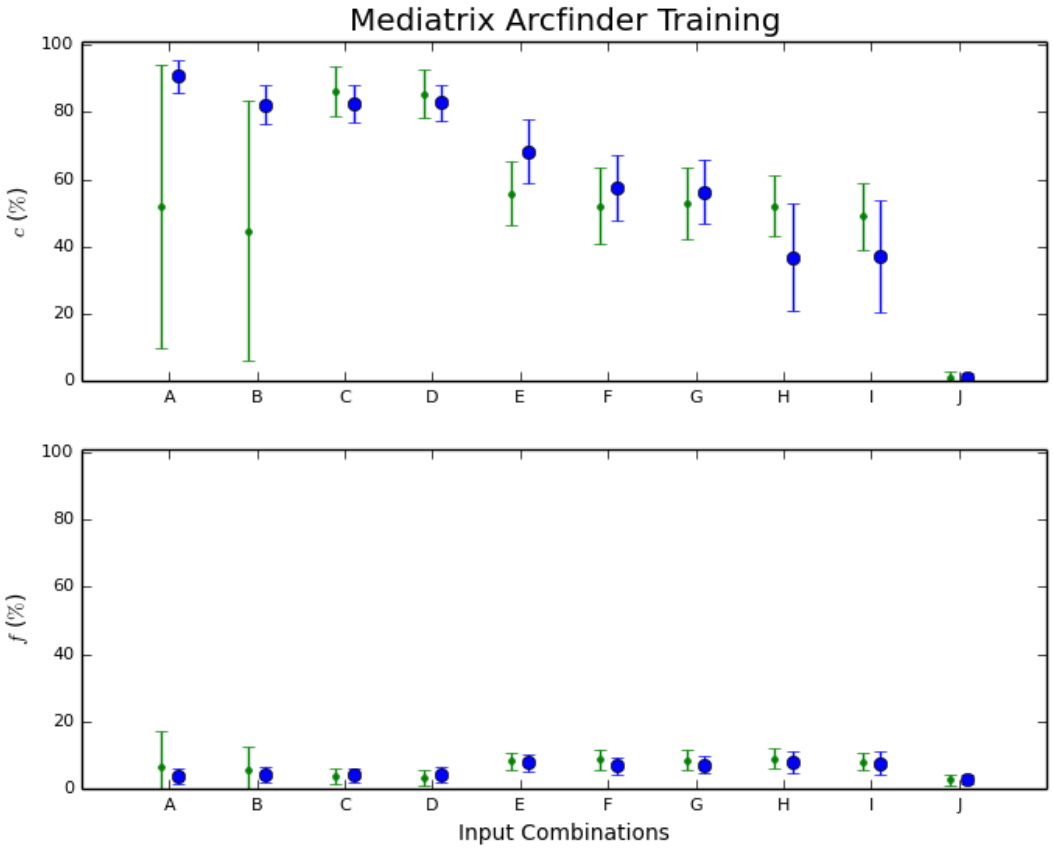

Figure 4.3: *Mean completeness $\bar{c}$ and false positive fraction $\bar{f}$ for the different sets of inputs (for threshold $t = 0$). The results from the training in pure arcs are shown as large blue dots, while those using images with background and noise are shown as small green dots. The error bars are the standard deviation from the sets of training plus validation subsamples. We shifted the symbols horizontally for the two types of input images for clarity.*

and nonarcs are of the same order of magnitude. However, for wide-field surveys, the number of arcs is roughly five orders of magnitude less than the total number of objects detected. Therefore, even if the preselection phase filters out 90% of the objects and f is as low as 1%, the false detections would still outnumber the real arcs by large amounts. Thus, even a low contamination as currently achieved with $t = +0.25$ would still require a further step of visual inspection when applied to large surveys, as happens with most arc finders proposed so far.

It is worth pointing out that t can always be set a posteriori in the sense that the ANN is specified without the need to define a threshold. Once the inputs and hidden neurons are defined and the training is carried out on a given sample, the ANN is fully determined. When the ANN is applied to the data, the result is an output value of the response function for

each object. Therefore we can vary the value of t after the ANN is run and choose a suitable balance between c and f to set the threshold.

We see from Fig. 4.4 that the completeness for configurations A and D are compatible with each other within their standard deviations for the whole range of t (except for $t = 0.75$), showing that both configurations are comparable for arc detection (although $\bar{c}$ is systematically higher for A). Regarding the false detection fraction, it is clearly higher for configuration D and $t < 0$. The highest difference with A occurs for $t = -0.75$ and is smaller than two standard deviations. It is not clear whether this is a real difference between the two configurations or if it is just a fluctuation.

In the next section, we apply the two ANN (i.e., with configurations A and D) trained as described in this section to objects from real HST images.

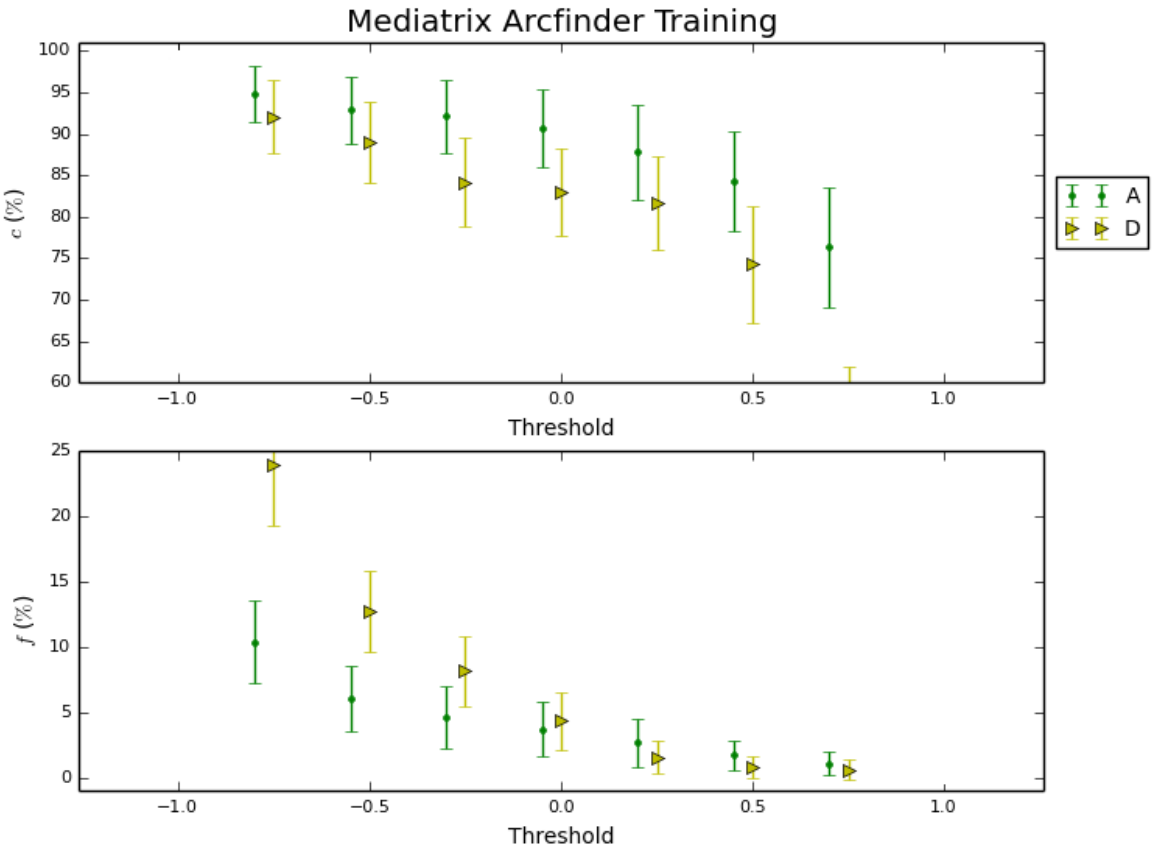

Figure 4.4: *Mean completeness $\bar{c}$ and mean false detection fraction $\bar{f}$ for the input configurations A and D as a function of threshold. The results are obtained from the training on pure arcs with an ANN with four hidden neurons. Symbols are shifted in the horizontal direction for clarity.*

4.4 Application on HST cluster images

In this section, we show an example of an application of the AMA to real images taken with the HST. In particular, we consider a well-known sample of massive clusters observed with the Wide Field and Planetary Camera 2 (WFPC2) instrument on HST from Smith et al. (2005). Images from this camera have been used in other exploratory studies of arc finders (Horesh et al, 2005; Lenzen et al, 2004; Seidel & Bartelmann, 2007), and, in particular, the same Smith et al. (2005) sample was used in Horesh et al. (2005).

The WFPC2 instrument has a mosaic of three wide-field (WF) CCDs (forming an L pattern) and a smaller CCD with finer pixel scale close to the center of the field. The exposures of each cluster are centered on one of the WF CCDs. Several exposures are taken with a dither pattern, so as to combine all CCDs into a single image with no gaps. The HST server[4] provides both the combined image with all CCDs and a combined image of all exposures for each single CCD. For the purposes of this paper it is better to work on the single images per CCD, as the mosaic images have strong S/N variations and artifacts in the regions between CCDs and close to the edges. This can produce spurious detections and affect the background estimation and it is beyond the scope of this paper to deal with them. For each CCD image, we remove the regions near the image borders to avoid the spurious detections.

We use the images from Smith et al. (2005) to apply the AMA to find arcs in the images, but also to provide the sample of nonarcs for the training of the ANN. This is so that the NAG have exactly the same observational and instrumental conditions as the images in which we look for arcs. We mimic those same conditions in one of the simulated arc samples as discussed in[5] Sec.4.3.2. In particular, we consider CCDs that do not contain the cluster center and have no apparent arcs to provide the NAG. We use seven such CCDs, carry out the detection and preselection steps and end up with the sample of 437 nonarcs used in the training of the ANN discussed in the previous section.

We apply the AMA to four clusters in the Smith et al. (2005) sample that have giant and

[4]The HST data products can be downloaded from the European HST Archive at ESA/ESAC: `http://archives.esac.esa.int/ehst/`

[5] For details on the noise and background evaluation in the HST images see Bom et al. (2016b).

clearly visible arcs, namely Abell 68, Abell 383, Abell 773, and Abell 963. The images of the CCD with more arcs for each cluster were visually inspected and the arc candidates were classified in three categories: A for the best candidates, objects with curved shapes close to the cluster central regions or galaxy cluster members; B for intermediate candidates, which are curved but do not have a cluster center or galaxy as a center of curvature or that are close to the cluster center but are not curved; and C for more ambiguous candidates that do not fall in the previous categories. This classification is somewhat arbitrary but is useful for a first assessment of the ability of the ANN to recover the arcs as a function of their quality/likelihood. For each cluster we label the arcs in each category with a number (e.g. a4, b2, and c1). In Figs. 4.5 and 4.6 we show cutouts of the images encompassing the regions of each selected CCD where arcs were visually selected and marked. In cluster A68 we marked 9, 2, and 1 arcs in the A, B, and C categories, respectively. For A383 we labeled 7, 4, and 2 arcs in these categories, while for A773 the numbers are 1, 1, 1, and for A963 7, 3, 1. This gives a total of 39 arc candidates, 24, 10, and 5 respectively in the A, B, and C, categories. We use these identifications as a truth table for testing the AMA.

The aim here is only to have a set of objects with a morphology visually associated with gravitational arcs. It is hard to compare the numbers above with the other identifications for the same clusters in the literature. On one hand, we only consider the arcs from a single CCD, do not include radial arcs, and do not impose an L/W cut for arc selection. On the other hand the visual identification is rather ambiguous anyway. In any case the orders of magnitude are compatible with the visual searches in Sand et al. (2005), which identified 27 arc systems in these four clusters and Smith et al. (2005), which found 33 multiple images in the four CCD chips we consider in this work.

Now we apply the AMA algorithm, to the four selected clusters. First we run `SExtractor` (step 1), with the same configurations used in the training and validation phases, obtaining a total of 1378 detections. Applying the ellipticity and other cuts on the preselection (step 2) leaves us with 304 objects, on which we run the Mediatrix filamentation (step 3), providing the inputs for the ANN. It must be pointed out that not all arcs visually identified comprising our truth table are found to be objects in the `SExtractor` run (likely because of their low surface brightness). Moreover, many of the arcs found end up blended with other objects in

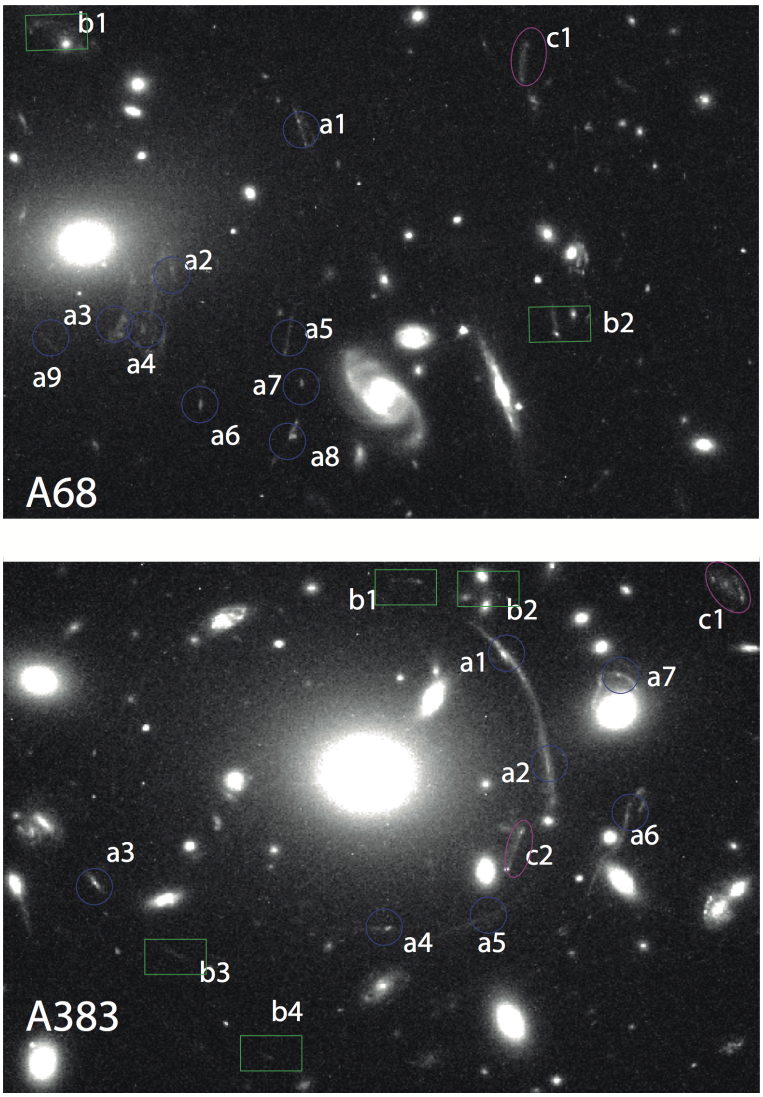

Figure 4.5: *Arc candidates in Abell 68 and Abell 383. The candidates were classified in* 3 *categories: A, best candidates indicated with blue circles; B, intermediate candidates indicated with green rectangles; and C, ambiguous candidates indicated with magenta ellipses.*

the image and therefore the morphology of the generated postage stamp does not represent an arc anymore. The total number of arcs that are either not detected or blended is 15. For a fair comparison with the results of Sec. 4.3.3 these objects should not be considered in the denominator for computing the completeness c, as we do not expect the ANN to identify them as objects; the ANN was not trained on blended objects and obviously the arcs that are not detected cannot be classified by the ANN.

Finally, we apply the ANN, trained as described in Sec. 4.3.3, using either the sets of inputs A or D, which are selected from our exploratory runs on the simulated arcs (using four hidden neurons and trained using the pure arcs as AG). The resulting number of arcs

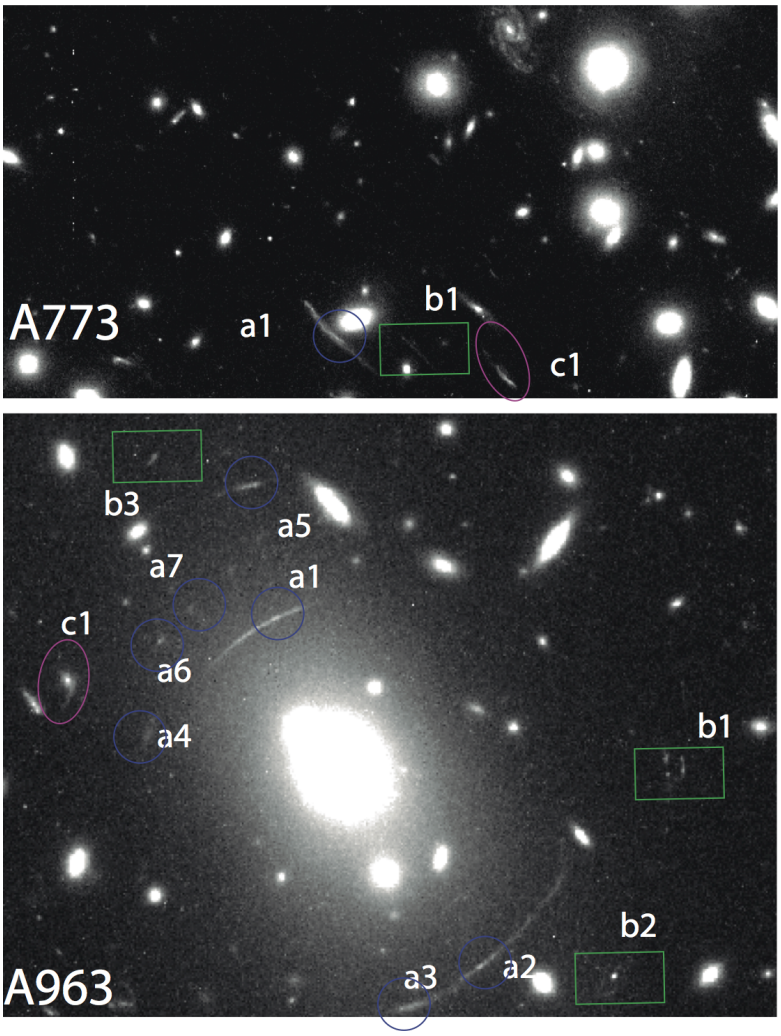

Figure 4.6: *Arc candidates in Abell773 and Abell963. The arc candidates in the* 3 *categories are indicated following the same convention as in Fig. 4.5.*

detected is, of course, a function of the threshold t. In Table 4.3, as an example, we show the results using configuration D and $t = -0.75$. In that case, a total of 16 arcs were identified and there were 43 false detections. We also show the number of arcs visually identified in each category along with the arcs that were not detected by `SExtractor` and those that were blended with other objects. We note that in A68 four out of six detectable arcs were found, while for A383 six out of seven were identified by the ANN, in A773 one out of two and in A963 five out of eight. The overall c in this case is $16/24 \simeq 67\%$. Considering each subclass, we have a completeness of 71%, 67%, and 50% for the A, B and C categories respectively. Although these numbers show the expected trend with arc quality, they are all mutually consistent taking Poisson statistics into account, and we cannot conclude whether the arc finder performs better or not with arc quality. Therefore, in the remaining of this

chapter we consider all categories together for evaluating c.

Table 4.3: *Arc detections in the 4 selected HST clusters. Columns 2 to 6: number of arc candidates visually identified in each category (A, B, and C), objects that are not detected by* `SExtractor`*, and arcs that are blended with other objects. Column 7 shows the arcs detected by the ANN for configuration D and $t = -0.75$. The last column shows the number of false positives (i.e., objects classified as arcs but not on the arc truth table) for the same configurations.*

	Category			SExtractor		ANN	
Cluster	A	B	C	Not detected	Blended	Arc detections	N_f
Abell 68	9	2	1	a9	a2, a3, a4, b1	a6, a7, a8, b2	12
Abell 383	7	4	2	a5, b1, b4	a7, b2, c2	a1, a2, a5, a6, b4, c1	3
Abell 773	1	1	1	—	a1	c1	13
Abell 963	7	3	1	—	a1, a3, a6	a2, a5, a7, b2, b3	15

As a comparison, we point out that the arc finder run presented in Horesh et al. (2005) found 16 arcs in the four clusters under consideration. Restricting to the areas where we denoted arcs for our truth table (see Figs. 4.5 and 4.6) these authors found a total of 9 arcs, 5 of which are in common with the sample of 16 arcs detected with the AMA, and 3 are blended in our detections. On the other hand, only objects with $L/W > 7$ are selected by Horesh et al. (2005), while we make no cuts in this quantity. In any case, the focus in Horesh et al. (2005) is not on completeness, but on a comparison between a real and a simulated arc sample. A more detailed comparison of the AMA with this and other arc finders is outside the scope of this thesis (see Bom et al, 2015, for preliminary results).

As for the false detection fraction f, it is computed as the ratio of the false positives to the total number of nonarcs given as input to the ANN. For the configuration in Table 4.3 we have $f \sim 15\%$. With respect to the total number of objects detected, the fraction of false detections is 3%.

The false positives are objects classified as arcs, but that are not on the truth table. In principle, some of these objects could be real arcs that are missed by visual inspection. However, we did look at all false positives and only two of them could be associated with arcs; they were in fact pieces of arcs with multiple peaks, other pieces of which have been identified by the arc finder. Thus these cases are negligible for the purposes of this thesis.

In Fig. 4.7 we show c and f as a function of the threshold t for configurations A and D combining the arc detections for the four cluster images considered in this section. Poisson error bars are indicated. We see that the ANN achieves a reasonable completeness, $\sim 70\%$ for configuration D, and $\sim 50\%$ for A, for a low threshold ($t = -0.75$), while still keeping a low contamination rate, $\sim 15\%$ and $\sim 9\%$ for configurations D and A, respectively.

As in the simulations, configurations A and D yield values of c that are compatible with each other in the whole range of t, taking their Poisson errors into account. However, c differs considerably between the real and simulated data. The completeness is significantly lower on the data and decreases more abruptly with the threshold than what was seen in the simulations. We interpret this result as an indication that the simulations are not realistic enough for a proper quantitative comparison with the real data. In fact, the simulated arcs are very diverse, but do not include some relevant degrees of realism, such as surface brightness variations in the sources and lenses with substructure. In addition, the real arcs are often close to bright galaxy cluster members, which can affect their segmentation and deblending (both due to contamination from the galaxies and background misestimation on the crowded field) and thus affect their shape. The strong effect of blending with other objects is already accounted for in our comparisons in the sense that these objects are removed from the denominator of c. However, a less significant contamination from close-by objects or a breaking into smaller objects affects the Mediatrix measurements and therefore the arc detection with the ANN, which was trained in simulations that do not include these effects.

In the validation c is a bit higher for A than D in the whole range of t. On the other hand, in the real data there is an apparent trend for D to have a higher completeness than configuration A for the smallest threshold. For the remaining interval the performance is very similar among configurations A and D.

Regarding f, the results are also compatible between A and D within the error bars, and the difference is again higher for $t = -0.75$. The false positive fraction drops substantially for higher t, reaching $f \lesssim 5\%$ for $t > -0.25$.

Comparing the false positive fraction obtained during the validation process with those from the runs on the HST images (bottom pannels of Figs. 4.4 and 4.7), we see that the

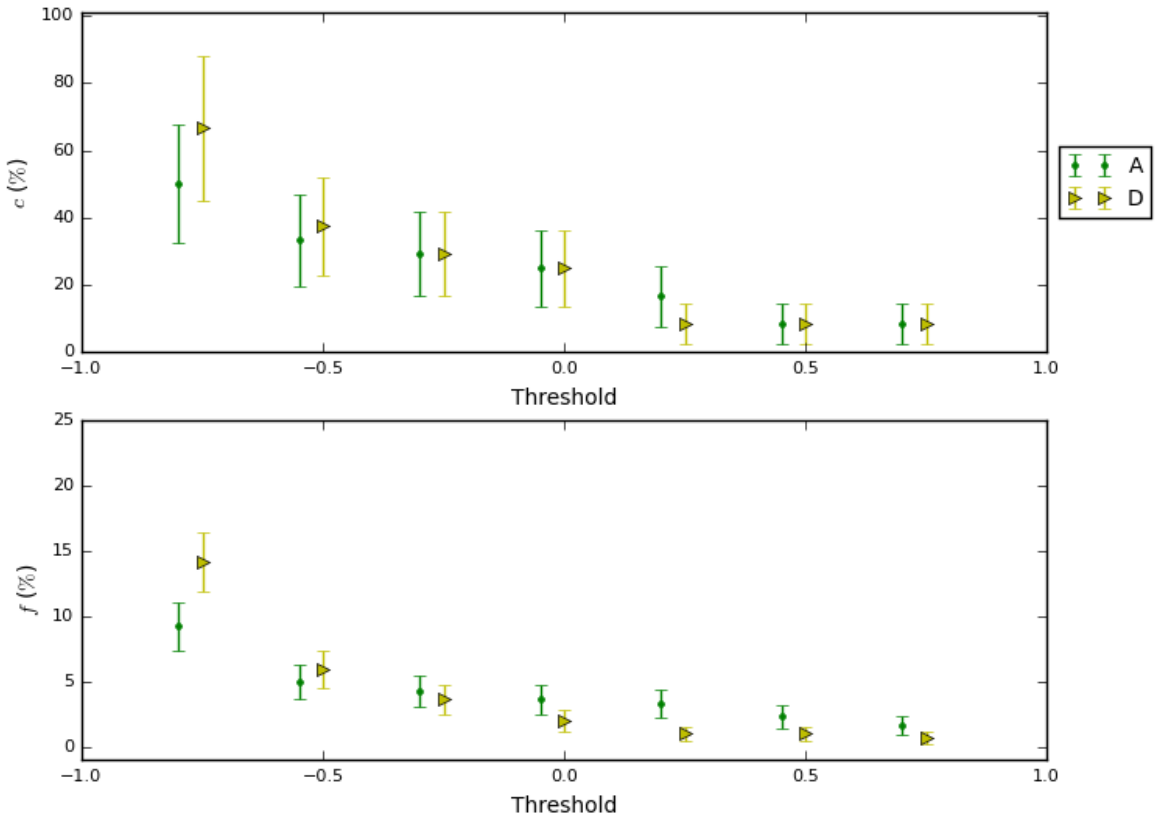

Figure 4.7: *Completeness c and fraction of false detections f, including Poisson error bars, for the arcs in the 4 selected HST Abell clusters, for configurations A and D, as a function of threshold. Data points for configuration A are shifted horizontally for clarity.*

results are consistent for configuration A in the whole range of t. However, for configuration D and $t < 0$ the false detection fraction is clearly higher in the validation than in the real data. The highest discrepancy occurs for $t = -0.75$, but is smaller than twice the standard deviation within the training plus validation samples. This difference could be just a consequence of the difference in f between A and D pointed out in the previous section or may be a difference in the behavior of f in the real data with respect to the validation.

The agreement between the validation set and the real data for f is expected; the NAG is obtained from the same set of images from WFPC2 for the training plus validation, although the CCDs are different and include other clusters. Thus we would expect a similar behavior between the bottom panels of Figs. 4.4 and 4.7 for f. This is indeed the case for configuration A and strengthens the case for a fluctuation in the false positives obtained in the simulations for configuration D.

4.5 Convolutional Neural Networks for Strong Lensing detection

The AMA algorithm presented in the previous sections was conceived particularly to objects with curvature, i.e. gravitational arcs but it turns out that the current implementation is not well suited for galaxy scale lensing, due to the blending of the arc and the lensing galaxy light, for instance we may have Einstein Radius $\theta_E < 1''$. In this regime, the *SExtractor* algorithm may blend the lens and the arcs/multiple images, particularly if we are running in a wide field, where we may not find a suitable fine-tuning to deblend all objects of interest. In order to have a method applicable to galaxy-galaxy Strong Lensing we sought for methods that could be directly applied in cut outs, i.e., is not sensitive to the fine tuning in the deblending process. The natural choice was to look into Convolutional Neural Networks (hereafter CNN) algorithm. This kind of Neural Network has been developed for image recognition tasks. In recent years the CNN has been used in Astronomy applications (Hálą 2014; Hoylę 2016; Huertas-Company et al, 2015). In particular Petrillo et al. (2017) applied this kind of approach to Kilo Degree Survey (KiDS; de Jong et al, 2015) to search for Strong Lenses. We developed our method and performed tests on a sample of simulated lens as in the context of the Gravitational Lens Finding Challenge[6] (PI. R. Benton Metcalf) in which we participated using the methods described below.

4.5.1 Gravitational Lens Finding Challenge data sample

The Gravitational Lens Finding Challenge is an initiative of the Bologna Lens Factory[7] (hereafter BLF) group. The BLF is a database for simulated gravitational lenses. The aim of the Challenge is to accurately quantify the detection efficiency and bias of automated lens detectors by running the algorithms in a sample of thousands of simulated lens.

In this first generation of the challenge, the focus was on the galaxy-galaxy Strong Lensing. In the development of our CNN Lens finder method, we used two training sets from simulations. The first C.1 mocks a space-based survey. Though it has less noise and PSF

[6]for further information see: http://metcalf1.bo.astro.it/blf-portal/gg_challenge.html
[7]http://metcalf1.bo.astro.it/blf-portal/index.html

than the second group (C.2) it is a single band survey. The data set consists of 20,000 objects among $\sim 50\%$ lensed and $\sim 50\%$ unlensed sources. The data set C.2 mocks a ground based wide-field survey. It also consists of 20,000 images but in four bands *u,g,r,i*. The bands represent the galaxies in the appropriate redshifts. However, we have no information of the redshifts. The sample C.2 presents some image artifacts and masked regions. All images are 101×101 pixels. This is an important feature as the CNN algorithm requires images of the same size.

4.5.2 Convolutional Neural Networks

Convolutional Neural Networks are a powerful technique for supervised machine learning well suited for image recognition (see e.g., Krizhevsky et al, 2012; Lawrence et al, 1997; Simard et al, 2003). Particulary, algorithms based on CNNs have won the ImageNet Large Scale Visual Recognition Competition (ILSVRC; Russakovsky et al, 2015) for four years.

The CNN main feature is that its connectivity pattern is inspired by the visual cortex of animals, i.e., how animals process visual information. The visual cortex has a complex arrangement of cells in which some of them are sensitive to small regions of the visual field known as Receptive Fields. The cells assigned to the receptive fields act as local filters and exploit strong spatially local correlations in images. The response of a given neuron to stimuli in its receptive field is mimicked by a convolution operation. The receptive field regions correspond to a small portion of a digital image and a sequence of convolutions of a given input image defines a feature map. The CNNs, as a deep learning algorithm, do not require that we input the features defined by the developer, skipping the object segmentation process. They also have the measurement part embedded in the Neural Network. The training process usually takes advantage of the use of Graphics Processing Units (GPUs) as in the current method. In the following section, we describe how we implement our method for the of the two types of samples of the challenge.

4.5.3 Image preprocessing

We tested two simple image processing routines that visually enhance the images in order to check if they improve the automate arc detection with CNN. We choose a contrast adjustment and apply a low pass band Wiener filter (Wiener, 1964) to reduce the effect of the noise. In Fig. 4.8 we present a simulated lensed image (from the lensing challenge) before and after the wiener filter and the contrast adjustment.

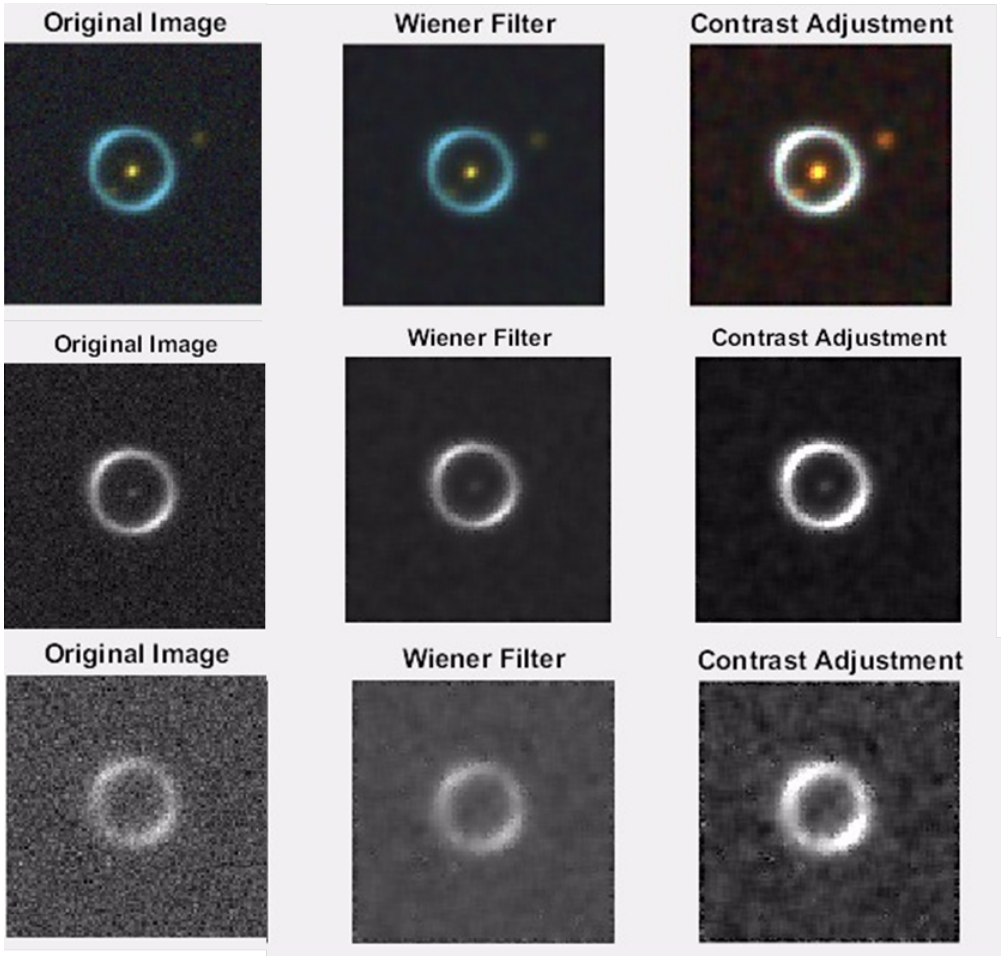

Figure 4.8: *The preprocessing in the images for a color composition of g, r, i (top), for g-band (middle) and u-band (bottom).*

4.5.4 CNN Lens Finder Algorithm Configurations

To implement the CNN method we propose several different configurations combining CNNs in different ways to use multiband information available and including or not the preprocessing phase described in the preceding subsection. To select the configuration that

is better suited to our purposes we carry out several tests to the simulated images produced for the lens finding challenge. As in the ANN case, the CNNs outputs a single float number p in the interval $[0, 1]$ in which $p = 0$ represents, ideally, an image with no lensed source and $p = 1$ represents an image with a lensed source. As in the AMA case, for real applications, one must choose a threshold t such that a system with p above t is considered a lens and is classified as not lens otherwise.

As any supervised Machine Learning Methods, CNNs require a prior training process. For the training process we adopt a similar cross-validation approach as in the AMA case: we use 90% of the sample, chosen randomly as a truth table to train the CNN. The remaining 10% are used for validation purposes. Then we repeat this process 10 times. However, contrarily on what we did in the case of the AMA, instead of randomly chasing the 10% of the object each of the 10 times, we just split the sample into 10 subsamples and pick one subsample at a time for the validation, and the other 9 for the training. In this way, any object appears in the validation only once and the 10 validation samples are thus independent.

Later we evaluate the efficiency for each configuration by analyzing its Receiver Operating Characteristic (hereafter ROC) curve. This curved can be defined as the Completeness c (also known as True positive rate) versus a False Positive Rate, f, with the same definitions as the ones described in section 4.2.4. Each point in the curve represents a given $c(t)$ and $f(t)$ for a threshold t. For $t = 0$ we have both $c = 0$ and $f = 0$, whereas for $t = 1$. Thus, all ROC curves start at $(0, 0)$ and end at $(1, 1)$. For a totally random classification the ROC is a straight line $c(t) = t$ and $f(t) = t$. A useful measurement of the quality of the classification is the area under the ROC, a_{ROC}. For an ideal classifier we would have $a_{ROC} = 1$ and for a random classifier $a_{ROC} = 0.5$. Other interesting quantities are c_{10} and c_0, which are the completeness when we have a maximum of 10 or 0 false positives. For our 2000 images cross-validation groups, this represents c when f is ~ 0.005 (for c_{10}) and 0 (for c_0). Since our cross-validation samples are small and c_{10} and c_0 are very sensitive to the sample size we considered only c_{10} in our analysis due to resolution limitations.

We have tested CNN configurations for the two sets of images made available for the challenge: single band space-based images and ground-based images in four bands. The current implementation of the CNN code we use work only in single band and on RGB

colour composite. Therefore, if we want to use the information on the 4 available bands, we will have to either combine the bands or use more than a single CNN.

We start with the simplest case of the space-based simulations. Here we have considered two configurations:

I.s) A direct input of the single band image in the CNN for classification.

II.s) Use of wiener filter and contrast adjustment functions in the image, then using the resulting image as a direct input in the CNN for classification.

The results will be discussed in section 4.5.5.

In the case of ground-based simulations, as mentioned above, we either combine 2 of the 4 bands to end up with 3 bands for a single RGB CNN (configuration I below) or we use multiple CNNs to use the information available (configuration II to VI). To combine the outputs of several CNNs, we use a Support Vector Machine (hereafter SVM; see e.g., Meyer & Wien, 2015; Rebentrost et al, 2014) one of state of the art supervised ANN. The SVN is used to combine outputs of p_i of the several CNN (configurations II, III, IV and VI). Instead of just using only p_i as inputs to the SVM we also tested giving to the SVM the CNN image features (feature maps, configuration V) as inputs. Finally, we also test the preprocessing discussed in section 4.5.3. A more detailed description of each configuration tested is presented below:

I) Combination of bands r and i with the average between bands u and g. Use one CNN for classification.

II) Creation of 1 CNN for each band (total of 4). The 4 outputs are used as input to a SVM classifier which returns the final classification p.

III) Combination into 4 different combinations of bands: RGB $\rightarrow$ (u,g,r), (u,g,i), (u,r,i) and (g,r,i). One CNN for each combination of bands and then use of the output score as input to an SVM classifier.

IV) Average of bands in different combinations RGB $\rightarrow$ (ug,r,i), (u,gr,i) and (u,g,ri). The outputs of these 3 CNNs are inputs to a SVM classifier.

V) Use of CNN-activations (CNN feature maps) as inputs to a SVM classifier, using same combinations of bands of III. The output of each CNN is used as input to a SVM classifier.

VI) Use of wiener filter and contrast adjustment on each band, then using the resulting

images in the same architecture as III.

4.5.5 Results of the CNN Lens finder on the Space Based sample

We present the ROC curves from 10 trainings and validations subsamples for configurations I.s e II.s in the space-based simulations in Fig. 4.9. The a_{ROC}, presented in table 4.4, in both configurations are mostly lower than the multi-band case, presented in the next section, for the 4 best configurations, in which indicates how the CNNs are sensitive to color information to find Strong Lensing. Particularly, configuration II used one CNN per band thus not considering color information and has the same a_{ROC} as our best single band configuration. However, II had more information (4 images for each entry) and a PSF greater than II.s.

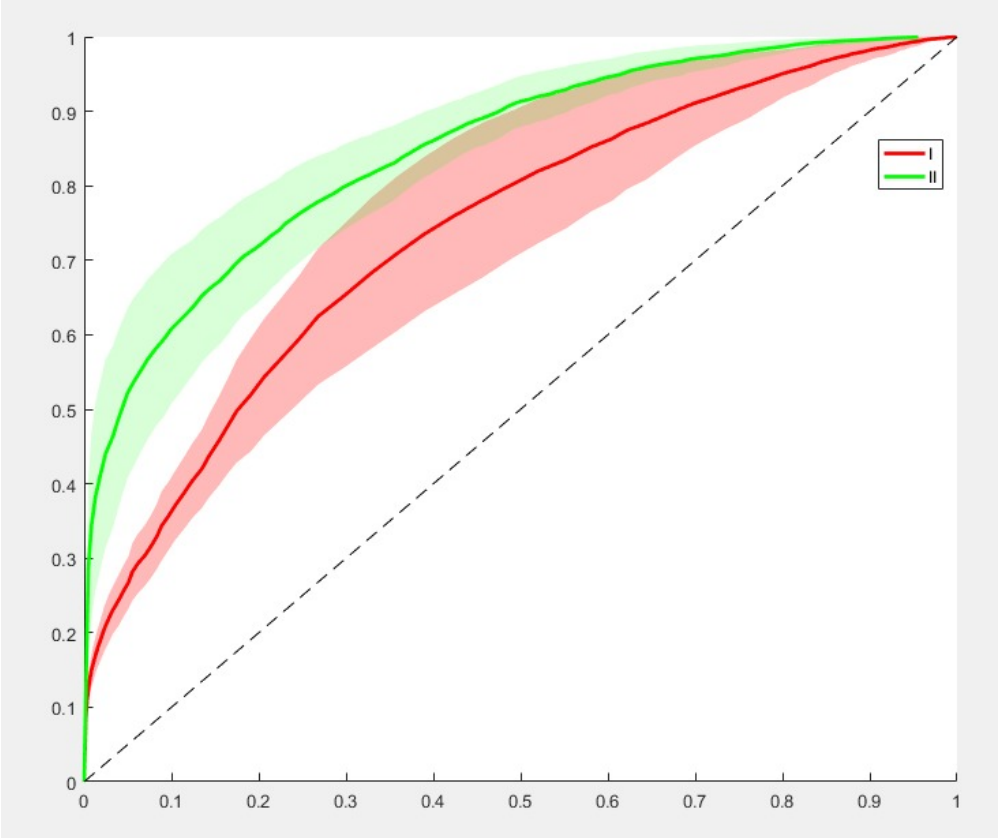

Figure 4.9: *ROC curves for two Space single band configurations with its confidence levels.*

The completeness c of II.s is higher than I.s within 1σ for a large range of f until $t \sim 0.3$. This result highlights the importance of the pre-processing phase. It is worth noticing that

II.s grows very rapidly and thus it has a high completeness for ~ 10 false positives which is a tendency also observed in Fig. 4.9. This result suggests that even if the overall quality of the method as pointed out by a_{ROC} analysis is lower in a single band case, for the low end of f the use of images with lower PSFs may be more valuable in a case where one must minimize the false positives.

4.5.6 Results of the CNN Lens finder on the Ground Base sample

We present the average of ROC curves in the multi-band data for configurations I-VI in Fig. 4.10. The results for a_{ROC} and c_{10} are presented in table 4.4. In Fig. 4.11 we present the standard deviation for the three configurations with highest a_{roc}: III,IV and VI. Although the a_{ROC} are very similar we see in Fig. 4.11 that VI are superior than IV considering its 1σ until the $f \sim 10\%$. It is worth mentioning that in a wide-field application as lensing phenomena are very rare and we would have several orders of magnitude less between lensing systems and fake detections, for our purposes we should concentrate in the low end of f. For the c_{10} feature only I have $c_{10} \sim 10\%$ greater than the others though this analysis must be taken in consideration very careful since in the cross-validation we have ~ 2000 images only and the function may not have enough resolution in this extremely low range.

Table 4.4: *Area under ROC and c_{10} for each configuration considered for the CNN lens finder method.*

Configuration	$a_{ROC}(\%)$	$c_{10}(\%)$
I	$75,4$	$27,1$
II	$81,0$	$17,2$
III	$83,1$	$10,2$
IV	$81,4$	$15,5$
V	$76,1$	$12,3$
VI	$84,1$	$15,5$
I.s	$74,6$	$16,9$
II.s	$81,0$	$42,6$

To give an intuition on the behavior of the code, we show in Fig. 4.12 some examples of the Strong Lensing systems recovered and some of the typical fake detections. By examining the false positive figure we may note that, among other objects, the method classifies some spiral galaxies as lenses.

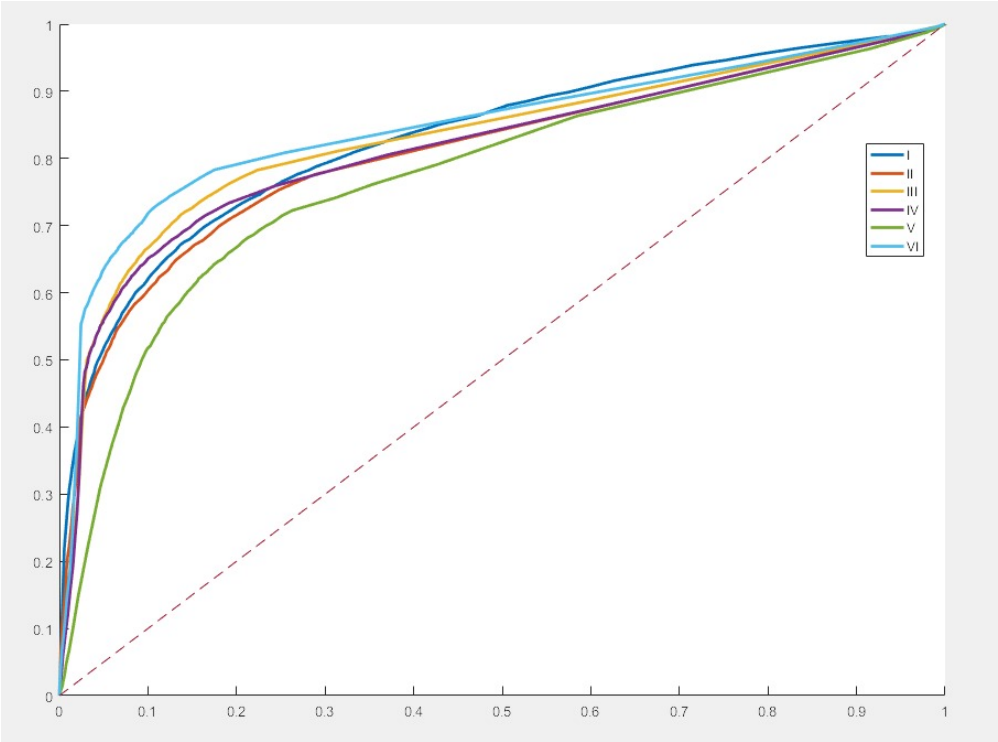

Figure 4.10: *ROC curves for the CNN Lens finder configurations tested in multi-band images.*

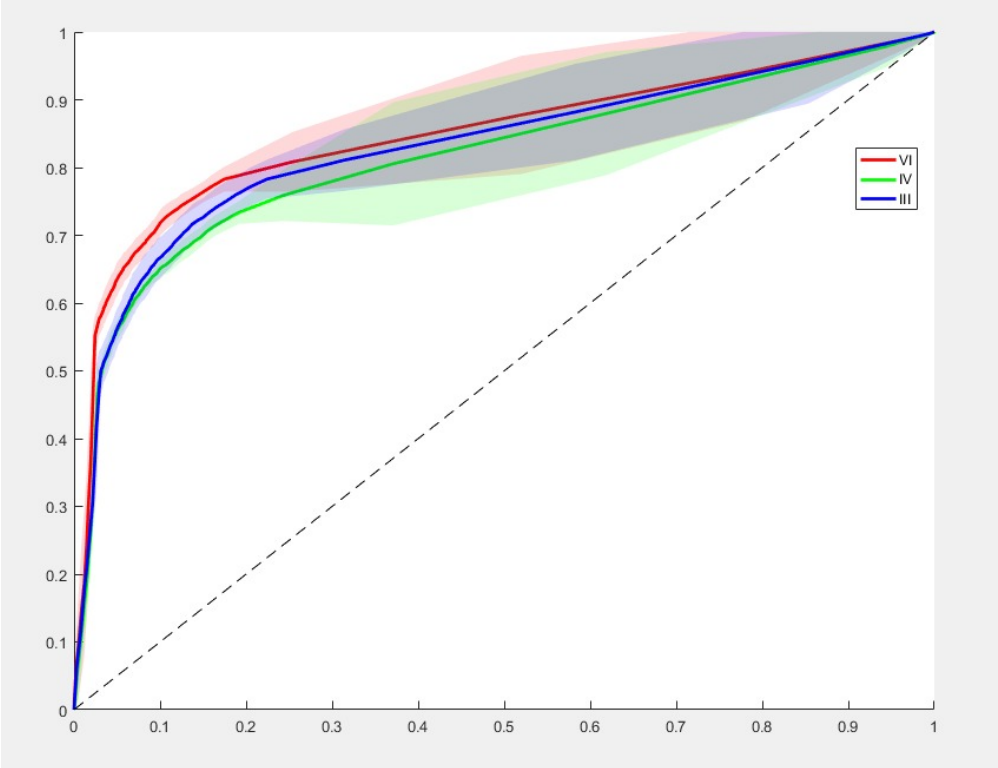

Figure 4.11: *ROC curves for three configurations with highest a_{roc} presented with their confidence levels in CNN Lens finder for multi band images.*

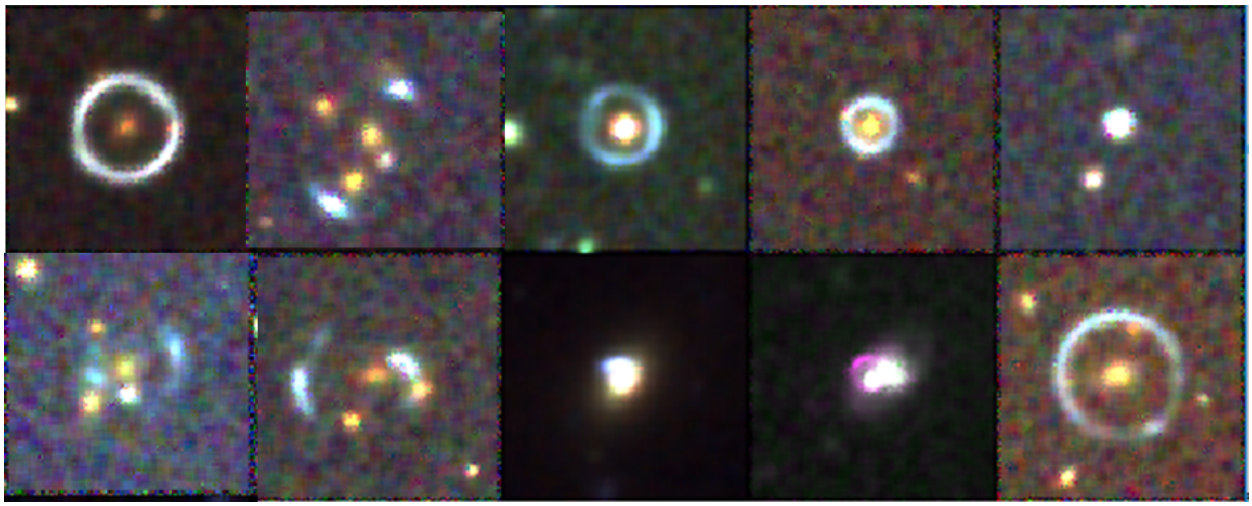

(a) *True Positives*

(b) *False Positives*

Figure 4.12: *Some examples of objects classified by the CNN Lens Finder as Lenses.*

4.6 Discussion

The purpose of the chapter was to present some key aspects in the Strong Lensing finding scenario, one recent example of a human inspection and the two Lensing finders methods proposed in this thesis: AMA, well suited for cluster scale systems and a CNN lens Finder, developed in the context of the Gravitational Lens Finder Challenge, and well suited for galaxy scale lensing.We also provide a simple example of an application of AMA in 4 HST images of Strong Lensing in clusters and the application of the CNN arcfinder to the Strong Lens Finder Challenge. We illustrate the training and validation processes for both methods in simulated arcs.

The major novel aspects of AMA are the use of the Mediatrix method in step 3 of the

arc finding process and the use of simulations. The simulated arcs are used not only to train, but also to find a good set of ANN configurations for step 4. There is room for many improvements in the processes described in the AMA development, most notably in the use of more realistic simulations and increasing the number of systems in the application to real data, but also in other aspects arc detection.

On the object identification and segmentation side, betterments can be implemented in order to detect faint sources, avoid the breaking of large arcs, improve on the deblending with nearby objects, and to find and segment sources in high background regions, which are known issues for arc identification. Although `SExtractor` does not deal with all these issues in an optimal way for arc detection, it has been used in many arc finders for their object identification to some degree (e.g., Estrada et al, 2007; Horesh et al, 2005; Joseph et al., 2014; Kubo & Dell'Antonio, 2008; Marshall et al, 2009; Maturi et al, 2014). A better performance than running `SExtractor` in a straight way, as in the current work, has been obtained by carrying out multiple runs of this code with different thresholds (Horesh et al., 2005), or by using `SExtractor` only for pixel thresholding (Kubo & Dell'Antonio, 2008). Other arc finders use different approaches for object detection and segmentation, which are specifically oriented toward identifying arcs (e.g., Alard, 2006; Lenzen et al, 2004; More et al, 2012; Seidel & Bartelmann, 2007; Xu et al, 2016).

A key issue for detection and segmentation for arcs is that these objects are often embedded in the haloes of bright galaxies (especially for galaxy-scale arcs and radial arcs) or blended with foreground galaxies (especially for arcs in clusters). One approach that has been implemented to address this issue is to fit and subtract the light profile of galaxies, as in Brault & Gavazzi (2015); Sand et al. (2005). Several codes have been proposed in the literature to this end (e.g., Barden et al, 2012; Vikram et al, 2010; Yoon et al, 2011), often running `galfit` (Peng et al, 2010) recursively to fit each galaxy by a combination of elliptical brightness distributions with Sersic (1968) profiles. Advanced versions of `SExtractor` also fit and subtract all identified objects in a field (e.g., Desai et al, 2012; Durret et al, 2015, Moraes et al., in prep.). Other schemes to subtract objects from images, which could be useful for arc finding have also been proposed (e.g., Jiménez-Teja & Benítez, 2012). The central galaxy removal has been already exploited by Paraficz et al. (2016) and Joseph et al. (2014)

using Principal Component Analysis (PCA) in context of other Lens finder approaches. A different approach has been carried out by Xu et al. (2016), who propose a new detection and segmentation scheme, working in intensity difference space, which performs well in bright halos without the need of subtraction.

Regarding the preselection, for applications to wide-field surveys this phase must also include the removal of image artifacts such as satellite tracks, star spikes, and regions with a large amount of noise or with a steeply varying background. In the example of HST cluster images, we removed noisy regions by simply cutting off objects that are close to the CCD borders. However, the AMA code already includes a proper handling of survey masks, which are produced to avoid bright star halos and spikes, satellites, and other image features. The approach of Xu et al. (2016) is also well suited to remove diffraction spikes without the need to use masks and may be useful for less bright nonmasked stars whose spikes could contaminate the arc detection.

For object measurement, we propose the use of the Mediatrix filamentation method, and several parameters derived from it, as it was designed for elongated and curved objects. Most arc finders end up using fewer parameters and simpler measurement schemes to characterize the arc candidates, such as L and L/W, and only in a few cases include estimates of the curvature (Estrada et al, 2007; Kubo & Dell'Antonio, 2008). However, other sets of inputs in addition to the Mediatrix inputs could be given to the ANN, such as higher order moments of the brightness distribution, including the arcness (Kubo & Dell'Antonio, 2008).

We argue that by using a machine learning algorithm for the final candidate selection (in this case a back-propagation ANN) one may achieve a better efficiency in finding arcs than using hard cuts on a few variables. By working on a multidimensional parameter space, it is possible to deal with correlations among the variables and empirically obtain combinations that represent gravitational arcs. For example, arcs tend to be more curved and smaller at galaxy scales than in massive clusters, such that a single cut in L/W or arcness would not be optimal for finding arcs at both scales.

Artificial neural networks were first used by Estrada et al. (2007) to search for Strong Lensing systems. In their case, the simulated lensed sources are arcs derived from simply sections of a circle with a surface brightness profile that is uniform along the tangential

direction and is convolved with a Gaussian with FWHM similar to the typical seeing of the images. The ANN is trained using a hundred such simulated arcs covering a range of sizes and brightnesses, which are added to SDSS images. The objects are also identified with `SExtractor` and the preselection is also carried out using an estimate of the object's elongation. Finally, four inputs are given to the ANN, based on a fit of the object by a circle and on a determination of the object's length (using its furthest pixels). Estrada et al. (2007) study the efficiency for recovering the simulated arcs both for a visual inspection and for the automated process as a function of peak surface brightness and L/W. A maximum efficiency of 40% (concerning the number of simulated arcs) is achieved in the automated search. The AMA code can be seen as an improvement on Estrada et al. (2007) in the sense that we use more realistic simulated arcs and a wider set of input measurements well suited to characterize the arcs, in addition to tuning the ANN configurations to improve the completeness.

Of course the key to a good performance in a learning algorithm is the realism of the training sample. Many improvements can be incorporated into the simple `AddArcs` simulations described in this work, such as considering more realistic lenses (e.g., Horesh et al, 2011; Xu et al, 2016) and sources (Horesh et al, 2011; Kubo & Dell'Antonio, 2008; Marshall et al. , 2009). Moreover, in addition to having a realistic sample of isolated arcs, those have to be added to real images, for example, to address the issue of blending with other sources and of embedding in the halo of bright galaxies in cluster cores. Other works have used simulations to test arc finders, define their parameters, or train their methods, and in some cases determine the selection functions (e.g., Brault & Gavazzi, 2015; Gavazzi et al, 2014; Horesh et al. , 2011, 2005; Joseph et al, 2014; Kubo & Dell'Antonio, 2008; Marshall et al, 2009; Xu et al, 2016). Another possibility is to use the growing number of strong lensing systems detected in wide-field surveys and HST images to perform the training on real data sets. For example, over 600 candidate systems have been detected in recent studies using CFHTLS data (Brault & Gavazzi, 2015; Gavazzi et al, 2014; Maturi et al, 2014; More et al, 2016; Paraficz et al. , 2016), which could be used to train and better characterize the AMA and other arc finders. By training and validating the ANN with more realistic simulated arcs or with real data, we expect to reach a better agreement for c in comparison to applications to other data

sets (and therefore to achieve a higher completeness), which is different from what we found when applying our trained ANN to the HST data.

The CNN lens finder was a more direct application of a Machine Learning Algorithm, particularly a Deep Learning Method, i.e. a method that derives the sample of relevant features by exploring the data. The main goal in our analysis was to explore several configurations, including a pre-processing and combinations of input images and concatenate machine learning algorithms (a combination of CNNs and/or SVMs) to explore a good architecture for our CNN lens finder. In a recent paper Petrillo et al. (2017) also use CNN for arc finding. Although they work on the KiDS multi-band data, they use only the r-band images and therefore their method is more comparable to our single-band implementation. A comparison of the two codes was made as part of the Gravitational Lens Challenge and a paper including all the participating algorithm is in preparation.

For the Challenge we worked on two samples of $100,000$ cut outs, one for the space-based and another for the ground-based (simulated) data. We participated using configuration VI and II.s for the ground and space based samples respectively. In the challenge preliminary results, configurations II.s ranked third out 15 in the c_0 comparison, while the Petrillo et al. (2017) based approach were on the eleventh position. In addition, our II.s configuration performed better than human inspection. In the area under the ROC analysis our methods gave essentially the same results: $a_{ROC} = 0.813$ for our CNNs while Petrillo et al. (2017) based approach obtained $a_{ROC} = 0.818$. In the multi-band data our method performed twelfth out of 16 in the c_0 analysis, but still better than at least one CNN based approach.

The CNN lens Finder also has lots of room for improvements. In particular the preprocessing phase must be exploited. To deal with the blending between the light of the lens and the source one promising approach would be to remove the light of the lens galaxy even if we are not as sensitive to segmentation issues as discussed in the AMA algorithm. Cut outs with the foreground galaxy subtracted would probably be more distinguishable as lenses. Although the CNN is one of the top algorithms for image recognition, it still has some important limitations. For instance, the images must have the same size, which is a problem, as arcs may span a large interval in radii, especially from galaxy to cluster scale lenses. Too big cut outs could include many objects in the cut out and too small would

hinder the detection of large Einstein radii systems. Another important issue from running on cut outs of the same size is that it usually implies to run over a catalog of pre-selected objects, such as Luminous Red Galaxies (LRGs), and not the whole field. To deal with this kind of limitation one may explore a new class of CNNs named Region-based Convolutional Neural Networks (R-CNNs; see, e.g., Ren et al, 2015), which can detect an object in images of any size within a wider range of angular sizes.

In general, the several Lens finders proposed in the literature carry out an end-to-end approach from the science image to a list of candidates, implementing at least three (Pre-selection/Preprocessing, Measuring and Final Classification for deep learning method) out of four steps (all other Pattern Recognition methods) that we refer to in this contribution. However, they have their own solutions for each step with different degrees of sophistication and specificity for finding Lenses. For example, in the AMA we focus on the third and fourth steps, respectively, by using a set of object measurement parameters that are well suited to arcs and a trained ANN, while most methods use simple cuts on a few parameters for the final classification. On the other hand, we use a generic object segmentation code that is not optimal for arcs (`SExtractor`). In the CNN Lens Finder case we focused our efforts in the Final Classification (Machine Learning algorithm architecture) though there is an enormous room for sophistication in the Preprocessing phase. For most methods, these four steps could be performed interchangeably. Therefore, if the codes are presented in a modular way, we would be able to test the performance of each step independently. Moreover, new lens finders could be created combining the solutions for each step that work better in specific situations. Several possible concatenations of the lens finder modules could also be compared using their end-to-end performance.

After a decade of progress in the development of Strong Gravitational Lens Finders, several codes are ready for exploring the new generation of wide-field surveys in the quest for gravitational arcs. However, more progress is still needed for fully automated runs so as to produce samples that can be readily exploited for their applications. Besides improving the efficiency in some situations, the most important is to limit the false positives to a level low enough to be corrected for and certainly less than the number of real systems, as thousands to hundreds of thousands strong lenses are expected in the forthcoming data.

Different strategies have been proposed and implemented to address these issues. Combining aspects of these solutions, which are more suited to each step of lensing detection, seems a natural way to proceed. We believe that using neural networks or other machine learning methods may provide an important contribution to the task of selecting more complete and pure samples of gravitational arcs for a broad range of deflector scales and backgrounds.

Chapter 5

Probing Cosmology in Different Observational Conditions

The Strong Lensing effects are sensitive to the mass distribution in the lens and the angular diameter distances involved. It is worth mentioning that this effect does not depend on the dynamical state of the object acting as lens and is also achromatic. As discussed in chapter 2, one may infer the underlying geometry of the universe by assessing the cosmological angular diameter distances. The lens equation (2.21) can be written with its cosmological dependence explicit as

$$\vec{\theta} = \vec{\beta} + \frac{2}{c^2}\frac{D_{LS}}{D_{OS}}\nabla_{\xi}\psi(\vec{\xi}), \tag{5.1}$$

where we used 2.29, $\vec{\beta}$ is the source position and ψ the projected Newtonian potential given by 2.25.

Therefore, in principle, to obtain the cosmological constrains provided by the angular diameter distances one must describe the potential, i.e., the mass distribution, with a precise, and reliable model. However, if we have information from sources at different redshifts, we may be able to remove (or at least reduce) the dependence of the results on the lens potential. In particular, we may be able to place constraints on certain distance ratios, from which cosmological constraints can be derived.

The aim of this contribution is to assess how those cosmological constraints are affected by the observational conditions, in particular by the depth and Point Spread Function (PSF) of the images. We use a reference model constructed from deep space-based images and ex-

tensive spectroscopic follow-up of a massive cluster with several families of multiple images. We then "degrade" those images to mimic the aforementioned effects, i.e., we artificially decrease the image depth and simulate a larger PSF. The degraded images have less identifiable multiple images of the sources than the original one, which will impact the cosmological constraints derived from modeling the multiple images. In the following sections, we describe how to obtain constrains from a set of families of multiples images, i.e., multiple images from sources at different positions and redshifts. We then describe our procedure for degrading the images. Finally, we present our preliminary results on how the cosmological constraints are affected by the simulated observational conditions.

5.1 Strong Lensing Constraints from multiple images

The underlying Cosmology in the lens equation (5.1) is embedded in D_{LS}/D_{OS}, also known as efficiency E, which is independent of H_0 as can be seen in (2.16). The efficiency is however degenerate concerning the absolute normalization of lens mass. To break this degeneracy and constrain the cosmological parameters, we may use systems with multiple sources. In this approach, the cosmological constraints arise from the distance ratios:

$$\Xi_{S1,S2}(\vec{\pi}) = \frac{D(\vec{\pi})_{LS,1} D(\vec{\pi})_{OS,2}}{D(\vec{\pi})_{LS,2} D(\vec{\pi})_{OS,1}}, \tag{5.2}$$

where $\vec{\pi}$ is the set of cosmological parameters and the subscripts 1 and 2 refer to sources at redshifts z_{s1} and z_{s2} respectively.

To illustrate why the distance ratios are the physical quantity determined by the use of sources at different redshifts, let us consider the very simple and idealized case of a double Einstein ring produced by a Singular Isothermal Sphere (SIS) model with velocity dispersion σ_v. The rings are generated by sources at redshift z_{s1} and z_{s2}. In this case, the observed "source positions" are the Einstein radii, θ_{E1} and θ_{E2}, given by Eq. (2.35). The dependence on the SIS mass parameter σ_v can be removed by computing the ratio of the Einstein radii:

$$\frac{\theta_{E1}}{\theta_{E2}} = \frac{4\pi c^2 \sigma_v^2 D_{LS,1} D_{OS,2}}{4\pi c^2 \sigma_v^2 D_{LS,2} D_{OS,1}} = \frac{D_{LS,1} D_{OS,2}}{D_{LS,2} D_{OS,1}}. \tag{5.3}$$

Therefore, the observable quantities determine the distance ratios, in a way that is independent of the lens mass parameters. Of course this is a very idealized model and the lens parameters may not cancel exactly in more realistic cases. Nevertheless, it is useful to gain some intuition on how we may use several sources to assess the underlying cosmology and reduce the degeneracies with the lens mass parameters.

To reach acceptable constraints one must use several families of multiple images arising from sources at different redshifts. This approach has been used with a few massive clusters with extensive spectroscopic coverage for the sources. See, for instance Caminha et al. (2016a); Jullo et al. (2010); Soucail et al. (2004), which apply these ideas to the galaxy clusters Abell S1063 (also known as RXC J2248.7−4431), Abell 1689 and Abell 2218, respectively. If we fix a high redshift source z_{s2}, the most suitable redshift for z_{s1} to distinguish between different cosmological models is $z_{s1} \approx z_L$. The highest the difference between z_{s2} and z_{s1} the best is the constraint (Golse et al, 2002). It is worth noticing that a source redshift close to the lens redshift means that the strong lensing cross sections are smaller and the image must be very close to the lens center which make the detection difficult since the it might be embed in the BCG light. Nevertheless, the difference between different Cosmological scenarios are of order of few %, for instance Golse et al. (2002) shown that is less than 3% between the Einstein-de Sitter model (EdS) and a flat ΛCDM one, indicating that we must have a robust and accurate model for the lens mass distribution in order to define cosmological constraints.

Such requirements lead to a concern on how the systematics in strong lensing modeling may bias the determination of the mass distribution. In Priewe et al. (2016) the authors show that magnification maps based on different lens inversion techniques may differ from each other by more than their nominal statistical errors, which indicates that some models underestimate their uncertainties. Substructures in the lens, whether baryonic or dark matter may also bias the modeling and resulting in the so called flux ratio anomalies (Despali & Vegetti, 2016; Gilman et al, 2016).

The study of possible biases arising from the analyses of clusters with many families of multiple images is a very relevant and active topic of research in the field. In this chapter. we focus on one aspect, namely what happens if we have observational conditions (especially

depth and seeing) that are worse than those deep space-based data used in the current studies of cosmology with strong lensing. This is particularly relevant for the next generation surveys, such as the Large Synoptic Survey Telescope (LSST; LSST Sci. Collaboration et al, 2009), the Euclid Mission (Refregier et al, 2010), and the Wide-Field InfraRed Survey Telescope (WFIRST; Spergel et al, 2015). By how much are the error bars on cosmological parameters enlarged from analyses of strong lensing clusters on the data from these surveys? Do biases on these parameters arise with respect to the high-quality data? This will be addressed in the following sections.

5.2 Strong Lensing Modeling and data

5.2.1 RXC J2248.7−4431

We focus our analysis on the cluster RXC J2248.7−4431 (hereafter RXC 2248), in which RXC stands for *ROSAT* X-ray Cluster. This cluster was first cataloged in Abell et al. (1989) as Abell S1063. It is a rich cluster at redshift $z_L = 0.348$, with X–ray bolometric luminosity of $(6.95 \pm 0.1) \times 10^{45}$ erg s^{-1} with the X-ray temperature within R_{500} as $11.1^{+0.8}_{-0.9}$ keV (Maughan et al, 2008). This cluster has dozens of multiple images many of them are spectroscopically confirmed (see, for example, Caminha et al, 2016b). This cluster was extensively analysed by several authors (e.g. , Boone et al, 2013; Cruddace et al, 2002; Gruen et al. , 2013; Karman et al, 2016, 2015; Richard et al, 2014). There is an evidence that indicates that RXC 2248 may be a merging system, which is supported by an offset between the galaxy distribution and the peak of X-ray isophotes. It is worth noticing that the analysis in Gómez et al. (2012) shows that the velocity distribution is better fitted in the merging model. However, previous strong lensing analyses (Johnson et al, 2014; Monna et al, 2014; Richard et al, 2014) have shown that the cluster total mass distribution of RXC 2248 can be reliably modelled by a single elliptical dark matter halo, added to the galaxy cluster members. Many studies have measured the cluster mass with a reasonable agreement (on the order of 10^{14} solar masses) using different probes. In particular, we mention an analysis that compares the robustness of the stellar mass fraction for a high quality set of images from Cluster Lensing And Supernova survey with Hubble (CLASH) and the wide-field ground

based image from the Dark Energy Survey (DES) by Palmese et al. (2016). The authors report that they are able to estimate stellar masses from ground based images (DES) within 25% of deep space images (HST-CLASH) values.

5.2.2 Imaging data

For our reference model we use images from the Frontiers Field project (FF; Lotz et al. , 2016) which is a director's discretionary time campaign with HST and the Spitzer Space Telescope. The survey imaged six clusters for over 840 HST orbits with 5σ depth $mag_{AB} \sim 29$ in seven filters using the Advanced Camera for Surveys (ACS) and the Wide Field Camera 3 (WFC 3). To obtain some of the degraded models for our studies, we have also used images from Cluster Lensing And Supernova survey with Hubble (CLASH; Postman et al, 2012). The survey imaged 25 massive galaxy clusters in 17 filters with $5-\sigma$ depth $mag_{AB} \sim 27.5$. We are particularly interested in the filters F475W, F625W and F775W which roughly correspond to g,r an i bands with limiting magnitudes 27.6, 27.2 and 27.0 for 5σ limiting magnitude, respectively. To constrain our models we make use spectroscopic redshifts available for RXC 2248, many of them obtained as part of Very Large Telescope (VLT) spectroscopic follow-up campaigns with the VIsible Multi-Object Spectrograph (VIMOS; Le Fèvre et al. , 2003) and the Multi Unit Spectroscopic Explorer (MUSE; Bacon et al, 2010). The redshift data is described in Balestra et al. (2013); Boone et al. (2013); Caminha et al. (2016a); Karman et al. (2016, 2015); Richard et al. (2014).

5.2.3 Modelling definitions

Our starting strong lensing model, which is revisited after the degradation procedure, is built upon the presented in Caminha et al. (2016a) with minor changes discussed below. The modeling is performed by a parametric approach using the Lenstool software (Jullo et al. , 2007).

Since the optical and X-ray images do not indicate a large asymmetry nor massive substructures near the multiple images, three dominant components were considered for the total mass distribution in the lens modelling. The first one is a smooth component describ-

ing the halo(s) of extended dark matter distribution. The second to accounts for the mass distribution of the Brightest Cluster Galaxy (BCG). The third component is made out of small scale halos associated to cluster members. In Caminha et al. (2016a) the authors used the three components and checked if the presence of external shear could improve the overall fit, though they could not find any significant improvement. However, with the addition of new multiple families described by Karman et al. (2016), they found that the overall fitting gets improved with the addition of an additional halo component associated to a secondary system of multiple images. In this contribution, we performed the modeling using these four components. The three main halos were modeled by a Pseudo Isothermal Elliptical Mass Distribution (hereafter PIEMD, Kassiola & Kovner, 1993) with projected mass density given by (2.36). This is a parametric model with 6 free parameters which follow: the centre position x_0 and y_0, the ellipticity and its orientation angle[1], i.e. ε and θ, the velocity dispersion σ_v and the core radius r_{core}.

To account for the cluster member halos, we considered only galaxies within $1'$ radius from the BCG center. This radius was chosen since it encloses all multiple images considered. This condition improves the computational time, and it is worth noticing that we do not expect outer regions to affect significantly the positions of multiple images and, as a consequence, the constraints. The procedure to determine a cluster member is described in Caminha et al. (2016a), which is our reference model, we include 139 cluster members in the model, 64 of which are spectroscopically confirmed.

We consider each cluster member as dual pseudoisothermal elliptical mass distribution (dPIE, Elíasdóttir et al, 2007). For simplicity, we choose zero ellipticity and core radius, and a finite truncation radius r_{cut}. Following a standard procedure in cluster-scale strong lensing analyses and to reduce the number of free constrains (e.g., Grillo et al, 2015; Halkola et al. , 2006; Jullo et al, 2007) we use the following velocity dispersion-luminosity and truncation radius-luminosity scaling relations for each i member:

$$\sigma_{v,i}^{gals} = \sigma_v^{gals} \left(\frac{L_i}{L_0}\right)^{0.25}, \; r_{cut,i}^{gals} = r_{cut}^{gals} \left(\frac{L_i}{L_0}\right)^{\alpha}, \tag{5.4}$$

[1]the horizontal is the principal axis and the angle is counted counterclockwise

where σ_v^{gals} and r_{cut}^{gals} are constant for all galaxy cluster members, L_0 is a reference luminosity associated to the second most luminous cluster member, marked in a magenta circle (Fig. 5.1). The first relation describes the velocity dispersion scaling with the total luminosity as in the the Faber-Jackson relation. For the second relation we pick $\alpha = 0.5$ which, as we will see below, represents a constant mass-to-light ratio. Considering this the total mass in a cluster member is

$$M_i = \frac{\pi}{G}(\sigma_v^{gals})^2 r_{cut}^{gals} \left(\frac{L_i}{L_0}\right), \tag{5.5}$$

Therefore, from now on, there are only two free parameters for the whole set of galaxy cluster members, the reference velocity dispersion σ_v^{gals} and truncation radius r_{cut}^{gals}, with exception of the BCG for each σ_v^{BCG} and r_{cut}^{BCG} is fitted independently.

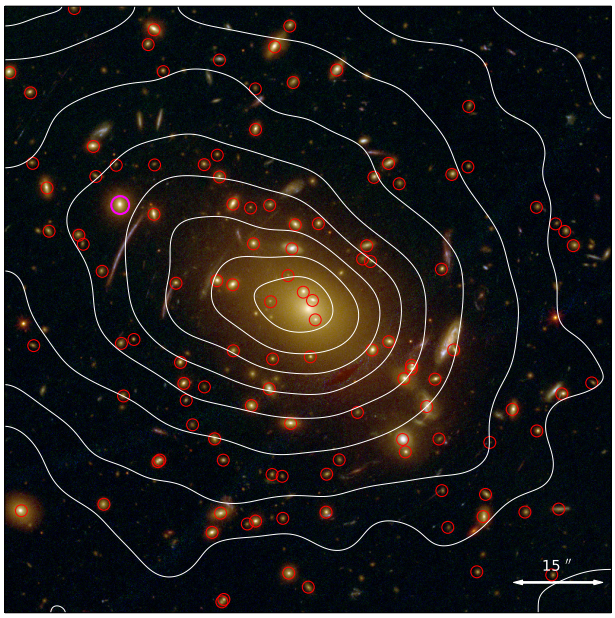

Figure 5.1: *Colour composite image of RXC J2248 overlaid with the* Chandra *X-ray contours in white (Gómez et al, 2012). Red circles indicate the selected cluster members in the reference model. The magenta circle shows the second brightest cluster member. Its luminosity is used as the reference for the normalization of the mass-to-light ratio of the cluster members, figure reproduced from Caminha et al. (2016a).*

To obtain the Cosmography we used a set of 15 families with 41 multiple images. We follow the nomenclature from Caminha et al. (2016a) in which a family is identified by a number and its multiple images by a letter. We also added 5 families ($23 - 28$) which were identified using MUSE data in Karman et al. (2016). Images which were not spectroscopically confirmed, that are close to a cluster member, possibly lensed by Line of Sight (LOS)

structures, or not having a secure counter image were excluded. The multiple families and images for our reference model are presented in Table 5.1. All images used in the reference model were visually identified in a stacked image using FF data in filters F435W, F606W, F814W, F105W, F125W, F140W, F160W. We used the Trilogy application (Coe et al, 2012) to combine the filters and to define a scale that improved the visualization. Trilogy re-scales the image by defining a log scaling constrained at three points, this, in general, improves the visualization by enhancing the faint objects while not saturating bright sources. The code returns png images that we converted to fits files. The Trilogy code has been recently used by the CLASH team and also by the DECam Legacy Survey (Blum et al, 2016) team.

5.3 Inverse Strong Lensing Modelling

In order to derive the free Cosmological and cluster parameters, we have used an optimization method to fit the data based on a Bayesian Markov Chain Monte Carlo (MCMC) approach implemented in the software *Lenstool* (Jullo et al, 2007). From the lensing model and the peaks of the image position, which are the constraints we may define the χ^2 from multiple image system i as

$$\chi_i^2 = \sum_{j=1}^{n_i} \frac{[x_{\rm obs}^j - x^j(\vec{\pi}, \vec{\Delta})]^2}{\sigma_{ij}^2} \ , \tag{5.6}$$

where n_i is the number of images from the source i, $x^j(\vec{\pi}, \vec{\Delta})$ is the position of the peak of image j predicted by the lensing model, whose halo parameters are $\vec{\Delta}$, the Cosmological parameters are $\vec{\pi}$ and the error on the position of image j, is σ_{ij}. In the optimization process, we assume that the errors associated with the measurement of the image positions are Gaussian and uncorrelated from one image to another. Thus, we may define the likelihood function as

$$\mathcal{L} = \Pr\left(D|x(\vec{\pi}, \vec{\Delta})\right) = \prod_{i=1}^{N} \frac{1}{\prod_j \sigma_{ij}\sqrt{2\pi}} \exp^{-\frac{\chi_i^2}{2}} \ , \tag{5.7}$$

where N is the number of sources.

Since we are considering a situation in which the available data is not completely sufficient

Table 5.1: *Multiple image systems in RXC J2248.7−4431*

ID	RA	DEC	z_{spec}
2a	342.19559	−44.52839	$1.229^{a,b,d}$
2b	342.19483	−44.52735	$1.229^{a,b,d}$
2c	342.18631	−44.52107	$1.229^{a,b}$
3a	342.19269	−44.53118	$1.260^{a,b}$
3b*	342.19212	−44.52984	$1.260^{a,b}$
3c	342.17986	−44.52156	1.260^{d}
4a	342.19317	−44.53652	—
4b	342.18782	−44.52730	$1.398^{a,b}$
4c	342.17919	−44.52358	$1.398^{a,b,d}$
6a	342.18847	−44.53998	$1.428^{a,b,e}$
6b	342.17585	−44.53254	1.428^{e}
6c	342.17420	−44.52831	$1.428^{d,e}$
7a	342.18006	−44.53842	1.035^{e}
7b	342.17554	−44.53590	1.035^{e}
7c	342.17191	−44.53023	1.035^{e}
13a	342.19369	−44.53014	—
13b	342.19331	−44.52942	—
14a	342.19088	−44.53747	$6.112^{b,c,e}$
14b	342.18106	−44.53462	$6.111^{b,c,e}$
14c	342.18904	−44.53004	—
14d	342.17129	−44.51982	$6.111^{b,c}$
14e	342.18408	−44.53162	—
18a	342.18150	−44.53936	4.113^{e}
18b	342.17918	−44.53870	4.113^{e}
20a	342.18745	−44.53869	3.118^{a}
20b	342.17886	−44.53587	3.118^{a}
20c	342.17065	−44.52209	—
23a	342.19023	−44.52976	0.73010^{f}
23b	342.18954	−44.52882	0.73010^{f}
24a	342.1983800	−44.53575200	2.97800^{f}
24b	342.1924400	−44.52506900	2.97800^{f}
24c	342.1815100	−44.52025400	2.97800^{f}
25b	342.1887700	−44.52277200	5.23730^{f}
25c	342.1838000	−44.52123800	5.23730^{f}
26a	342.1908500	−44.53565600	5.05100^{f}
26b	342.1901500	−44.53095900	5.05100^{f}
27a	342.2021700	−44.53211100	3.28600^{f}
27b	342.1960800	−44.52295300	3.28600^{f}
27c	342.1893000	−44.51871800	3.28600^{f}
28a	342.1991000	−44.53600400	3.16900^{f}
28b	342.1919800	−44.52417700	3.16900^{f}
28c	342.1829200	−44.52031200	3.16900^{f}

Multiple images used in our reference model with their coordinates and redshifts. The coordinates correspond to the luminosity peak used in the strong lensing models. a Caminha et al. (2016a) b Balestra et al. (2013); c Boone et al. (2013); d Richard et al. (2014); e Karman et al. (2015); f Karman et al. (2016).

or reliable to determine the models one may infer that the use of a Bayesian approach may be useful for the model fitting by the use of priors and/or in combinations of data from other experiments. For the model $x(\vec{\pi}, \vec{\Delta})$ with the parameters $\vec{\pi}, \vec{\Delta}$ and given data D we may write the so-called Bayes Theorem as:

$$\Pr\left(\vec{\pi}, \vec{\Delta} | D, x(\vec{\pi}, \vec{\Delta})\right) = \frac{\Pr\left(D | x(\vec{\pi}, \vec{\Delta})\right) \Pr(\vec{\pi}, \vec{\Delta})}{\Pr(D)} , \tag{5.8}$$

where $\Pr\left(\vec{\pi}, \vec{\Delta} | D, x(\vec{\pi}, \vec{\Delta})\right)$ is the posterior Probability Density Function (hereafter PDF), $\Pr(\vec{\pi}, \vec{\Delta})$ is the prior PDF for the parameters, and $\Pr(D)$ is a normalization factor known as the evidence. The best fit parameters are the parameters from the maximum in the posterior PDF. The evidence can be interpreted as the probability of getting the data D given a model $x(\vec{\pi}, \vec{\Delta})$ and can be used to quantify the complexity of the model, and thus used in model selection.

In the present case, we have nontrivial posterior PDFs and also dozens of parameters from the halos, cluster members and Cosmology. Therefore, it is reasonable to use Markov Chains to converge progressively from the prior PDF to the posterior PDF due to the computational time involved. The current implementation of *Lenstool* uses 10 interlinked Markov Chains at the same time to avoid any of them from falling in a local minimum.

In all results discussed in this thesis, we considered a flat $XCDM$ cosmology with $H_0 = 70\,\mathrm{km/s/Mpc}$, free Ω_M and a Dark Energy equation of state $p = w_X \rho$, as the one in section 2.2 where we set $w_X = -1$ for a Dark Energy model, with free w_X . We set a flat prior for both Ω_M and w_X ranging from 0 to 1 and 0 to -4 respectively. We choose a large range of priors for w_X since in previous Cluster Strong Lensing studies (for instance, Jullo et al, 2010; Soucail et al, 2004) the contours are very degenerated for $w > 1$ and we are interested in the analysis of the uncertainties arising from the degraded models.

5.4 Mimicking observational effects

Simulating images in different observational conditions has become an essential task for obtaining realistic forecasts in astrophysics and cosmology (e.g., Bergé et al, 2013; Bertin,

2009; LSST Sci. Collaboration et al, 2009; Overzier et al, 2012). Before designing an experiment is it crucial to understand what may be obtained from data and how the experiment systematics behave, e.g., if the planned constraints are feasible and competitive to other probes and surveys.

In this section, we discuss a more direct approach, starting from the real images, to simulate different observational conditions. We concentrate our efforts on how to add observational effects in images, i.e., how to degrade images, to mimic several observational conditions. Our ultimate goal is to investigate the bias in Cosmology from the inverse modeling of strong lensing systems with families of multiply imaged sources due to image degradation.

5.4.1 Point Spread Function

The Point Spread Function, thereafter PSF, characterizes the response from an imaging system to a point source, i.e., how the incident photons are displaced due observational effects such as scattering from atmosphere for ground-based images, or by instrumental issues, for instance, telescope motion blurring (jitter and guiding errors), instrument diffraction and aberrations, optical diffusion effects, or intra pixel response (see, for example, Bertin, 2009). To simulate the PSF we worked with a Gaussian profile

$$G(r) = \frac{1}{\sqrt{2\pi\sigma}} \exp\left(-\frac{r^2}{2\sigma}\right), \tag{5.9}$$

where $\sigma = \frac{PSF_{in}}{2\sqrt{2\log 2}}$, to mimic these effects.

The procedure to add a PSF in HST images with a subtracted background is the following:

1. As the images used in this work had their background subtracted is necessary to estimate their original background. This is so because when we decrease the S/N, we must be able to compute the noise from the background (which, of course, is not changed when we subtract the constant background). We assume that the background effects are essentially a Poisson process where the variance σ is equal to mean N. Therefore by measuring the noise from the background, we are able to recover the original background. For this sake, we Select an area in the original image with no visible sources. Then convert the counts to

units of charge by using the effective gain. Then we define the estimated background as the variance of this image histogram.

2. To determine the PSF in the original image we run SExtractor. Using the output catalog we select a stellar box in the Flux Radius, R_f, versus magnitude M plot. We eliminate objects with FLAGS$>$ 0 (a SExtractor quality flag) and MAG$_{ERR} > 0.1$ (the uncertainty in magnitude, δmag). We use the mean $2 \times R_f$ and its standard deviation to estimate an initial[2] PSF_0. To determine the output PSF $(FWHM)$ we sum in quadrature:

$$PSF_{out} = \sqrt{PSF_0^2 + PSF_{in}^2}, \tag{5.10}$$

3. We add the estimated background to the original image in charge units. Next, we convolve the image with the Gaussian Kernel with a width σ computed from PSF_{in}.

4. Then we add a Poisson noise as follows: each pixel is assigned a new value sampled from a Poisson distribution with the mean given by that pixel value in charge units.

5. Finally, the (constant) background is subtracted from the convolved image.

In Fig. 5.3 we show the original image of RXC 2248 from the CLASH survey for three filters (F475W, F625W and F775W) and the resulting image after Gaussian convolution with a PSF with $FWHM = 0.9$". To check our procedure, i.e., to evaluate if the actual PSF of the convolved image matches the expectation from Eq. (5.10), we need to obtain the stellar box in the resulting image. This was not possible to be done using the HST images of RXC 2248, as they have very few stars. Therefore, as a test, we consider a DES image which covers this same system, but with a much wider field of view. In this case, of course, we have to convolve with PSFs larger than the DES one. The results are shown in Fig. 5.2, where we display the difference between the measured and expected PSF FWHM. The initial PSF obtained in step 2 was $1.2''$. In general, using the above procedure, we recover the desired PSF within less than 10%, which is less than the pixel scale and enough for the purposes of this study.

[2]In the case of the HST images of the cluster under consideration, there are not enough stars to measure the PSF. In this case, we use a typical value of $PSF_0 = 0.1''$ from Postman et al. (2012).

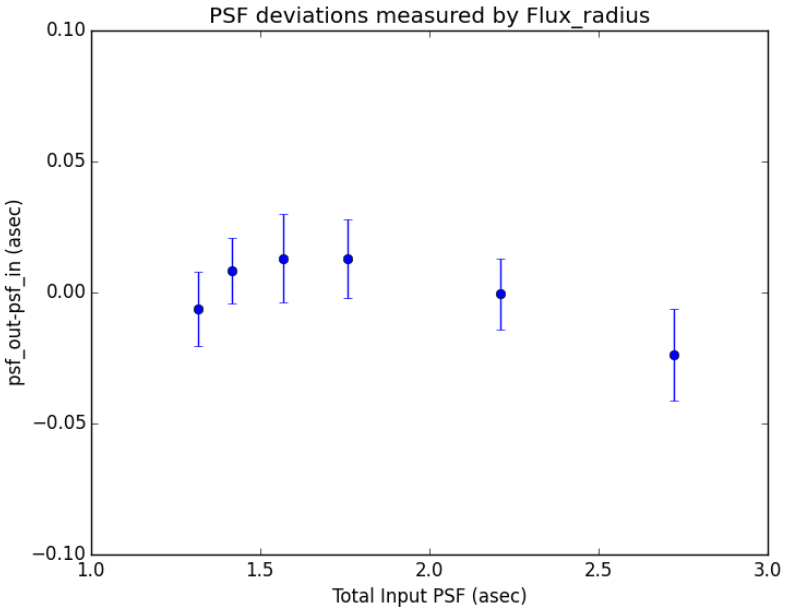

Figure 5.2: *Deviations between the measured output PSF_{out} from the Gaussian convolution and the input desired PSF_{in} for a DES tile containing RXC 2248.*

5.4.2 Limiting magnitude

When observing astrophysical sources through CCDs, the signal, S, indicates the number of photons detected from a given source. However, since the CCDs detect only a fraction of the photons, converting them to electrons (in charge units) we assume that the S is given by the electrons detected. The ratio between electrons/photons is named quantum efficiency and it ranges, typically, from $50 - 85\%$.

The Noise represents the random contribution due to several effects which impacts the Signal such as, sky noise, electrons that are coming from thermal radiation of the detector itself and read-out noise. The noise may be interpreted as the error on the flux measurement.

Thus, Signal-to-Noise ratio, thereafter SNR, is a measurement that describes the detection quality. We may define it as

$$\frac{S}{N} = \frac{\mu}{\sigma}, \tag{5.11}$$

where μ is a measurement, in our case the magnitude, and σ is its uncertainty. Eq. (5.11) consequence is that the SNR is an inverse measurement of the fractional uncertainty for a direct measurement. Thus by changing the SNR we actually change the limiting magnitude.

From the definition of magnitude m:

$$m - m_0 = -2.5 \log_{10} f, \tag{5.12}$$

where f is the flux and m_0 is the magnitude zero point, If we consider a linear relation between the Signal S in charge units and some flux units $f = C_0 S$, and also a magnitude m and its uncertainty δm have

$$m \pm \delta m = C_0 - 2.5 \log_{10} (S \pm N), \tag{5.13}$$

where $C_1 = m_0 + \log_{10} C$, from which we may derive

$$\delta m = \pm 2.5 \log_{10} \left(1 + \frac{1}{SNR}\right), \tag{5.14}$$

which may be expanded to

$$\delta m = \pm 1.0875 \left(\frac{1}{SNR} - \frac{1}{2}\left(\frac{1}{SNR}\right)^2 + \mathcal{O}(3)\right), \tag{5.15}$$

$$\delta m \approx \pm \frac{1.0875}{SNR}. \tag{5.16}$$

If one considers the image pixel values mainly as a Poissonic process, we have $SNR \approx N/\sqrt{N} = \sqrt{N}$, where N is the counts. This hypothesis indicates that we may change the limiting magnitude, or SNR by multiplying the counts, in units of electric charge, by a factor F. The relation between the original SNR_{old} and the new signal-to-noise would then be given by:

$$SNR_{new} = \sqrt{F} \times SNR_{old}. \tag{5.17}$$

The procedure to determine F and validate the results is described below:

1. We determine the original depth (i.e. limiting magnitude) of the image using a $MAG \times MAG_{ERR}$ diagram, where these quantities are taken from the SExtractor catalog. The limiting magnitude is given by the intersection of the resulting curve (binned in MAG_{ERR}) with the desired SNR (or equivalently δmag from Eq. 5.16). In Fig. 5.4(A) we show the results for

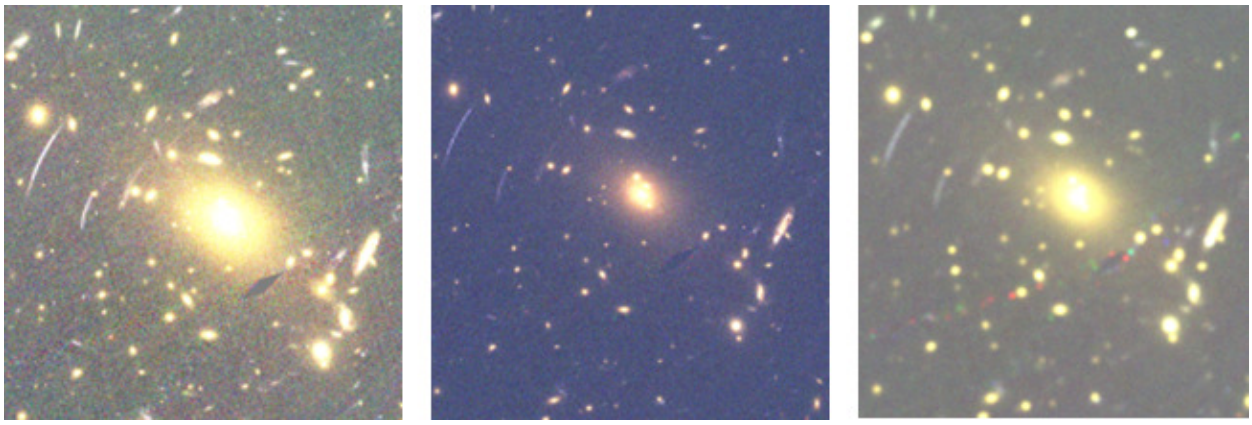

Figure 5.3: *Colour composite image of RXC J2248 from the F475W, F625W and F775W filters. Left: Original CLASH Image, with limiting magnitude* ~ 27.6 *and assumed PSF* $0.1''$*. Center: Limiting magnitude reduced to* 26*. Right: convolved with a Gaussian PSF, with FWHM*=0.9*.*

a chosen SNR = 5 (i.e. δm = 0.2175), from which we recover the original limiting magnitude of the image, $m_{\rm lim} = 27.4$.

2. To determine the factor f we use again the $MAG \times MAG_{ERR}$ diagram. Setting a new limiting magnitude $m_{\rm lim}^{\rm new}$ gives us the corresponding SNR in the original image SNR$^{\rm new}$, or equivalently, δmag$^{\rm new}$. Therefore, using Eq. (5.17), the f factor will be given by

$$F = \left(\frac{\delta{\rm mag}}{\delta{\rm mag}^{\rm new}}\right)^2 = \left(\frac{{\rm SNR}^{\rm new}}{\rm SNR}\right)^2, \tag{5.18}$$

where SNR is the significance chosen for the magnitude estimation in the original image (in this case SNR = 5).

3. Now we take the original image, in units of electric charge and with the background added (as discussed in section 5.4.1) and multiply all counts the the factor F.

4. Finally, we add back the Poisson noise to the resulting image and subtract the new background (as described in section 5.4.1). Here we assume that the Poisson noise from the original (deeper) image is significantly smaller than in the one with lower SNR, such that we sample the Poisson noise from the rescaled counts in the original image without removing its noise.

In Fig. 5.4(B) we show and example of the resulting $MAG \times MAG_{ERR}$ diagram obtained from the RXC image from CLASH following the procedure above with a chosen $m_{\rm lim}^{\rm new} = 26$. By choosing the SNR = 5 (i.e. δmag = 0.2175) we recover precisely this target magnitude.

Using the described algorithm, we were able to obtain the initial depths compatible with

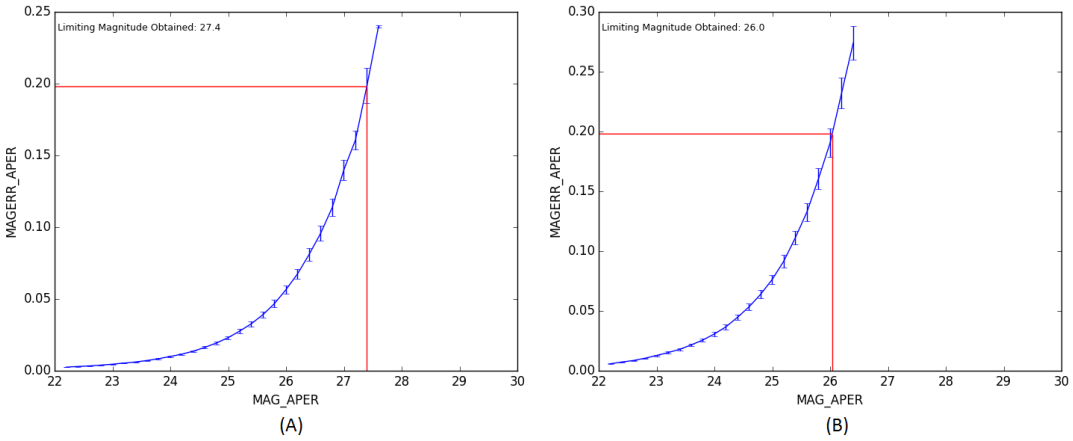

Figure 5.4: *Magnitude versus error in magnitude for RXC 2248 in a CLASH image in the F475W filter (Postman et al, 2012). Left (A): in the original image. Right (B): in the degraded image with decreased SNR. The horizontal lines are set at* $SNR = 5$*, such that the vertical lines show the limiting magnitude for this chosen SNR. Reported magnitudes are measured by SExtractor in circular apertures of* 0.4 *arcsec in diameter.*

the ones in Postman et al. (2012) within 0.1-0.2 mag and recover the target limiting magnitude within 0.1-0.2 in degraded images even without using the rms maps while measuring the original images from *SExtractor*. For the Hubble Frontier Fields data if one does not consider the rms to measure the original images the initial depths are overestimated from 0.3 to 1.0 mag, which can be fixed by using the rms maps. However, in this case the scatter in the magnitude errors are higher which affects the estimation of F and thus the target limiting magnitude recovery which deviates from $0.3 - 0.7$ from the target limiting magnitude, depending on the filter. For the model evaluation in the next sections, we considered the recovered limiting magnitude.

5.4.3 Degraded Models

We used the procedure described in the previous subsections to produce a set of degraded models from which we derive the Cosmology. To define a model in the degraded images we visually identify the multiple images on the color stacked images. It is worth noticing that, as we already know the images in the reference model this procedure represents an upper limit on the number of the multiple images that could be really found in the degraded observational conditions.

Another important point is that we only consider systems of multiple images where at

least one image has a spectroscopic redshift. This is so because it has been shown that the inclusion of systems with photo-z may make the the resulting cosmological constraints weaker (as in, e.g., Caminha et al, 2016a). In particular, the system under consideration has 15 sources with spec-z from MUSE and VIMOS from Balestra et al. (2013); Boone et al. (2013); Caminha et al. (2016a); Karman et al. (2016, 2015); Richard et al. (2014). Therefore, our systems identified in the degraded images will be a subset of this sample. As Sources with only one image, i.e. no counter image, are highly degenerate with cluster and cosmological parameters if only single image from a family (see table 5.1) still classified as visible in the degraded model we excluded it in the lens inversion. Hence, for each model, we define a group of visible images with N_v images and F_v families and a group of images which were effectively used in the lens inversion with N_{eff} images. These numbers along with a description and ID for each model are presented in table 5.2.

To determine the image positions in the reference model, we employ the procedure described in Caminha et al. (2016a), in which different iso-luminosity contours around each peak are drawn and we determine the position of the centroid of the innermost contour enclosing a few pixels. The peaks of the light distribution of different multiple images correspond to the same position on the source plane.

First, we considered how multiple images may be lost by going from FF images, where our reference model is defined with all 41 visible images, to those of CLASH. We considered a color composite of CLASH data using the following bands: F435W and F475W (for Blue), F606W, F625W, F775W, F814W, and F850W (for green) and F105W, F110W, F125W, F140W, and F160W (for red). The results from the visual inspection in CLASH are shown in table 5.2. We see that in this case 4 images are no longer visible. By just using the filters F475W, F625W and F775W which roughly correspond to the SDSS *g, r* and *i* bands (see, e.g. Abazajian et al, 2009; York et al, 2000), the effect is even more dramatic: we lose 9 images in 3 families from our reference model, particularly images that are mostly red. It is worth noticing that in a model with FF data but depth reduced below CLASH values the resulting model has more visible images and families than the CLASH model in 3 SDSS-like bands which suggests that the loss in depth should affect the models less than the loss of flux in redder bands. We considered two models with $PSF = 0.6$, one from FF (F3)

and another from with 3 filters from CLASH (C4). This PSF would be a typical value that would be achieved with good seeing from the ground, for instance, KiDS (de Jong et al, 2015, thought this is much shallower), or with LSST[3] (LSST Sci. Collaboration et al, 2009) which will reach limiting magnitude $\sim$ 27 in 10 years releases. We also considered a FF model with limiting magnitude reduced to 26.7[4], which is roughly 1 magnitude shallower than CLASH. We considered a model with 3 SDSS-like filters and with limiting magnitude[4] 26.1 and 25.0, which is feasible to a wide field survey, particularly if we consider a space-based, with PSF $\sim 0.1''$ like WFIRST (Spergel et al, 2015). In all models except for the ones with PSF degradation, the Trilogy algorithm scale was sufficient to visualize the multiple images. In the PSF degraded images the trilogy defined scales that made most of the objects very faint and it was necessary to vary the scale parameters in the DS9 visualization software[5] in order to define which multiple images are visible.

In Fig. 5.5 we present the sources and the images as function redshift for each considered model. We used bins with 0.5 width in redshift. From this figure one may infer that the models may be split in two major groups, one containing the most degraded models C3, C4 and C5 with very few sources at high redshift. C3 and C4 have 1 source in the range $[2.5, 3)$ and two in the range $[3, 3.5)$, while C5 has only one source in each of these ranges. The second group contains the less degraded models: F1, F2, F3, C1 and C2. This group has sources with redshift above 3.5 and have more sources in the range $[2.5, 3.5)$. Golse et al. (2002) and (Caminha et al, 2016a) argued that sources in higher redshifts range would be more suitable to define distance ratios that would be able to constrain Cosmological parameters.

.

5.5 Results

We explored the degraded Strong Lensing Models discussed in the previous sections focusing on their ability to constrain a flat $XCDM$ cosmological model with free Ω_m and w. We present our results for those parameters along with constraints from the combina-

[3]for further information see https://confluence.lsstcorp.org/display/LKB/LSST+Key+Numbers.

[4] We present the limiting magnitude recovered from the procedure described in 5.4.2 rather than the input limiting magnitude.

[5]For further information see *http://ds9.si.edu/site/Home.html*

Table 5.2: *Number of identified families F_v, multiple images identified N_v and number of images effectively used images in the lens inversion N_{eff} for each model of RXC J2248.7−4431.*

Model ID	Model Description	F_v	N_v	N_{eff}
F1	FF original $mag_{lim} \sim 29$	15	41	41
F2	FF $mag_{lim} = 26.7$	13	33	33
F3	FF - $PSF = 0.6''$	13	34	32[a]
C1	CLASH original $mag_{lim} \sim 27.6$	13	37	36
C2	CLASH 3 filters	12	32	31
C3	CLASH 3 filters - $mag_{lim} = 26.1$	9	26	24
C4	CLASH 3 filters - $PSF = 0.6''$	9	25	22
C5	CLASH 3 filters - $mag_{lim} = 25$	7	18	17

[a]The family 28 was visible with only two multiple images and the model had difficulties to converge. Thus we have removed this family in this case.

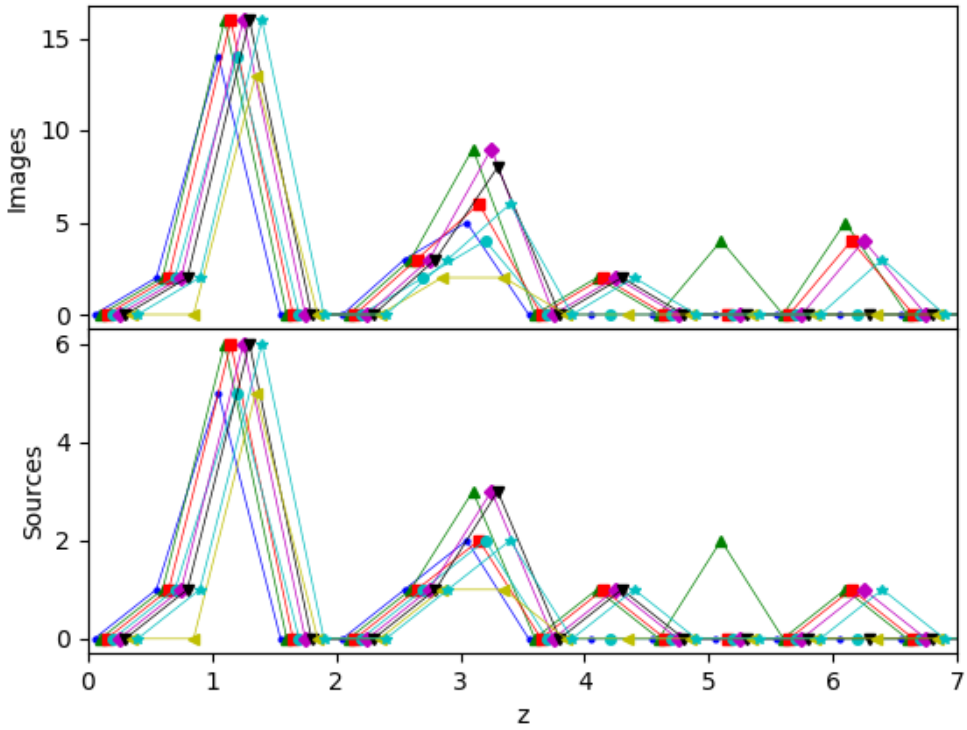

Figure 5.5: *Number of Images (top) and Sources (bottom) as a function of the source redshift for each model: FF (F1, green), FF with limiting magnitude 26.7 (F2, red), FF with $PSF = 0.6''$ (F3, $\star$ in cyan), CLASH (C1, magenta), CLASH with 3 filters (C2, black), CLASH with 3 filters and with limiting magnitude 26.1 (C3, blue), CLASH with 3 filters and with $PSF = 0.6''$ (C4, cyan) and CLASH with 3 filters and with limiting magnitude* 25.0 *(C5, yellow). The points were shifted horizontally for clarity.*

tion with Planck data (Planck Collaboration et al, 2014) in table (5.3). The Planck data used is a combination of Planck temperature power spectrum with a WMAP polarization low-multipole likelihood. It is worth noticing that all Strong Lensing only results pre-

sented, except for CLASH with limiting magnitude 25, agree within 1σ with the combination of Planck[6] with cosmic shear (i.e., Weak Lensing) data, Baryon Acoustic Oscillations (BAO), type Ia Supernova values, which yields $\Omega_m = 0.3089 \pm 0.0062$ and $w = -1.019^{+0.075}_{-0.080}$ (Planck Collaboration et al, 2016). The confidence contours and PDFs for Ω_m and w for each model are presented in Figs. 5.6 to 5.13.

An interesting feature concerning the contours in the $\Omega_m \times w$ plane is that the Strong Lensing data is complementary to the one from CMB, and its overall shape remains qualitatively the same for all models with the exception of C4 and C5, which are the most degraded[7]. We also noticed that the confidence contours are qualitatively comparable to a similar Strong Lensing analysis in Abell 1689 by Jullo et al. (2010). From the plots, we see that the best-fit to the combined data (SL+Planck) in the Ω_m x w plane is shifted to the border of the 1σ Planck contours. This is so for all models from the less degraded ones (F1, F2, F3, C1, C2) and two in the more degraded ones (C3 and C4), indicating that this result is robust, even with the loss of $\sim 40\%$ of the image families.

From table 5.3 we notice that although the Strong Lensing constraints are very degenerate in the lower limit of w they may constrain its upper limit with error bar comparable to the Planck one with a single cluster and even with shallow images with depth reduced to 26.7 if one considers a coadd of several bands, including the redder ones. It is also worth noticing that the stringent upper limits on w were first obtained in this work. This is due to the new set of images that we employ for constraining cosmology for the first time. A previous work concerning the CLASH+VIMOS and MUSE data from Caminha et al. (2016b) obtained $\Omega_m = 0.25^{0.11}_{-0.14}$ and $w = -1.20^{+0.25}_{-0.47}$ for a model with spectroscopically confirmed families only. This previous result is comparable to models of the less degraded group F1, F2, F3, C2 and particularly C1, which represents what can be seen with CLASH. On the other hand, in that paper, the lower limit of w is much better constrained than in the present results. We believe that this lower limit might be dominated by the prior in w, as Caminha et al. (2016b) use a flat prior ranging from 0 to -2.

There is a major difference between the two groups, the less degraded in comparison to

[6]For further details see table 4 and 5 in Planck Collaboration et al. (2016)

[7]Despite of the fact that their uncertainty regions are larger when the models are more degraded.

the more degraded, which confirms the expectation that to obtain better constraints it is important to have high redshift sources. Despite of the bias in C3 and C4 when considering Strong Lensing only, we may note that the results for the analyses are still consistent in 1σ with those from F1, the reference model, with very similar error bars to C2, which suggests that the observational effects may increase the bias but not change much the error bars. The most significant change in error bars from one model to the next one with fewer constraints was in the Ω_m from C1 to C2, in which the upper error has doubled suggesting that the loss of the readder images when changing from CLASH with 12 bands to CLASH with 3 bands are more important than the change in depth.

Table 5.3: *Cosmological parameters Ω_m and w for the Strong Lensing analysis for each model of RXC J2248.7−4431 and the results for Strong Lensing in combination with Planck data. The errors represent 1σ confidence levels.*

Model	Ω_m	w	Ω_m (SL+Planck)	w (SL+Planck)
Planck Only	$0.16^{+0.10}_{-0.02}$	$-1.67^{+0.48}_{-0.16}$		
F1	$0.36^{+0.08}_{-0.16}$	$-1.03^{+0.05}_{-1.99}$	$0.28^{+0.02}_{-0.05}$	$-1.14^{+0.05}_{-0.27}$
F2	$0.34^{+0.10}_{-0.14}$	$-1.03^{+0.16}_{-2.20}$	$0.24^{+0.02}_{-0.08}$	$-1.24^{+0.05}_{-0.38}$
F3	$0.36^{+0.14}_{-0.16}$	$-1.03^{+0.05}_{-2.20}$	$0.24^{+0.04}_{-0.08}$	$-1.14^{+0.05}_{-0.48}$
C1	$0.34^{+0.10}_{-0.14}$	$-1.03^{+0.05}_{-2.31}$	$0.24^{+0.04}_{-0.04}$	$-1.24^{+0.05}_{-0.27}$
C2	$0.34^{+0.26}_{-0.10}$	$-1.14^{+0.05}_{-2.20}$	$0.24^{+0.04}_{-0.04}$	$-1.24^{+0.16}_{-0.27}$
C3	$0.48^{+0.28}_{-0.20}$	$-0.92^{+0.05}_{-2.52}$	$0.28^{+0.04}_{-0.08}$	$-1.14^{+0.16}_{-0.37}$
C4	$0.52^{+0.26}_{-0.23}$	$-0.92^{+0.16}_{-2.42}$	$0.24^{+0.04}_{-0.04}$	$-1.24^{+0.16}_{-0.27}$
C5	$0.24^{+0.44}_{-0.08}$	$-1.24^{+0.16}_{-2.20}$	$0.18^{+0.04}_{-0.04}$	$-1.57^{+0.27}_{-0.27}$

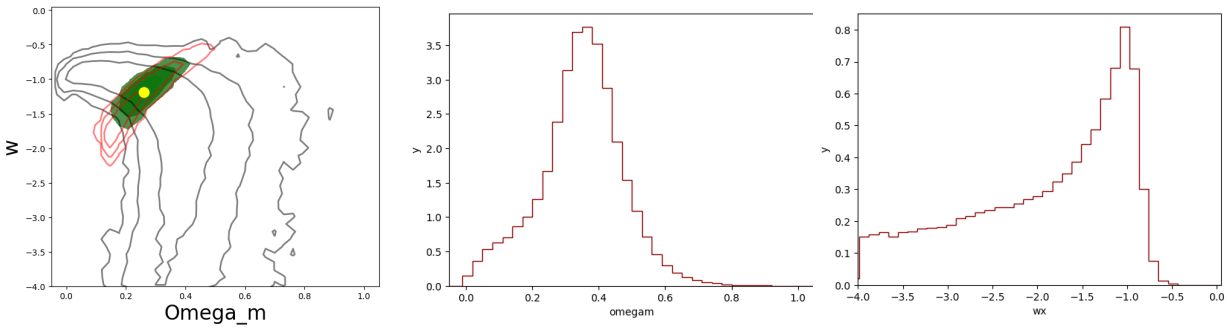

(a) $\Omega_m \times w$ *contours* **(b)** Ω_m **(c)** w

Figure 5.6: *Model F1: all visible multiple images in Frontiers Field. Panel (a): Confidence levels for the cosmological parameters with Strong Lensing (Black Lines), Planck Data Release 2 data (red contours) and the combined constraints (green regions). The yellow circles indicate the maximum likelihood peak from SL+Planck in this projection. Panel (b): PDF for Ω_m in the Strong Lensing Model and (c): PDF for w in the Strong Lensing Mode.*

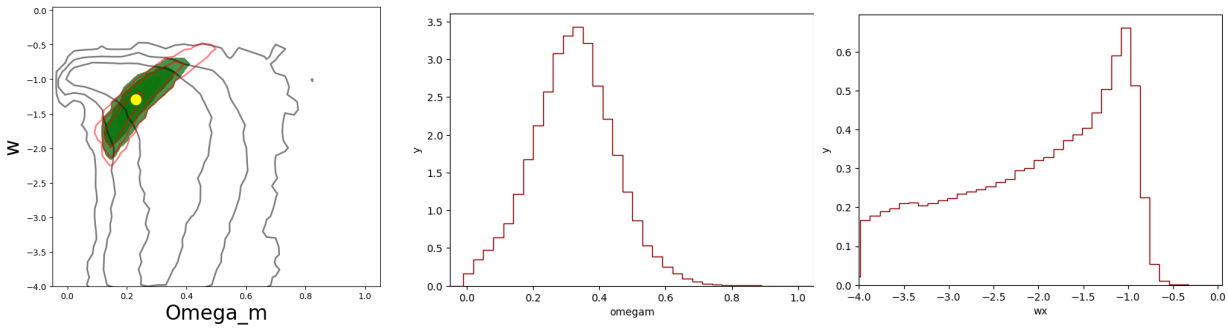

(a) $\Omega_m \times w$ *contours* **(b)** Ω_m **(c)** w

Figure 5.7: *Model F2: all visible multiple images in Frontiers Field images with limiting magnitude* 26.7. *Panel (a): Confidence levels for the cosmological parameters with Strong Lensing (Black Lines), Planck Data Release 2 data (red contours) and the combined constraints (green regions). The yellow circles indicate the maximum likelihood peak from SL+Planck in this projection. Panel (b): PDF for* Ω_m *in the Strong Lensing Model and (c): PDF for* w *in the Strong Lensing Mode.*

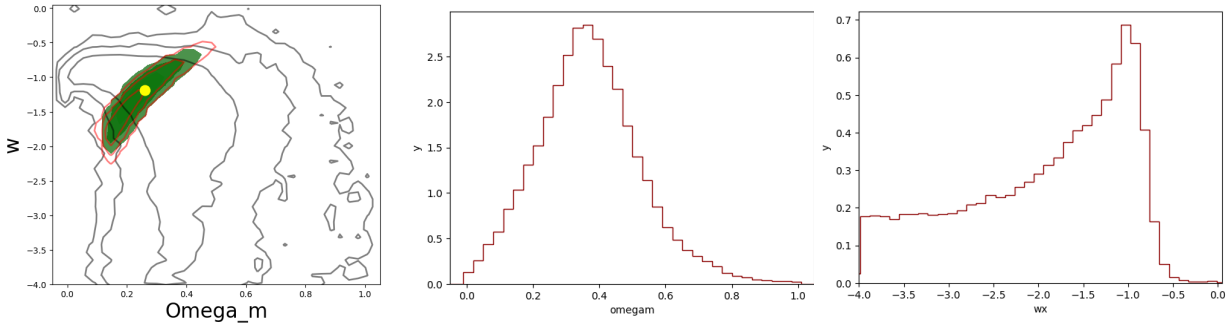

(a) $\Omega_m \times w$ *contours* **(b)** Ω_m **(c)** w

Figure 5.8: *Model F3: all visible multiple images in Frontiers Field images with PSF* $= 0.6''$. *Panel (a): Confidence levels for the cosmological parameters with Strong Lensing (Black Lines), Planck Data Release 2 data (red contours) and the combined constraints (green regions). The yellow circles indicate the maximum likelihood peak from SL+Planck in this projection. Panel (b): PDF for* Ω_m *in the Strong Lensing Model and (c): PDF for* w *in the Strong Lensing Mode.*

5.6 Discussion

In this chapter, we evaluated the cosmological constraints arising from Cluster Strong Lensing in a flat $XCDM$ model for different degraded models of RXC 2248, which exploited the dependency of the cosmological constraints on the observing conditions. We considered how the constraints were biased due to the degradation in combination with Planck data release 2 in order to evaluate if those constraints are robust and if it would be feasible to derive cosmological constraints with limited observational conditions such as PSF and depths compatible with ground-based data, such as LSST and/or future space-based wide field surveys such as WFIRST and Euclid. We also exploit models using fewer bands. We derived the cosmological constraints for a set of families of multiple images which were

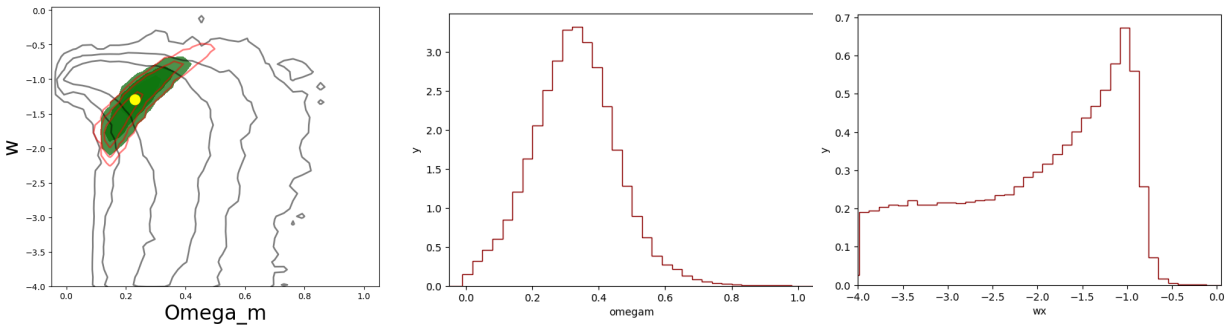

(a) $\Omega_m \times w$ *contours* **(b)** Ω_m **(c)** w

Figure 5.9: *Model C1: with all visible multiple images in CLASH model. Panel (a): Confidence levels for the cosmological parameters with Strong Lensing (Black Lines), Planck Data Release 2 data (red contours) and the combined constraints (green regions). The yellow circles indicate the maximum likelihood peak from SL+Planck in this projection. Panel (b): PDF for* Ω_m *in the Strong Lensing Model and (c): PDF for* w *in the Strong Lensing Mode.*

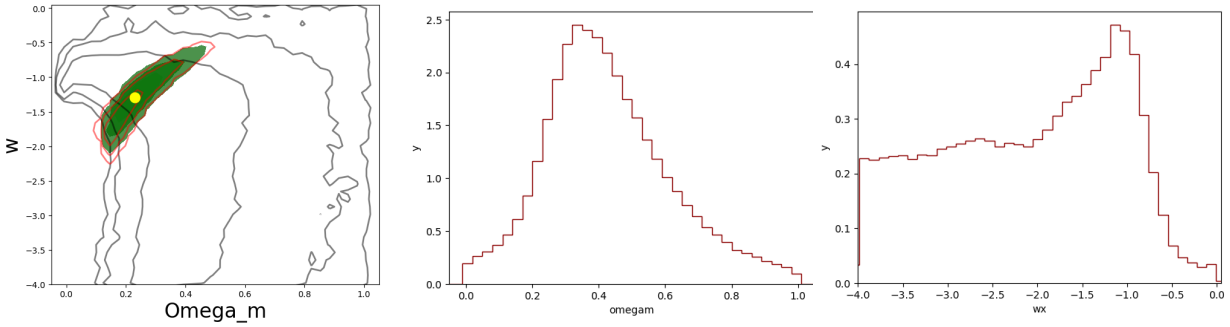

(a) $\Omega_m \times w$ *contours* **(b)** Ω_m **(c)** w

Figure 5.10: *Model C2: all visible multiple images in CLASH images using* 3 *sdss-like filters only: F475W, F625W and F775W. Panel (a): Confidence levels for the cosmological parameters with Strong Lensing (Black Lines), Planck Data Release 2 data (red contours) and the combined constraints (green regions). The yellow circles indicate the maximum likelihood peak from SL+Planck in this projection. Panel (b): PDF for* Ω_m *in the Strong Lensing Model and (c): PDF for* w *in the Strong Lensing Mode.*

spectroscopically confirmed. A sample with well defined redshifts is important to derive the cosmography since redshifts are highly degenerate with the Cosmological parameters. We reported that the best fit in the Ω_m x w plane remains robust in several models in combination with Planck data, changing the Planck best fit to the 1σ Planck contours borders. This result remains robust even with depth reduction from $\sim$ 29 in the reference model to 26.1 with 3 bands only. A depth that would be feasible in a wide field survey, particularly space-based with low PSF, in which it would be possible to combine the analysis of several Clusters.

In a previous analysis of RJC 2248, Caminha et al. (2016b) also highlighted the importance to use a wide range of source redshifts, as also pointed out by Golse et al. (2002). For

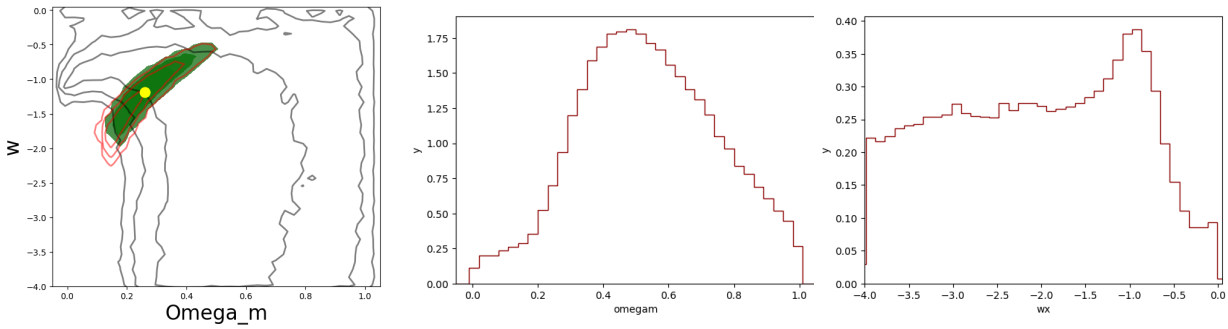

(a) $\Omega_m \times w$ *contours* **(b)** Ω_m **(c)** w

Figure 5.11: *Model C3: all visible multiple images in CLASH images using* 3 *earth-like filters only: F475W, F625W and F775W and with limiting magnitude* 26.1. *Panel (a): Confidence levels for the cosmological parameters with Strong Lensing (Black Lines), Planck Data Release 2 data (red contours) and the combined constraints (green regions). The yellow circles indicate the maximum likelihood peak from SL+Planck in this projection. Panel (b): PDF for* Ω_m *in the Strong Lensing Model and (c): PDF for* w *in the Strong Lensing Mode.*

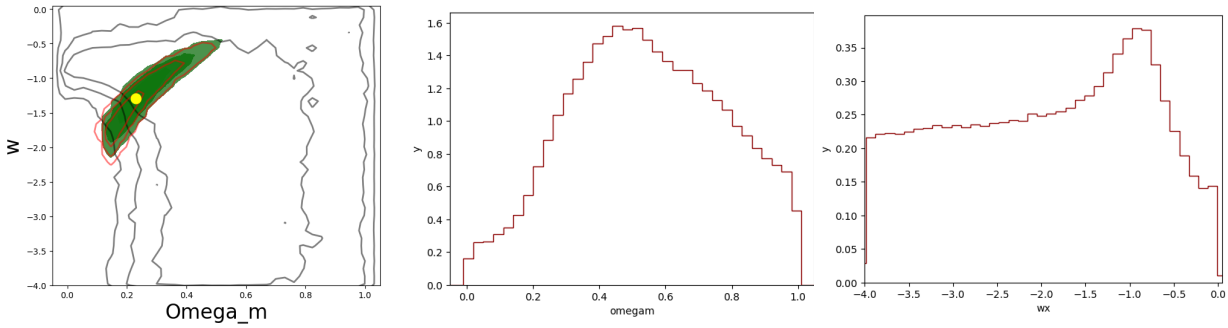

(a) $\Omega_m \times w$ *contours* **(b)** Ω_m **(c)** w

Figure 5.12: *Model C4: all visible multiple images in CLASH model using* 3 *earth-like filters only: F475W, F625W and F775W with PSF=*0.6″. *Panel (a): Confidence levels for the cosmological parameters with Strong Lensing (Black Lines), Planck Data Release 2 data (red contours) and the combined constraints (green regions). The yellow circles indicate the maximum likelihood peak from SL+Planck in this projection. Panel (b): PDF for* Ω_m *in the Strong Lensing Model and (c): PDF for* w *in the Strong Lensing Mode.*

illustration purposes, Caminha et al. (2016b) derived cosmological constraints without the highest redshift source ($z = 6.11$). They obtained $\Omega_m = 0.49^{+0.26}_{-0.26}$ and $w = 1.07^{+0.42}_{0.57}$ which roughly represents an increase of $\sim 50\%$ in the errors of the Cosmological parameters. In this work, we considered a set that included 6 sources identified by Karman et al. (2016) not considered for Cosmological constraints previously. We noticed that the error in the upper limit of Ω_m has increased to the value close to the one in C2 (degraded to CLASH data in 3 bands) model, which has no sources with redshift higher than $z = 4.11$ (i.e., family 18 already included in Caminha et al, 2016b). However, the extra families added in this model (23, 24, 27 and 28) appear to keep the lower limit of Ω_m comparable to the model which includes

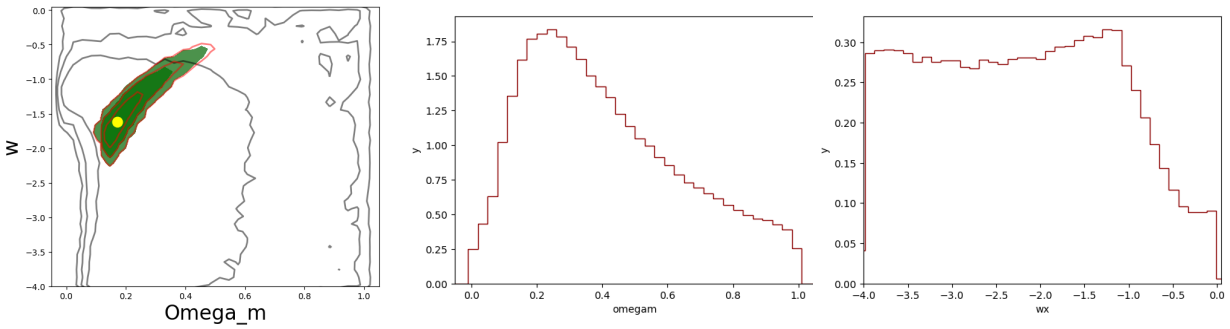

(a) $\Omega_m \times w$ *contours* **(b)** Ω_m **(c)** w

Figure 5.13: *Model C5: all visible multiple images in CLASH images using* 3 *earth-like filters only: F475W, F625W and F775W with limiting magnitude reduced to* 25.0*. Panel (a): Confidence levels for the cosmological parameters with Strong Lensing (Black Lines), Planck Data Release 2 data (red contours) and the combined constraints (green regions). The yellow circles indicate the maximum likelihood peak from SL+Planck in this projection. Panel (b): PDF for* Ω_m *in the Strong Lensing Model and (c): PDF for* w *in the Strong Lensing Mode.*

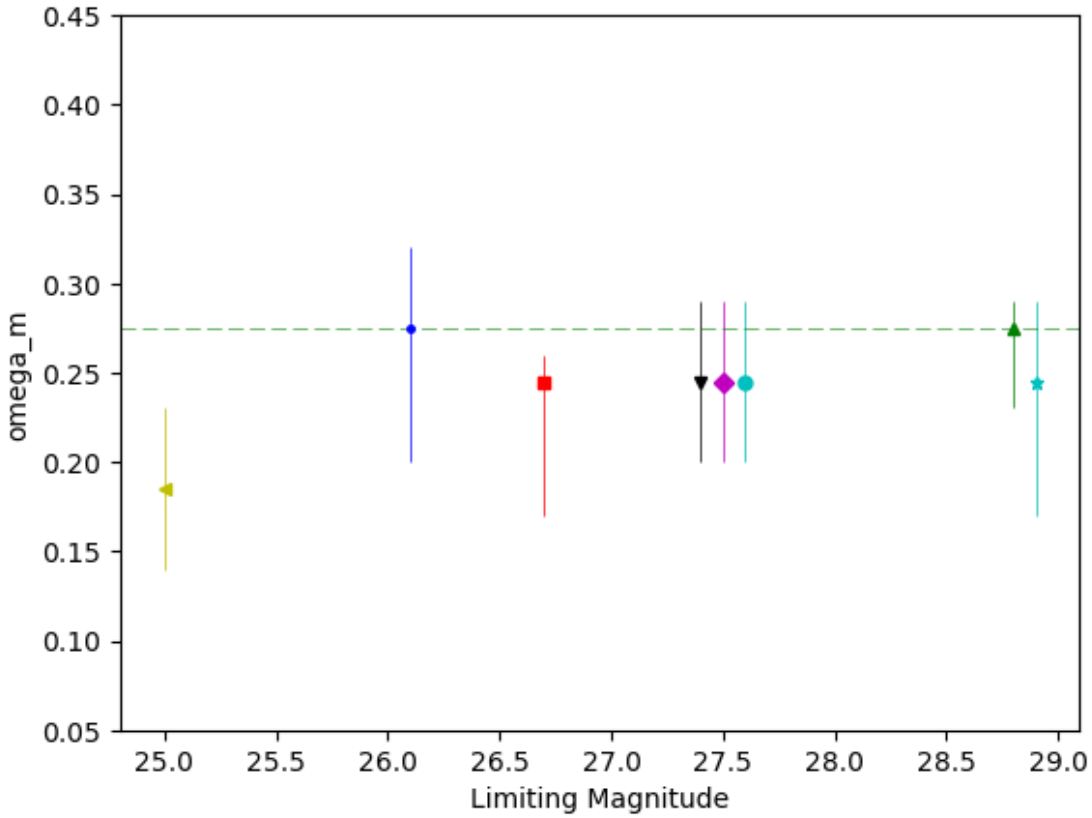

Figure 5.14: Ω_m *and its* 1σ *error bars as a function of the limiting magnitude for each model. From right to left: FF with* $PSF = 0.6''$ *(F3, in cyan), original FF (F1, green), CLASH with 3 filters and with PSF=* $0.6''$ *(C4, cyan), CLASH (C1, magenta), CLASH with 3 filters (C2, black), FF with limiting magnitude 26.7 (F2, red), CLASH with 3 filters and with limiting magnitude 26.1 (C3, blue), CLASH with 3 filters and with limiting magnitude* 25.0 *(C5, yellow). The green line presents the value of* Ω_m *for the reference model (F1). The points were shifted horizontally for clarity.*

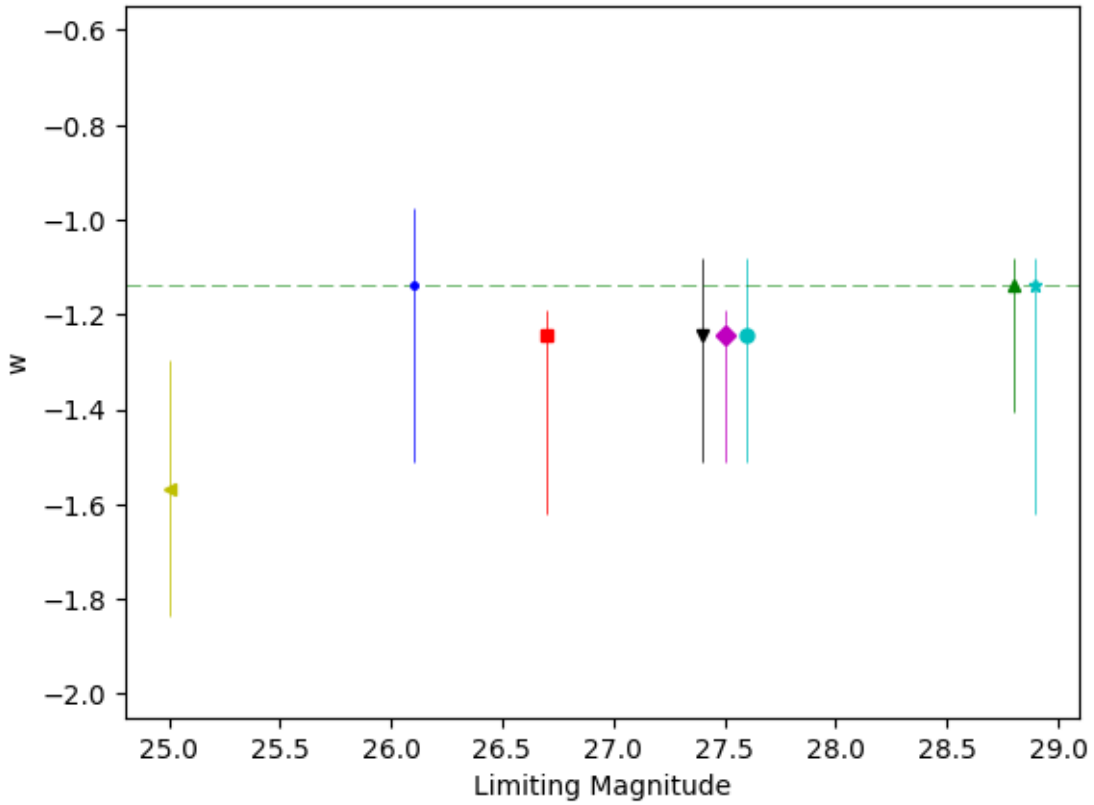

Figure 5.15: *w and its 1σ error bars as a function of the limiting magnitude for each model for each model. From right to left: FF with $PSF = 0.6''$ (F3, in cyan), original FF (F1, green), CLASH with 3 filters and with $PSF = 0.6''$ (C4, cyan), CLASH (C1, magenta), CLASH with 3 filters (C2, black), FF with limiting magnitude 26.7 (F2, red), CLASH with 3 filters and with limiting magnitude 26.1 (C3, blue), CLASH with 3 filters and with limiting magnitude* 25.0 *(C5, yellow). The green line presents the value of w for the reference model (F1). The points were shifted horizontally for clarity.*

the high redshifts sources though shifting the range of Ω_m to upper values. The lower limit range of w is about half if one compares to the similar model with all spectroscopic families in Caminha et al. (2016b), which includes the $z = 6.111$ redshift. These results suggest that the increase in the uncertainties due to removal of a high redshifts source, i. e. $z \sim 6$, may be compensated by adding more constraints in low/intermediate redshifts.

Now we look into our results to have a first glance on the issue of constraining cosmological parameters with strong lensing in the upcoming wide-field survey data. Given that we expect several systems with multiple families of multiple images to be found on that data, will the statistics be able to overcome the effects of the worse PSF and/or depth compared to the Frontier Fields data? Are there systematic errors arising from the degraded data that will not go away by averaging several systems? What is the number of systems needed so that

the error bars on the parameters get down to the Frontier Fields ones? To touch upon these questions, let's look at Figs. 5.14 and 5.15, where we summarize the constraints on Ω_m and w derived from the models considered in this work. We see that in all cases but the most degraded one (C5), the biases are quite small (at most about 0.1 in w and 0.03 in Ω_m). Nevertheless, these biases are already significant for CLASH (C1) and shallower FF (F2), as they show stringent upper limits on the two parameters. In general, the error bars do not change much for the cases we have considered. The largest effect is on the upper level of w and Ω_m, which is significantly increased in the CLASH models with 3 filters (C2, C3, and C4). To have a rough estimate on how the statistical error bars will change as we consider the combination of several clusters, we assume that the fractional errors will scale as $\delta\Omega_m/\Omega_m \propto 1/\sqrt{N}$. For example, let's consider the variation on the upper error bar on Ω_m from models F1 to C4: $\delta\Omega_m^{C4+}/\delta\Omega_m^{F1+} \approx 3$. In this case, employing the assumed scaling of the error bars, one would expect that by using about 10 clusters under the C4 conditions, the error bars would shrink to the values obtained with the full FF data. In this case, of course, the bias would start being significant. Clearly, the arguments above are very rough and a systematic study with more observational conditions and, especially, with more systems (either from simulations or data) is needed for a more quantitative assessment. This is an avenue we will pursue the continuation of this work.

Chapter 6

Concluding Remarks and Perspectives

In this thesis, we address several aspects of the Strong Gravitational Lensing program, from finding lens systems to using multiple images to constrain cosmological parameters. In section 3 propose a new method to make measurements in gravitational arcs, and particularly, how to estimate their curvature. These developments are presented in two articles: one submitted to Astronomy and Astrophysics and the other a CBPF technical note (Bom et al, 2016a).

The Mediatrix decomposition and its measurements were applied to the recovery of arc features, in simulated and real arcs in Furlanetto et al. (2013b), on which I am a co-author. This method is presently being applied by myself and collaborators to characterize arc candidates and estimates Einstein radii in the SOAR (Southern Astrophysical Research) Gravitational Arc Survey (SOGRAS Furlanetto et al, 2013a). We expect to submit this paper on SOGRAS data on this semester.

In section 4 we discuss how to find Strong Lenses. We present three approaches, a standard visual inspection in which the author took part (Nord et al, 2015), a Pattern Recognition automated algorithm, named ANN Mediatrix Arcfinder (AMA) and a Deep Learning pipeline with which we have participated in the Gravitational Lensing Challenge. Presently a paper is being prepared in which the results in the Challenge will be presented. The AMA algorithm was fully described in an article recently published in A&A (Bom et al, 2017). More recently, the author and collaborators worked on an optimization of SExtractor based in Genetic Algorithms, named GOSEx (Genetic Optimization in SExtractor), which may

improve significantly the deblending and therefore, the results in the arcfinder and the morphology measurements.We plan to further develop the AMA arcfinder, both implementing a cleaning of the image using SExtractor model fitting options as well as training in a sample of real cluster scale arcs, for instance in CFHTLS. We also plan to improve the CNN Lens finder and apply it in wide-field surveys in targeted searches for galaxy scale lensing.

In the last part of this thesis, we discuss how observational effects such as the PSF and image depth may affect the constraints from multiple image cosmography to have a glance on how they can bias the cosmological parameters from ground-based observations and for present and future wide-field surveys (both space or ground based). To the best of our knowledge, this has never been tested, although recent works have addressed other systematics, such as those arising from substructure, structure along the line of sight (LOS) or lens modelling codes (Despali & Vegetti, 2016; Gilman et al, 2016; Meneghetti et al, 2016; Planck Collaboration et al, 2016; Priewe et al, 2016). Even in these cases, the authors are concerned with the accuracy, precision, and reliability in the mass distribution constraints and do not focus on the cosmological constraints. We combined our results with Planck data and derived the constraints on the cosmological parameters. The results were robust in several degraded models when defining an upper limit to w. In combination with Planck, the results improved the Planck constraints in all degraded models except to the one with limiting magnitude 25 (the one with fewer images). We are currently preparing a paper with the summary of our tests and discussion in section 5.6 and plan to submit it a near future. In a future work, I also plan to develop simulations to explore what cosmological constraints would be feasible to derive with the emerging astronomical technologies such as the MKIDs (Day et al, 2003) detector that would enable us to have a low resolution redshift for every imaged source.

Therefore, in this thesis we covered several fields, from image processing and pattern recognition to the final proposed goal, which are the cosmological constraints from multiple image Strong Lensing analyses as a cosmological probe. Particularly we evaluate the feasibility to derive the constraints in conditions similar to future wide-field surveys that will provide many systems of multiple image Strong Lensing, which, when combined, might be used as a powerful cosmological probe.

Bibliography

Abazajian, K. N., Adelman-McCarthy, J. K., Agüeros, M. A., et al. 2009, The Astrophysical Journal Supplement Series, 182, 543

Abdelsalam, H. M., Saha, P., & Williams, L. L. R. 1998, MNRAS, 294, 734

Abell, G. O., Corwin, Jr., H. G., & Olowin, R. P. 1989, ApJS, 70, 1

Alard, C. 2006, arXiv:astro-ph/0606757

Bacon, R., Accardo, M., Adjali, L., et al. 2010, in Proc. SPIE, Vol. 7735, Ground-based and Airborne Instrumentation for Astronomy III, 773508

Balestra, I., Vanzella, E., Rosati, P., et al. 2013, A&A, 559, L9

Barden, M., Häußler, B., Peng, C. Y., McIntosh, D. H., & Guo, Y. 2012, MNRAS, 422, 449

Bartelmann, M., Huss, A., Colberg, J. M., Jenkins, A., & Pearce, F. R. 1998, A&A, 330, 1

Bayliss, M. B. 2012, ApJ, 744, 156

Beckwith, S. V. W., Stiavelli, M., Koekemoer, A. M., et al. 2006, AJ, 132, 1729

Belokurov, V., Evans, N. W., Hewett, P. C., et al. 2009, MNRAS, 392, 104

Benitez, N., Dupke, R., Moles, M., et al. 2014, arXiv:1403.5237

Bergé, J., Gamper, L., Réfrégier, A., & Amara, A. 2013, Astronomy and Computing, 1, 23

Bertin, E. 2009, Mem. Soc. Astron. Italiana, 80, 422

Bertin, E. & Arnouts, S. 1996, A&AS, 117, 393

Bleem, L. E., Stalder, B., de Haan, T., et al. 2015, ApJS, 216, 27

Blum, R. D., Burleigh, K., Dey, A., et al. 2016, in American Astronomical Society Meeting Abstracts, Vol. 228, American Astronomical Society Meeting Abstracts, 317.01

Bolton, A. S., Burles, S., Koopmans, L. V. E., Treu, T., & Moustakas, L. A. 2006, ApJ, 638, 703

Bom, C. R., Furlanetto, C., More, A., et al. 2015, in Thirteenth Marcel Grossmann Meeting: On Recent Developments in Theoretical and Experimental General Relativity, Astrophysics and Relativistic Field Theories, ed. K. Rosquist, 2088–2090

Bom, C. R., Makler, M., & Albuquerque, M. P. 2016a, CBPF Technical Notes

Bom, C. R., Makler, M., Albuquerque, M. P., & Brandt, C. H. 2017, A&A, 597, A135

Bom, C. R., Makler, M., Albuquerque, M. P., Brandt, C. H., & Ferreira, P. C. 2016b, A&A, submitted

Boone, F., Clément, B., Richard, J., et al. 2013, A&A, 559, L1

Bradač, M., Treu, T., Applegate, D., et al. 2009, ApJ, 706, 1201

Brault, F. & Gavazzi, R. 2015, A&A, 577, A85

Brownstein, J. R., Bolton, A. S., Schlegel, D. J., et al. 2012, ApJ, 744, 41

Cabanac, R. A., Alard, C., Dantel-Fort, M., et al. 2007, A&A, 461, 813

Caminha, G. B., Estrada, J., & Makler, M. 2013, arXiv:1308.6569

Caminha, G. B., Grillo, C., Rosati, P., et al. 2016a, A&A, 587, A80

Caminha, G. B., Grillo, C., Rosati, P., et al. 2016b, A&A, 587, A80

Cao, S., Biesiada, M., Gavazzi, R., Piórkowska, A., & Zhu, Z.-H. 2015, The Astrophysical Journal, 806, 185

Carrasco, E. R., Gomez, P. L., Verdugo, T., et al. 2010, ApJ, 715, L160

Coe, D., Benítez, N., Broadhurst, T., & Moustakas, L. A. 2010, ApJ, 723, 1678

Coe, D., Benítez, N., Sánchez, S. F., et al. 2006, AJ, 132, 926

Coe, D., Fuselier, E., Benítez, N., et al. 2008, ApJ, 681, 814

Coe, D., Umetsu, K., Zitrin, A., et al. 2012, ApJ, 757, 22

Collett, T. E. 2015, ApJ, 811, 20

Cooray, A. R. 1999, A&A, 341, 653

Cruddace, R., Voges, W., Böhringer, H., et al. 2002, ApJS, 140, 239

Dark Energy Survey Collaboration, Abbott, T., Abdalla, F. B., et al. 2016, arXiv:1601.00329

Day, P. K., LeDuc, H. G., Mazin, B. A., Vayonakis, A., & Zmuidzinas, J. 2003, Nature, 425, 817

de Jong, J. T. A., Verdoes Kleijn, G. A., Boxhoorn, D. R., et al. 2015, A&A, 582, A62

Desai, S., Armstrong, R., Mohr, J. J., et al. 2012, ApJ, 757, 83

Despali, G. & Vegetti, S. 2016, arXiv: 1608.06938

Diego, J. M., Protopapas, P., Sandvik, H. B., & Tegmark, M. 2005, MNRAS, 360, 477

Dressler, A., Bigelow, B., Hare, T., et al. 2011, PASP, 123, 288

Durret, F., Adami, C., Bertin, E., et al. 2015, A&A, 578, A79

Dyson, F. W., Eddington, A. S., & Davidson, C. 1920, Philosophical Transactions of the Royal Society of London Series A, 220, 291

Elíasdóttir, Á., Limousin, M., Richard, J., et al. 2007, arXiv:0710.5636

Enander, J. & Mörtsell, E. 2013, Journal of High Energy Physics, 2013, 1

Estrada, J., Annis, J., Diehl, H. T., et al. 2007, ApJ, 660, 1176

Fassnacht, C. D., Moustakas, L. A., Casertano, S., et al. 2004, ApJ, 600, L155

Faure, C., Kneib, J.-P., Covone, G., et al. 2008, ApJS, 176, 19, erratum 2008, 178, 382

Furlanetto, C., Santiago, B. X., Makler, M., et al. 2013a, MNRAS, 432, 73

Furlanetto, C., Santiago, B. X., Makler, M., et al. 2013b, A&A, 549, A80

Gao, L., Navarro, J. F., Cole, S., et al. 2008, MNRAS, 387, 536

Gavazzi, R., Marshall, P. J., Treu, T., & Sonnenfeld, A. 2014, ApJ, 785, 144

Gilman, D., Agnello, A., Treu, T., Keeton, C. R., & Nierenberg, A. M. 2016, arXiv:1610.08525

Gladders, M. D., Hoekstra, H., Yee, H. K. C., Hall, P. B., & Barrientos, L. F. 2003, ApJ, 593, 48

Golse, G., Kneib, J.-P., & Soucail, G. 2002, A&A, 387, 788

Gómez, P. L., Valkonen, L. E., Romer, A. K., et al. 2012, AJ, 144, 79

Goobar, A., Amanullah, R., Kulkarni, S. R., et al. 2016, arXiv:1611.00014

Grillo, C., Suyu, S., Rosati, P., et al. 2015, The Astrophysical Journal, 800, 38

Grillo, C., Suyu, S. H., Rosati, P., et al. 2015, ApJ, 800, 38

Gruen, D., Brimioulle, F., Seitz, S., et al. 2013, MNRAS, 432, 1455

Hála, P. 2014, ArXiv e-prints

Halkola, A., Hildebrandt, H., Schrabback, T., et al. 2008, A&A, 481, 65

Halkola, A., Seitz, S., & Pannella, M. 2006, MNRAS, 372, 1425

Hennawi, J. F., Gladders, M. D., Oguri, M., et al. 2008, AJ, 135, 664

Hogg, D. W., Blandford, R., Kundic, T., Fassnacht, C. D., & Malhotra, S. 1996, ApJ, 467, L73

Hook, I. M., Jørgensen, I., Allington-Smith, J. R., et al. 2004, PASP, 116, 425

Horesh, A., Maoz, D., Ebeling, H., Seidel, G., & Bartelmann, M. 2010, MNRAS, 406, 1318

Horesh, A., Maoz, D., Hilbert, S., & Bartelmann, M. 2011, MNRAS, 418, 54

Horesh, A., Ofek, E. O., Maoz, D., et al. 2005, ApJ, 633, 768

Hoyle, B. 2016, Astronomy and Computing, 16, 34

Huertas-Company, M., Gravet, R., Cabrera-Vives, G., et al. 2015, The Astrophysical Journal Supplement Series, 221, 8

Jackson, N. 2008, MNRAS, 389, 1311

Jaki, S. L. 1978, Foundations of Physics, 8, 927

Jiménez-Teja, Y. & Benítez, N. 2012, ApJ, 745, 150

Johnson, T. L., Sharon, K., Bayliss, M. B., et al. 2014, ApJ, 797, 48

Jones, T. A., Swinbank, A. M., Ellis, R. S., Richard, J., & Stark, D. P. 2010, MNRAS, 404, 1247

Joseph, R., Courbin, F., Metcalf, R. B., et al. 2014, A&A, 566, A63

Jullo, E., Kneib, J.-P., Limousin, M., et al. 2007, New Journal of Physics, 9, 447

Jullo, E., Natarajan, P., Kneib, J.-P., et al. 2010, Science, 329, 924

Karman, W., Caputi, K. I., Caminha, G. B., et al. 2016, arXiv:1606.01471

Karman, W., Caputi, K. I., Grillo, C., et al. 2015, A&A, 574, A11

Kassiola, A. & Kovner, I. 1993, ApJ, 417, 450

Kausch, W., Schindler, S., Erben, T., Wambsganss, J., & Schwope, A. 2010, A&A, 513, A8

Keeton, C. & Kochanek, C. 1998, The Astrophysical Journal, 495, 157

Keeton, C. R. 2001, arXiv:astro-ph/0102340

Kelly, P. L., Rodney, S. A., Treu, T., et al. 2015, Science, 347, 1123

Kneib, J.-P., Ellis, R. S., Smail, I., Couch, W. J., & Sharples, R. M. 1996, The Astrophysical Journal, 471, 643

Komatsu, E., Dunkley, J., Nolta, M. R., et al. 2009, ApJS, 180, 330

Komatsu, E., Smith, K. M., Dunkley, J., et al. 2011, ApJS, 192, 18

Koopmans, L. V. E., Treu, T., Bolton, A. S., Burles, S., & Moustakas, L. A. 2006, ApJ, 649, 599

Kovner, I. 1989, ApJ, 337, 621

Krizhevsky, A., Sutskever, I., & Hinton, G. E. 2012, in Advances in neural information processing systems, 1097–1105

Kubo, J. M., Allam, S. S., Drabek, E., et al. 2010, ApJ, 724, L137

Kubo, J. M. & Dell'Antonio, I. P. 2008, MNRAS, 385, 918

Lawrence, S., Giles, C. L., Tsoi, A. C., & Back, A. D. 1997, IEEE transactions on neural networks, 8, 98

Le Fèvre, O., Saisse, M., Mancini, D., et al. 2003, in Proc. SPIE, Vol. 4841, Instrument Design and Performance for Optical/Infrared Ground-based Telescopes, ed. M. Iye & A. F. M. Moorwood, 1670–1681

Lenzen, F., Schindler, S., & Scherzer, O. 2004, A&A, 416, 391

Lotz, J. M., Koekemoer, A., Coe, D., et al. 2016, arXiv:1605.06567

LSST Sci. Collaboration, Abell, P. A., Allison, J., et al. 2009, arXiv:0912.0201

Luppino, G. A., Gioia, I. M., Hammer, F., Le Fèvre, O., & Annis, J. A. 1999, A&AS, 136, 117

Lynds, R. & Petrosian, V. 1986, in Bulletin of the American Astronomical Society, Vol. 18, Bulletin of the American Astronomical Society, 1014

Magaña, J., Motta, V., Cárdenas, V. H., Verdugo, T., & Jullo, E. 2015, ApJ, 813, 69

Marshall, P. J., Hogg, D. W., Moustakas, L. A., et al. 2009, ApJ, 694, 924

Maturi, M., Mizera, S., & Seidel, G. 2014, A&A, 567, A111

Maughan, B. J., Jones, C., Forman, W., & Van Speybroeck, L. 2008, ApJS, 174, 117

Meneghetti, M., Bartelmann, M., Dahle, H., & Limousin, M. 2013, Space Sci. Rev., 177, 31

Meneghetti, M., Dolag, K., Tormen, G., et al. 2004, Modern Physics Letters A, 19, 1083

Meneghetti, M., Jain, B., Bartelmann, M., & Dolag, K. 2005, MNRAS, 362, 1301

Meneghetti, M., Natarajan, P., Coe, D., et al. 2016, arXiv:1606.04548

Meyer, D. & Wien, F. T. 2015, The Interface to libsvm in package e1071

Mollerach, S. & Roulet, E. 2002, Gravitational Lensing and Microlensing (World Scientific)

Monna, A., Seitz, S., Greisel, N., et al. 2014, MNRAS, 438, 1417

More, A., Cabanac, R., More, S., et al. 2012, ApJ, 749, 38

More, A., Verma, A., Marshall, P. J., et al. 2016, MNRAS, 455, 1191

Natarajan, P., De Lucia, G., & Springel, V. 2007, MNRAS, 376, 180

Navarro, J. F., Frenk, C. S., & White, S. D. M. 1996, ApJ, 462, 563

Navarro, J. F., Frenk, C. S., & White, S. D. M. 1997, ApJ, 490, 493

Neto, A. F., Gao, L., Bett, P., et al. 2007, MNRAS, 381, 1450

Nord, B., Buckley-Geer, E., Lin, H., et al. 2015, arXiv:1512.03062

Oguri, M. 2007, ApJ, 660, 1

Oguri, M. 2010, glafic: Software Package for Analyzing Gravitational Lensing, Astrophysics Source Code Library

Overzier, R., Lemson, G., Angulo, R. E., et al. 2012, Monthly Notices of the Royal Astronomical Society

Palmese, A., Lahav, O., Banerji, M., et al. 2016, MNRAS, 463, 1500

Paraficz, D., Courbin, F., Tramacere, A., et al. 2016, arXiv:1605.04309

Peebles, P. 1993, Principles of Physical Cosmology, Princeton series in physics (Princeton University Press)

Peng, C. Y., Ho, L. C., Impey, C. D., & Rix, H.-W. 2010, AJ, 139, 2097

Petrillo, C. E., Tortora, C., Chatterjee, S., et al. 2017, arXiv: 1702.07675

Petters, A., Levine, H., & Wambsganss, J. 2012, Singularity Theory and Gravitational Lensing, Progress in Mathematical Physics (Birkhäuser Boston)

Pizzuti, L., Sartoris, B., Borgani, S., et al. 2016, arXiv:1602.03385

Planck Collaboration, Ade, P. A. R., Aghanim, N., et al. 2014, A&A, 571, A16

Planck Collaboration, Ade, P. A. R., Aghanim, N., et al. 2016, A&A, 594, A13

Postman, M., Coe, D., Benítez, N., et al. 2012, ApJS, 199, 25

Priewe, J., Williams, L. L. R., Liesenborgs, J., Coe, D., & Rodney, S. A. 2016, arXiv:1605.07621

Ratnatunga, K. U., Griffiths, R. E., & Ostrander, E. J. 1999, AJ, 117, 2010

Rebentrost, P., Mohseni, M., & Lloyd, S. 2014, Physical review letters, 113, 130503

Refregier, A., Amara, A., Kitching, T. D., et al. 2010, arXiv:1001.0061

Ren, S., He, K., Girshick, R., & Sun, J. 2015, in Advances in neural information processing systems, 91–99

Richard, J., Jauzac, M., Limousin, M., et al. 2014, MNRAS, 444, 268

Richard, J., Jones, T., Ellis, R., et al. 2011, MNRAS, 413, 643

Riess, A. G., Filippenko, A. V., Challis, P., et al. 1998, AJ, 116, 1009

Rumelhart, D. E., Hinton, G. E., & Williams, R. J. 1988, Cognitive modeling, 5, 1

Russakovsky, O., Deng, J., Su, H., et al. 2015, International Journal of Computer Vision, 115, 211

Ryden, B. 2016, Introduction to Cosmology (Cambridge University Press)

Rykoff, E. S., Rozo, E., Busha, M. T., et al. 2014, ApJ, 785, 104

Sand, D. J., Treu, T., Ellis, R. S., & Smith, G. P. 2005, ApJ, 627, 32

Schneider, P., Ehlers, J., & Falco, E. 2013, Gravitational Lenses, Astronomy and Astrophysics Library (Springer Berlin Heidelberg)

Schutz, B. 2009, A First Course in General Relativity (Cambridge University Press)

Schwab, J., Bolton, A. S., & Rappaport, S. A. 2010, ApJ, 708, 750

Seidel, G. & Bartelmann, M. 2007, A&A, 472, 341

Sersic, J. L. 1968, Atlas de galaxias australes

Simard, P. Y., Steinkraus, D., Platt, J. C., et al. 2003, in ICDAR, Vol. 3, Citeseer, 958–962

Smith, G. P., Kneib, J.-P., Smail, I., et al. 2005, MNRAS, 359, 417

Smith, G. P., Kneib, J.-P., Smail, I., et al. 2005, Monthly Notices of the Royal Astronomical Society, 359, 417

Soucail, G., Fort, B., Mellier, Y., & Picat, J. P. 1987, A&A, 172, L14

Soucail, G., Kneib, J.-P., & Golse, G. 2004, A&A, 417, L33

Spergel, D., Gehrels, N., Baltay, C., et al. 2015, ArXiv e-prints

Suyu, S. H., Marshall, P. J., Auger, M. W., et al. 2010, ApJ, 711, 201

Suyu, S. H., Treu, T., Hilbert, S., et al. 2013, arXiv:1306.4732

Treu, T. & Koopmans, L. V. E. 2002, The Astrophysical Journal, 575, 87

Treu, T. & Koopmans, L. V. E. 2002, MNRAS, 337, L6

van de Ven, G., Mandelbaum, R., & Keeton, C. R. 2009, MNRAS, 398, 607

Vikram, V., Wadadekar, Y., Kembhavi, A. K., & Vijayagovindan, G. V. 2010, MNRAS, 409, 1379

Weinberg, S. 1972, Gravitation and cosmology: principles and applications of the general theory of relativity, Vol. 67 (Wiley New York)

Wen, Z.-L., Han, J.-L., & Jiang, Y.-Y. 2011, Research in Astronomy and Astrophysics, 11, 1185

Wiener, N. 1964, Extrapolation, interpolation, and smoothing of stationary time series: with engineering applications, Technology press books in science and engineering (Technology Press of the Massachusetts Institute of Technology)

Williams, D. R. G. H. R. & Hinton, G. 1986, Nature, 323, 533

Willis, J. P., Hewett, P. C., Warren, S. J., Dye, S., & Maddox, N. 2006, MNRAS, 369, 1521

Xu, B., Postman, M., Meneghetti, M., et al. 2016, ApJ, 817, 85

Yamamoto, K., Kadoya, Y., Murata, T., & Futamase, T. 2001, Progress of Theoretical Physics, 106, 917

Yoon, I., Weinberg, M. D., & Katz, N. 2011, MNRAS, 414, 1625

York, D. G., Adelman, J., Anderson Jr, J. E., et al. 2000, The Astronomical Journal, 120, 1579

Zackrisson, E. & Riehm, T. 2010, Advances in Astronomy, 2010

Zaritsky, D. & Gonzalez, A. H. 2003, ApJ, 584, 691